8-2022

Design and Operation of a Microwave Flow Cytometer for Single Cell Detection and Identification

Jeffrey A. Osterberg
josterb@clemson.edu

DESIGN AND OPERATION OF A MICROWAVE FLOW CYTOMETER FOR
SINGLE CELL DETECTION AND IDENTIFICATION

A Dissertation
Presented to
the Graduate School of
Clemson University

In Partial Fulfillment
of the Requirements for the Degree
Doctor of Philosophy
Electrical Engineering

by
Jeffrey Andrew Osterberg
August 2022

Accepted by:
Pingshan Wang, Committee Chair
Sarah Harcum
Anthony Martin
William Harrell

ABSTRACT

Microwave dielectric sensing has become a popular technique in biological cell sensing for its potential in online, label-free, and real-time sensing. At microwave frequencies probing signals are sensitive to intracellular properties since they are able to penetrate cell membranes, making microwave flow cytometry a promising technology for label-free biosensing. In this dissertation a microwave flow cytometer is designed and used to measure single biological cells and micro particles. A radio frequency (RF)/microwave interferometer serves as the measurement system for its high sensitivity and tunability and we show that a two-stage interferometer can achieve up to 20 times higher sensitivity than a single interferometer. A microstrip sensor with an etched microfluidic channel is used as the sensing structure for measuring single cells and particles in flow.

The microwave flow cytometer was used to measure changes in complex permittivity, $\varepsilon(f) = \varepsilon'(f) - j\varepsilon''(f)$, of viable and nonviable *Saccharomyces cerevisiae* and *Saccharomyces pastorianus* yeast cells and changes in complex permittivity and impedance of two lifecycle stages of *Trypanosoma brucei*, a unicellular eukaryotic parasite found in sub-Saharan Africa, at multiple frequencies from 265 MHz to 7.65 GHz.

Yeast cell measurements showed that there are frequency dependent permittivity differences between yeast species as well as viability states. Quadratic discriminate analysis (QDA) and k-nearest neighbors (KNN) were employed to validate the ability to

classify yeast species and viability, with minimum cross-validation error of with cross validation errors of 19% and 15% at 2.38 GHz and 265 MHz, respectively.

Measurements of changes in permittivity and impedance of single procyclic form (PCF) and bloodstream form (BSF) *T. brucei* parasites also showed frequency dependence. The two cell forms had a strong dependence on the imaginary part of permittivity at 2.38 GHz and below and a strong dependence on the real part of permittivity at 5.55 GHz and above. Three PCF cell lines were tested to verify that the differences between the two cell forms were independent of cell strain. QDA gave maximum cross-validation errors of 15.4% and 10% when using one and three PCF strains, respectively. Impedance measurements were used to improve cell classification in cases where the permittivity of a cell cannot be detected.

Lastly, a microwave resistance temperature detector (RTD) is designed, and a model is developed to extract the temperature and complex permittivity of liquids in a microfluidic channel. The microwave RTD is capable of measuring temperature to within 0.1°C. The design can easily be modified to increase sensitivity be lengthening the sensing electrode or modified for smaller volumes of solute by shortening the electrode.

DEDICATION

This dissertation is dedicated to my wife Neelima.

ACKNOWLEDGMENTS

TABLE OF CONTENTS

Table of Contents (Continued)

LIST OF TABLES

LIST OF FIGURES

List of Figures (Continued)

List of Figures (Continued)

List of Figures (Continued)

Figure   Page

List of Figures (Continued)

Figure   Page

List of Figures (Continued)

List of Figures (Continued)

Figure   Page

List of Figures (Continued)

CHAPTER ONE

INTRODUCTION

Microwave technology has attracted significant interests in biological cell sensing due to the potential for label-free and real-time sensing. Biological cells generally exhibit a frequency dependent permittivity similar to that shown in Fig. 1.1, which is characterized by three distinct dispersion regions, or frequency regions with a particularly strong frequency dependence separated by plateaus [1.1]. The α-dispersion region typically occurs from several Hz up to a few kHz and is associated with the diffusion process of ions at interfaces, such as membranes, and is hence correlated with membrane potential, the β-dispersion region typically occurs from several kHz up to tens or hundreds of MHz and is associated with the polarization of cellular membranes and other organic macromolecules, and the γ-dispersion region typically occurs above 10 GHz and is primarily attributed to the polarization of water molecules [1.2-1.5].

Broadband dielectric spectroscopy can be used to extract a wealth of information from biological systems. Generally speaking, there are two approaches to dielectric measurements of biological systems – measurement of bulk cell monolayers and suspensions, and single cell measurements. Bulk cell dielectric measurements can quantify cell concentration, provide cell size, membrane capacitance, and cytoplasm permittivity and conductivity [1.6, 1.7]. Due to the large sample size bulk measurements of a stationary suspension can be easily measured over a broad frequency range using a parallel plate capacitor or coaxial probe. RF and microwave sensors have been used to

1
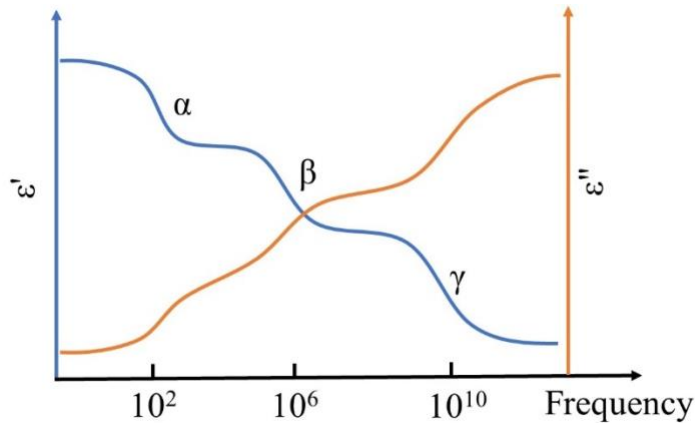
Fig. 1.1. Complex permittivity spectrum of biological tissues showing three distinct dispersion regions – α, β, and γ.

detect cancer cells (liver, breast, lymphocyte, bone) [1.8-1.13], on-line monitoring of cell adhesion [1.14], alterations of cell morphology and motility for cytotoxicity assessment of chemicals [1.15], and on-line biomass monitoring [1.16]. A major drawback of bulk measurements is the lack of insight provided on the large variability of individual cells within the population and most studies of this type are well controlled in the lab and may not translate to real-world applications. Additionally, the complex models required to extract cell properties are only valid for low concentrations of cells as intercellular interactions at higher concentrations are difficult to predict.

The second dielectric measurement approach, single cell measurements or flow cytometry, measures several individual cells within a culture. Single cell dielectric spectroscopy has mainly focused on the β-dispersion regions, which is primarily affected by the cell membrane. Radio wave and microwave fields in the MHz and GHz frequency range can penetrate the cell membrane and detect intracellular properties, and hence

microwave-based flow cytometers have the potential to be highly sensitive partly due to strong interactions between microwaves and cells and the large permittivity contrasts between cells and liquid medium matrix.

A variety of approaches have been developed and different types of cells have been tested. For instance, a combination of a resonator and interference measurements demonstrated high sensitivity microwave (1.1 GHz) detection of dual-frequency dielectrophoresis response of in-flow CHO cells [1.17]. A straight transmission line with a sensing gap has been used to monitor single cell monocytes subject to electroporation [1.18], where a blocker is used to capture single cells for broadband measurement up to 40 GHz. A similar design was developed for detecting small populations of *E. coli* cells from 0.5 to 20 GHz [1.19]. Passive interferometers were built to measure single yeast cells [1.20, 1.24]. Nevertheless, the lack of specificity has been the limiting factor for microwave cell sensing.

Results from various microwave and RF sensing efforts indicated potential measurement specificity. At lower frequencies, impedance measurements [1.21] have shown partial success in single cell identification when the ratio of impedance at two different frequencies (i.e. opacity) is used [1.22, 1.23]. At 5.0 GHz, viable and non-viable yeast cells showed significantly different signals [1.24]. The fact that a cell species can have highly conserved and stable molecular components, such as fatty acids [1.25], likely enabled the differentiation due to differing charges, polarization, and dynamics of molecules of the bacteria. These drawbacks could be overcome by measuring individual cells within a cell suspension over a broadband. Thus, a combination of broadband and

3

high-frequency measurements of single cells presents the best opportunity in the search for cell differentiation power due to potentially added information of molecular relaxation not detected by single frequency or narrow band probing and cell organelles not detectable at low frequencies. As a result, microwave measurement specificity could be achieved without using bio-recognition elements or labels. The specificity would address the major limitation of microwave sensor application in biology as well as chemical and environmental monitoring, where substance identification is of paramount importance. While label-based technologies can provide high specificity, these tools are often labor and cost intensive. Nevertheless, measuring single in-flow cells over a wide frequency range remains a challenge despite significant efforts and progress.

In Chapter II of this dissertation the design of a simple RF interferometer is presented, which serves as the measurement system for the microwave flow cytometer. RF interferometers have been demonstrated for high sensitivity detection and analysis of single cells [1.26, 1.27], particles [1.28], DNAs [1.29], glucose, methanol, and 2-propanel [1.30-1.32] in solution. Their design flexibility, tunable sensitivity and frequency coverage are attractive properties for various sensing applications. Nevertheless, for high sensitivity measurements, the required system dynamic range is exceptionally large, e.g. $\sim$ 120 dB for an effective quality factor of $\sim 3 \times 10^6$ [1.32]. As a result, such systems are difficult to use in rugged environments. To help address this problem, different filters and resonators [1.33-1.35] have been proposed and demonstrated to improve sensitivity for a given dynamic range. With engineered spectrum and dispersion relationship, the probing RF waves in these devices are slowed down with enhanced field intensities,

which lead to longer and stronger interactions between RF fields and material-under-test (*mut*). The group delays, which are defined as $t_g = -d\varphi/d\omega|_{\omega_0}$ with φ the frequency dependent phase shift and ω0 the operating frequency, of these filters and resonators are positive. Corresponding group velocities, v_g, are lower than the speed of light, c, in the medium, i.e. $v_g < c$.

We also show that an RF interferometer can be incorporated into a second one to form a two-stage interferometer setup to achieve up to 20-times higher frequency sensitivity, compared with one-stage interferometers. The improvements are better than that with filters and resonators in [1.33-1.35]. We also show that a single stage interferometer has negative group delays (NGDs), i.e. negative group velocities (NGVs), and SP regimes. Such abnormal electromagnetic properties have been reported in a few structures and circuits [1.36-1.39]. In RF interferometers, these properties occur around the operating frequency points due to destructive interference of two traveling waves at the output port, similar to the processes at the dark port of a Mach–Zehnder interferometer [1.38]. A simple model shows that loss or reflection is not necessary for the RF interferometer to exhibit those properties. At the same time, large positive group delays (PGD) can be easily obtained. The achievable NGD, PGD and SP levels can be easily tuned. Such tunability is not available in other passive circuits. Furthermore, these abnormal properties can be exploited for high sensitivity sensor applications.

In Chapter III the sensor for the microwave flow cytometer is introduced. A microstrip sensor with an integrated microfluidic channel is used for detection of single cells in the cytometer. The microstrip sensor was shown to have better sensitivity than

CPW sensors [1.40], provides more reliable measurements by minimizing the uncertainty from variations in cell sizes and vertical location, and allows for broadband operation.

In Chapter V the microwave flow cytometer is applied to two *Saccharomyces* yeasts of closely related species, showing significant microwave property differences that can be used to differentiate the species and their viability in a cell-particle mixture suspension.

The ability to accurately identify the phase of a cell is critical in cell cycle research. For some cells, such as yeast, the stages of cell growth (budding or non-budding) are easy to observe by optical microscopy. For cells like *Trypanosoma brucei*, where different forms of the cell have similar morphology, more advanced approaches such as immunostaining, which selectively targets proteins in cells, are employed to identify and study cell cycles [1.41, 1.42]. These methods are time consuming, can only be performed periodically, and require the use of labels. Researchers have long put significant efforts into finding noninvasive and label-free methods for real time monitoring of cells. Dielectric sensing shows promise in being able to monitor cell cycle progression noninvasively and in real-time.

Many studies have shown that the dielectric properties of cells can be used to determine the phase of cells in their lifecycle, such as [1.43], where changes in permittivity of a yeast culture below 300 kHz corresponded to an increase in cell length and bud size of budding yeast. The same authors later showed that the peaks in the cyclic changes of the permittivity corresponded with the time when daughter cells segregated from mother cells [1.44], which can be used to monitor and synchronize yeast cell

6

division [1.45]. In [1.46], the authors showed that the capacitance of Chinese hamster ovary (CHO) cell cultures can be used as an indicator of transition points of the culture. Typically, these studies looked at the behavior of entire populations in synchronized cultures and thus fail to account for the large variability of individual cells within a culture. Additionally, these studies focused on the α- and β-dispersion regions, which is primarily affected by the cell membrane. Radio wave and microwave fields in the MHz and GHz frequency range can penetrate the cell membrane. The ability of microwave probing signals to penetrate cell walls indicates that microwave sensing could detect intercellular differences between cells that are unobtainable at lower frequencies [1.47]. Trapping-based sensors have also been developed for monitoring lifecycles of single cells, including a sensor that was developed to monitor the capacitive contrast of trapped living B lymphoma cells from 40 MHz to 40 GHz [1.48]. A similar approach was used to monitor the lifecycles of single budding yeast cells by correlating impedance at lower frequencies (10 kHz to 10 MHz) with optically monitored cell morphologies [1.49]. However, trapping based sensors can only score a single cell throughout the entire cell cycle, and thus lack the ability to analyze the significant number of cells in a culture that is required for phenotype analysis. Microwave flow cytometer sensors offer the ideal combination of high sensitivity and high throughput that enables label free detection of lifecycles of single cells in real time. In Chapter VI the microwave flow cytometer is used to measure the permittivity and impedance of single *Trypanosoma brucei* cells and show that the system can discriminate between two lifecycle stages of *T. brucei* cells-bloodstream form (BSF) and procyclic form (PCF).

In Chapter VII a highly sensitive microwave resistance temperature detector (RTD) sensor is proposed and demonstrated. The frequency and temperature dependent nature of polar liquids has been investigated thoroughly over the past several decades but precise temperature measurements in microfluidic chips is still a difficult task due to fast thermal transfer rates in small sample volumes, making it difficult to observe and account for local hot spots. The microwave RTD sensor is capable of measuring temperature in a microfluidic channel to within 0.1°C.

References

[1.1]   H.P. Schwan, "Electrical properties of tissue and cell suspensions," *Advances in Biological and Medical Physics*, vol. 5, pp. 147-209, 1957.

[1.2]   C. Prodan, F. Mayo, J. R. Claycomb, J. H. Miller Jr., and M.J. Benedik, "Low-frequency, low-field dielectric spectroscopy of living cell suspensions," *Journal of Applied Physics*, vol. 95, iss. 7, Apr. 2004.

[1.3]   K.R. Foster and H.P. Schwan, "Dielectric properties of tissues and biological materials: a critical review," *Critical Reviews in Biomedical Engineering*, vol. 17, iss. 1, pp. 25-104, Feb. 1989.

[1.4]   T.P. Bothwell and H.P. Schwann, "Electrical properties of the plasma membrane of erythrocytes at low frequencies," *Nature*, vol. 178, iss. 4527, pp. 265-266, Aug. 1956.

[1.5]   H.P. Schwan and E.L. Casrtensen, "Di-electric properties of the membrane of lysed erythrocytes," *Science*, vol. 125, iss. 3255, pp. 986-986, May 1957.

[1.6]   K. Asami, "Characterization of heterogeneous systems by dielectric spectroscopy." *Progress in Polymer Science*, vol. 27, iss. 8, pp. 1617-1659, Oct. 2002.

[1.7]   K. Asami, T.Yonezawa, H.Wakamatsu, and N. Koyanagic, "Dielectric spectroscopy of biological cells," *Bioelectrochemistry and Bioenergetics*, vol. 40, iss. 2, pp. 141-145, Aug. 1996.

[1.8]   Y.F Chen, H.W. Wu, Y.H. Hong, and H.Y. Lee, "40 GHz RF biosensor based on microwave coplanar waveguide transmission line for cancer cells (HepG2) dielectric characterization," *Biosensors and Bioelectronics*, vol. 61, pp 417-421, Nov. 2014.

[1.9]   M. Hussein, F. Awwad, D. Jithin, H. El Hasasna, K. Athamneh, and R. Iratni, "Breast cancer cells exhibits specifc dielectric signature in vitro using the open-ended coaxial probe technique from 200 MHz to 13.6 GHz," *Scientific Reports*, vol. 9, Mar. 2019.

[1.10]   K. Grenier, F. Artis, M. Poupot, J. Foumié and D. Dubuc, "Label-free discrimination of human lymphoma cell sub-populations with microwave dielectric spectroscopy," *2018 IEEE/MTT-S International Microwave Symposium - IMS*, Philadelphia, PA, USA, Jun. 2018, pp. 907-910.

[1.11]   G. Qiao , W. Wang, W. Duan, F. Zheng, A.J. Sinclair, and C.R. Chatwin, "Bioimpedance analysis for the characterization of breast cancer cells in suspension." *IEEE Transactions on Biomedical Engineering*, vol. 59, no. 8, pp. 2321-2329, Aug. 2012.

[1.12]   Z. Macit, C. Aydinalp, T. Yilmaz, A.B.O. Sert and F.N. Kok, "Microwave Dielectric properties of Osteosarcoma Cell Line (SAOS-2) Suspensions," *2019 23rd International Conference on Applied Electromagnetics and Communications (ICECOM)*, Dubrovnik, Croatia, Sep./Oct. 2019, pp. 1-4.

[1.13]   A. Han, L. Yang, and A. B. Frazier, "Quantification of the Heterogeneity in Breast Cancer Cell Lines Using Whole-Cell Impedance Spectroscopy," *Clinical Cancer Research*, vol. 13, no. 1, pp. 139-143, Jan. 2007.

[1.14]   L. Ceriotti, J. Ponti, P. Colpo, E. Sabbioni, and F. Rossi, "Assessment of cytotoxicity by impedance spectroscopy," *Biosensors and Bioelectronics*, vol. 22, no. 12, pp. 3057-3063, Jun. 2007.

[1.15]   D. Opp, B. Wafula, J. Lim, E. Huang, J. Lo, and C. Lo, "Use of electric cell–substrate impedance sensing to assess in vitro cytotoxicity" *Biosensors and Bioelectronics*, vol. 24, no. 8, pp. 2625-2629, Apr. 2009.

[1.16]   J. P. Carvell, and J. E. Dowd, "On-line measurements and control of viable cell density in cell culture manufacturing processes using radio-frequency impedance," *Cytotechnology*, vol. 50, no. 1, pp. 35-48, Mar. 2006.

[1.17]   S. Afshar, E. Salimi, K. Braasch, M. Butler, D. J. Thomson, and G. E. Bridges, "Multi-frequency DEP cytometer employing a microwave sensor for dielectric analysis of single cells," *IEEE Transactions on Microwave Theory and Techniques,* vol. 64, no.3, pp. 991-998, Mar. 2016.

[1.18] A. Tamra, D. Dubuc, M. Rols, and K. Grenier, "Microwave monitoring of single cell monocytes subjected to electroporation," *IEEE Transactions on Microwave Theory and Techniques,* vol. 65, no. 9, pp. 3512-3518, Sep. 2017.

[1.19] H. Li *et al.*, "Differentiation of live and heat-killed *E. coli* by microwave impedance spectroscopy," *Sensors and Actuators B: Chemical,* vol. 255, no. 2, pp. 1614-1622, Feb. 2018.

[1.20] Z. Wang et al., "Time domain detection and differentiation of single particles and cells with a radio frequency interferometer," *2016 IEEE Topical Conference on Biomedical Wireless Technologies, Networks, and Sensing Systems (BioWireleSS)*, Austin, TX, USA, Jan. 2016, pp. 77-80.

[1.21] S. Gawad, L. Schild, and P. H. Renaud, "Micromachined impedance spectroscopy flow cytometer for cell analysis and particle sizing," *Lab on a Chip,* vol. 1, no. 1, pp. 76-82, Sep. 2001.

[1.22] D. Holmes, *et al.*, "Leukocyte analysis and differentiation using high speed microfluidic single cell impedance cytometry," *Lab on a Chip,* vol. 9, no. 20, pp. 2881-2889, Oct. 2009.

[1.23] J. McGrath, C. Honrado, D. Spencer, B. Horton, H. Bridle, and H. Morgan, "Analysis of parasitic protozoa at the single-cell level using microfluidic impedance cytometry," *Scientific Reports,* vol. 7, iss. 1, Jun. 2017.

[1.24] Y. Yang, H. Zhang, J. Zhu, G. Wang, T.R. Tzeng, X. Xuan, K. Huang, and P. Wang, "Distinguishing the viability of a single yeast cell with an ultra-sensitive radio frequency sensor," *Lab on a Chip,* vol. 10, iss. 5, pp. 553-555, Jan. 2010.

[1.25] B. Slabbinck, B. De Baets, P. Dawyndt, and P. De Vos, "Towards large-scale FAME-based bacterial species identification using machine learning techniques," *Systematic and Applied Microbiology,* vol. 32, no. 3, pp. 163-176, May 2009.

[1.26] G.A. Ferrier, S.F. Romanuik, D.J. Thomson, G.E. Bridges, and M.R. Freeman, "A microwave interferometric system for simultaneous actuation and detection of single biological cells," *Lab on a Chip*, vol. 9, iss. 23, pp. 3406-3412, Oct. 2009.

[1.27] G. A. Ferrier, S. F. Romanuik, D. J. Thomson, G. E. Bridges, and M. R. Freeman, "A microwave interferometric system for simultaneous actuation and detection of single biological cells," *Lab on a Chip,* vol. 9, iss. 23, pp. 3406-3412, Dec. 2009.

[1.28] X. Hu, G. Yu, J. W. Sun, D. Moline, and P. Wang, "Radio frequency detection and analysis of synthetic particles," *2014 IEEE Topical Conference on Biomedical Wireless Technologies, Networks, and Sensing Systems (BioWireleSS)*, Newport Beach, California, Jan. 2014, pp. 49-51.

[1.29] Y. Cui, J. Li, W. Cao, and P. Wang, "Highly Sensitive RF Detection and Analysis of DNA Solutions," *2014 IEEE MTT-S International Microwave Symposium (IMS2014),* Tampa, Florida, Jun. 2014, pp. 1-4.

[1.30] Y. Cui and P. Wang, "The design and operation of ultra-sensitive and tunable radio-frequency interferometers," *IEEE Transactions on Microwave Theory and Techniques,* vol. 62, iss. 12, pp. 3172-3182, Dec. 2014.

[1.31] C. Song and P. Wang, "A radio frequency device for measurement of minute dielectric property changes in microfluidic channels," *Applied Physics Letters,* vol. 94, iss. 2, Jan. 2009.

[1.32] Y. Cui, J. Sun, Y. He, Z. Wang, and P. Wang, "A simple, tunable, and highly sensitive radio-frequency sensor," *Applied physics letters,* vol. 103, iss. 6, Aug. 2013.

[1.33] C. Shen, Z. Chen, Y. Shao, and P. Wang, "Engineering Spectrum and Dispersion with Filters for High-Sensitivity RF Detections," *Applied Physics Letters,* vol. 105, Jul. 2014.

[1.34] Z. Chen and P. Wang, "Resonator and Filter Induced Slow Waves for High-Sensitivity RF Interferometer Operations," *IEEE Sensors Journal,* vol. 15, iss. 5, May 2014.

[1.35] Y. Shao, Z. Chen, and P. Wang, "Exploiting Filter Stop Band for Radio Frequency Interferometer Operation," *IEEE Sensors Journal,* vol. 15, iss. 10, Oct. 2014.

[1.36] D. Solli, C. McCormick, C. Ropers, J. Morehead, R. Chiao, and J. Hickmann, "Demonstration of superluminal effects in an absorptionless, nonreflective system," *Physical Review Letters,* vol. 91, iss. 14, Aug. 2003.

[1.37] H. Mirzaei, R. Islam, and G. V. Eleftheriades, "Anomalous negative group velocity in coupled positive-index/negative-index guides supporting complex modes," *IEEE Transactions on Antennas and Propagation ,* vol. 59, iss. 9, pp. 3412-3420, Sept. 2011.

[1.38] M. Kitano, T. Nakanishi, and K. Sugiyama, "Negative group delay and superluminal propagation: An electronic circuit approach," *IEEE Journal of Selected Topics in Quantum Electronics,* vol. 9, iss. 1, pp. 43-51, Jan-Feb 2003.

[1.39] H. Uranus and H. Hoekstra, "Modeling of loss-induced superluminal and negative group velocity in two-port ring-resonator circuits," *Journal of Lightwave Technology,* vol. 25, iss. 9, pp. 2376-2384, Sep. 2007.

[1.40] C. Song, J. E. Harriss, and P. Wang, "Compensating on-chip transmission line losses for a high-sensitivity microwave sensor," *Sensors and Actuators A: Physical,* vol. 154, no. 1, pp. 7-11, Aug. 2009.

[1.41] K.R. Matthews, T. Sherwin, and K. Gull, "Mitochondrial genome repositioning during the differentiation of the African trypanosome between life cycle forms is microtubule mediated," *Journal of Cell Science*, vol. 108, iss. 6, pp. 2231–2239, Jun. 1995.

[1.42] I. Roditi, H. Schwarz, T.W. Pearson, R.P. Beecroft, M.K. Liu, J.P. Richardson, H.J. Biihring, J. Pleiss, R. Billow, R.O. Williams, and P. Overath, "Procyclin gene expression and loss of the variant surface glycoprotein during differentiation of *Trypanosoma brucei*," *Journal of Cell Biology*, vol. 108, iss. 2, pp. 737–746, Feb. 1989.

[1.43] K. Asami, E. Gheorghiu, and T. Yonezawa, "Real-Time Monitoring of Yeast Cell Division by Dielectric Spectroscopy," *Biophysics Journal*, vol. 76, iss. 6, pp. 3345-3348, Jun. 1999.

[1.44] K. Asami, K. Takahashi, and K. Shirahige, "Progression of cell cycle monitored by dielectric spectroscopy and flow-cytometric analysis of DNA content," *Yeast*, vol. 16, iss. 5, pp. 1359-1363, Nov. 2000.

[1.45] A. Valero, T. Braschler, A. Rauch, N. Demierre, Y. Barral, and P. Renaud, "Tracking and synchronization of the yeast cell cycle using dielectrophoretic opacity," *Lab on a Chip*, vol. 11, 1754-1760, Mar. 2011.

[1.46] C. Cannizzaro, R. Gügerli, I. Marison, and U. von Stockar, "Online biomass monitoring of CHO perfusion culture with scanning dielectric spectroscopy," *Biotechnology and Bioengineering,* vol. 84, iss. 5, pp. 597-610, Dec. 2003.

[1.47] H. P. Schwan, "Electrical properties of tissues and cell suspensions: mechanisms and models," Proceedings of 16th Annual International Conference of the IEEE Engineering in Medicine and Biology Society, Baltimore, MD, USA, Nov. 1994, vol.1, pp. A70-A71.

[1.48] T. Chen, F. Artis, D. Dubuc, J. Fournié, M. Poupot, and K. Grenier, "Microwave biosensor dedicated to the dielectric spectroscopy of a single alive biological cell in its culture medium," *2013 IEEE MTT-S International Microwave Symposium Digest (MTT),* Seattle, WA, USA, Jun. 2013, pp. 1-4.

[1.49] Z. Zhu, O. Frey, N. Haandbæk, D. S. Ottoz, F. Rudolf, and A. Hierlemann, "Real-time multi-parameter monitoring of immobilized single yeast cells via electrical impedance spectroscopy," *2013 Transducers & Eurosensors XXVII: The 17th International Conference on Solid-State Sensors, Actuators and Microsystems*

(TRANSDUCERS & EUROSENSORS XXVII), Barcelona, Spain, Jun. 2013, pp. 1527-1530.

CHAPTER TWO

RADIO FREQUENCY INTERFEROMETER

2.1 Single Stage Radio-Frequency Interferometer

RF interferometers (Fig. 2.1) have been shown to improve the sensitivity of measurements in dielectric spectroscopy measurements [2.1-2.3]. The system operates by splitting an RF signal between two transmission lines of different lengths. When the two signals are combined the resulting frequency response consists of a series of peaks and valleys due to constructive and deconstructive interference. A dielectric sensor is placed in one the signal paths, generally the shorter path to maximize the signal to noise ratio (SNR). A change in the dielectric properties of the sensor results in a change in the complex propagation constant, $\gamma = \alpha + j\beta$, which is observed as a change in the magnitude and phase of the scattering parameters (S-parameters) measured by the vector network analyzer (VNA) when used as a single frequency transmit/receive module. If measuring in the frequency domain a shift in the frequency and magnitude of the minimum point of $|S_{21}|$ is also observed as the change in phase constant β is changes the electrical length of the sensor, and a change in the attenuation constant α changes the balance between the two paths.

To determine the propagation constant from measured S_{21} values, first consider the signal from port 1, $V_1 = V_1^+ + V_1^-$, then assuming a matched system, i.e. $V_1^- = 0$, the outputs of the first power divider are

(a)   (b)
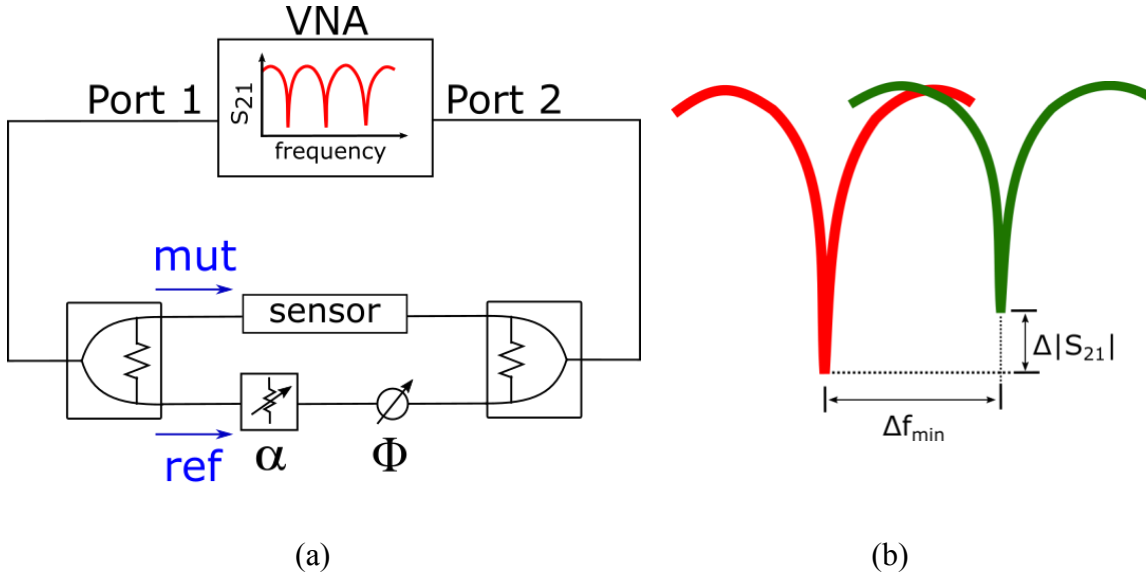
Fig. 2.1. (a) Schematic of a single stage RF interferometer using two Wilkinson power dividers. Attenuator α is used for line balancing and phase shifter Φ is used for tuning operating frequency. (b) Frequency domain signals showing the effect of a change in dielectric properties in the sensor in (a), where a change in α causes a shift in the amplitude $\Delta|S_{21}|$ and a change in β causes a shift in the frequency of the minimum point Δf_{min}.

$$V_{ref} = V_{mut} = -j\frac{V_1^+}{\sqrt{2}} \qquad (2.1)$$

Then the signals at the input of the second power divider are

$$V_{ref,mut} = -j\frac{V_1^+}{\sqrt{2}}e^{-\gamma_{ref,mut}l_{ref,mut}} \qquad (2.2)$$

and the output of the interferometer is

$$V_{out} = -V_1^+\left(e^{-\gamma_{ref}l_{ref}} + e^{-\gamma_{mut}l_{mut}}\right) \qquad (2.3)$$

where γ_{mut} and γ_{ref} are the propagation constants of the two paths of the interferometer. The propagation constants can also be written in terms of frequency as

$$V_{out} = -V_1^+ \left(e^{-\alpha_{ref}l_{ref} - j\frac{2\pi f l_{ref}}{v_{ref}}} + e^{-\alpha_{mut}l_{mut} - j\frac{2\pi f l_{mut}}{v_{mut}}} \right) \tag{2.4}$$

since $\beta = 2\pi f / v_p$, where v_p is the phase velocity of the traveling wave. (2.4) shows that the output will have minimum at frequencies when the phase of the two paths are $180°$ out of phase, i.e.

$$f = \frac{(n-1)v_{ref}v_{mut}}{l_{ref}v_{mut} + l_{mut}v_{ref}}, \qquad n = 1,2,3,... \tag{2.5}$$

The constant n denotes the harmonic number of the interferometer, where $n = 1$ is the fundamental frequency, $n = 2$ is the first harmonic, $n = 3$ is the second harmonic, etc. At harmonic frequencies the level of cancellation at the output is determined by the loss in the two lines, $\alpha_{ref,mut}$, so if $\alpha_{ref} = \alpha_{mut}$ the output would be 0. For a dielectric sensor in the *mut* path, if the permittivity of the sensor changes it causes a shift in the operating frequency, Δf, and the cancellation level $\Delta|S_{21}|$, as shown in Fig. 2.1(b). If Δf is assumed to be caused solely by a phase shift from a change in permittivity of the *mut*, then from (2.5)

$$\Delta\varepsilon_{eff} = \left[\frac{c}{l_{mut}} \left(\frac{n-1}{f + \Delta f} - \frac{l_{ref}}{v_{ref}} \right) \right]^2 - \varepsilon_{eff}, \qquad n = 1,2,3,... \tag{2.6}$$

where the speed of light in free space is $c = 1/\sqrt{\varepsilon_0\mu_0} \approx 3 \cdot 10^8 m/s$ and the phase velocity is related to effective permittivity by $v_p = c/\sqrt{\varepsilon_{eff}}$. Likewise, if $\Delta|S_{21}|$ is

assumed to be solely from a change in dielectric loss of the *mut* the loss tangent, *tan δ_{mut}*,

can be determined from

$$\Delta|S_{21}| = B_{ref} + B_{mut}e^{-\frac{\beta_{mut}(tan\delta_{mut}+\Delta tan\delta_{mut})l_{mut}}{2}-j\beta_{mut}l_{mut}}, \qquad (2.7)$$

Where the coefficients *B_{mut}* and *B_{ref}* are constants. While the above equations can be used

to calculate the complex permittivity from S-parameter measurements, this approach

requires measuring the constant coefficients in equations (2.6) and (2.7). A simpler and

more accurate approach is to use calibration standards. The process for calculating

impedance and permittivity with the use of calibrations in discussed in Chapters III and

IV.

2.2 Two-Stage Interferometer

Fig. 2.2(a) shows the schematic of a two-stage interferometer, in which the first

(i.e. inner) stage uses two commercial power dividers. No tuning components, such as R

and Φ in the second (outer) stage, are used for the first stage to simplify the design and

operation of the two-stage interferometer. Simple microstrip lines on Rogers RO4003C

substrate are built and used as high frequency electrodes for *mut* detection. A second

one-stage interferometer at ~ 2 GHz, Fig. 2.2(b), is also designed and built as the first

stage in Fig. 2.2(a). The use of quadrature hybrids may enable some measurements not

available from power divider settings [2.8].

Figs. 2.3(a) and (b) show the measured $|S_{21}|$ and group delay, respectively, of the

first stage in Fig. 1(a). The constant positive group delay, ~ 4ns, is associated with the

physical delay of the circuit. Around ~ 1.1 GHz and 3.2 GHz, which are the fundamental

and 1st harmonic operating frequency, respectively, negative group delay (NGD), slow

waves and superluminal propagations (SP) exist. For slow waves, we have $0<|v_g|<c$,

(a)   (b)
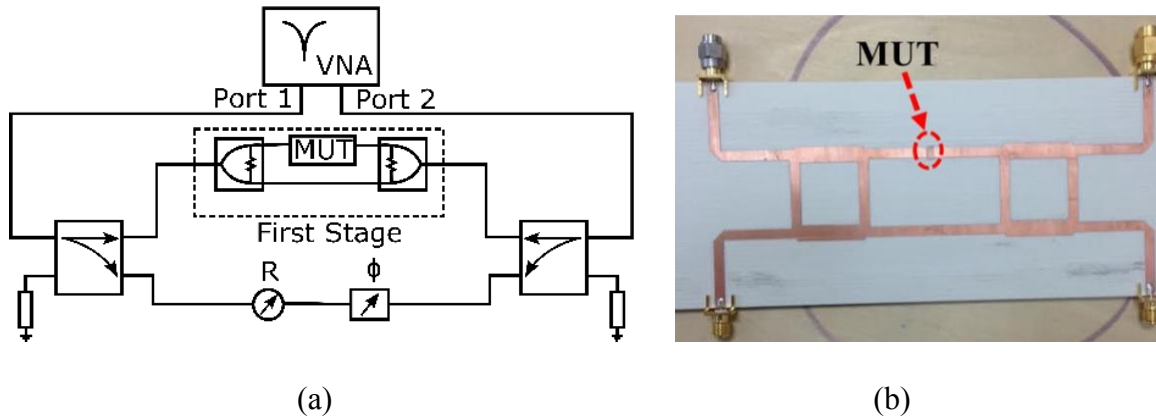
Fig. 2.2 The schematic of a two-stage RF interferometer. Attenuator R and phase shifter

Φ are used for sensitivity and operating frequency tuning. Two commercial power

dividers are used for the first stage and two quadrature hybrids are used for the second

stage. A polydimethylsiloxane (PDMS) slab is used as *mut* and is placed on one path of

the first stage. The paths are formed with uniform microstrip lines. (b) A first stage built

with quadrature hybrids.

while for SP, $|v_g|>c$, where c is the speed of RF waves along the uniform microstrip line.

The NGD indicates negative group velocities, $v_g<0$ [2.7]. Simulation results with

Advanced Design System (ADS) agree with the measured results in Fig. 2.3(b) when

$|S_{21}|_{min}$ is tuned to fit the measured $|S21|_{min}$ in Fig. 2.3(a). Nevertheless, simulations also

show PGD operations in Fig. 2.3(b). A simple analysis can help understand the key

factors that determine the observed main features. Consider an input RF signal (with unit

18

amplitude) that is split by the first broadband power divider into two. At the inputs of the

second power divider we have

$$S_{MUT} = A_1 e^{-j\beta_1 l_1} S_{REF} = A_2 e^{-j\beta_2 l_2} \tag{2.8}$$

where $A_{1,2}$ are the magnitudes of the transmission coefficients, $\beta_{1,2}$ are the propagation

constants and $l_{1,2}$ the electrical lengths of the transmission lines. The output S_{21} of the

second power divider will be

$$S_{21} = A_{21} e^{-j\Phi_{21}} = \frac{A_1}{\sqrt{2}} e^{-j(\beta_1 l_1 + \pi/2)} + \frac{A_2}{\sqrt{2}} e^{-j(\beta_2 l_2 + \pi/2)}, \tag{2.9}$$

Assume A_1 and A_2 are frequency independent around the operating frequency,

taking the negative frequency derivative of (2.9), $-d/d\omega$, gives

$$jA_{21} e^{-j\Phi_{21}} \tau_g - \frac{dA_3}{d\omega} e^{-j\Phi_{21}} =$$

$$\frac{1}{\sqrt{2}} \left[jA_1 e^{-j\Phi_1} \tau_1 - \frac{dA_1}{d\omega} e^{-j\Phi_1} + jA_2 e^{-j\Phi_2} \tau_2 - \frac{dA_2}{d\omega} e^{-j\Phi_2} \right] \tag{2.10}$$

where $\Phi_{1,2} = \beta_{1,2} l_{1,2} - \pi/2$, τ_g is the total group delay and $\tau_{1,2}$ are the group delays of the

individual transmission lines. Equating the imaginary parts of (2.10) gives the total group

delay as

$$\tau_g = \frac{A_1 e^{-j\Phi_1} \tau_1 + A_2 e^{-j\Phi_2} \tau_2}{A_1 e^{-j\Phi_1} + A_2 e^{-j\Phi_2}} \tag{2.11}$$

while $|S_{21}|_{min}$ occurs at frequencies where the two branches have a phase difference of

$$\beta_1 l_1 - \beta_2 l_2 = (2n - 1)\pi \tag{2.12}$$

where n = 1 is the fundamental operating frequency of the interferometer. Under the

condition of (12) the total group delay from (2.11) becomes

$$\tau_g = \frac{A_1\tau_1 - A_2\tau_2}{A_1 - A_2} \tag{2.13}$$

The above equation implies that if A_1 and A_2 are the same that the group delay goes to infinity. However, if they differ the group delay can be either positive or negative, depending on which signal is larger, as shown in Fig. 2.3(b). Current NGD electrical structures and circuits, such as the electromagnetic structures of a backward wave oscillator (BWO) [2.9], the distributed transmission line filter [2.10], left-handed media [2.52, 2.11], and the active circuits [2.6, 2.12], involve complicated wave reflection and propagation processes. The RF interferometer, however, only involves the summation of two traveling waves with minimal reflections occurring in the summation device.

Fig. 2.3(c) shows that at the design frequency, ~ 2 GHz, both $|S_{11}|$ and $|S_{21}|$ are small, as expected for the structure in Fig. 2.2(b). Fig. 2.2(d) shows the measured group delay, where the ~ 1 ns constant group delay is shorter than that in Fig. 2.3(b) due to shorter physical structure length. The -15 ns group delay indicates slower waves than those in Fig. 2.3(b). The slower waves are associated with lower $|S_{21}|$ values in Fig. 2.3(c), as indicated in eq. (6). Both $|S_{11}|$ and $|S_{21}|$ indicate strong reflections within the structure due to discontinuities. Such reflections may be an issue for many signal processing applications. However, for the investigation in this work, the reflections induce new group delay patterns in Fig. 2.3(d) and allow convenient study of group delay effects on interferometer sensitivities.

(a)

(b)

(c)

(d)
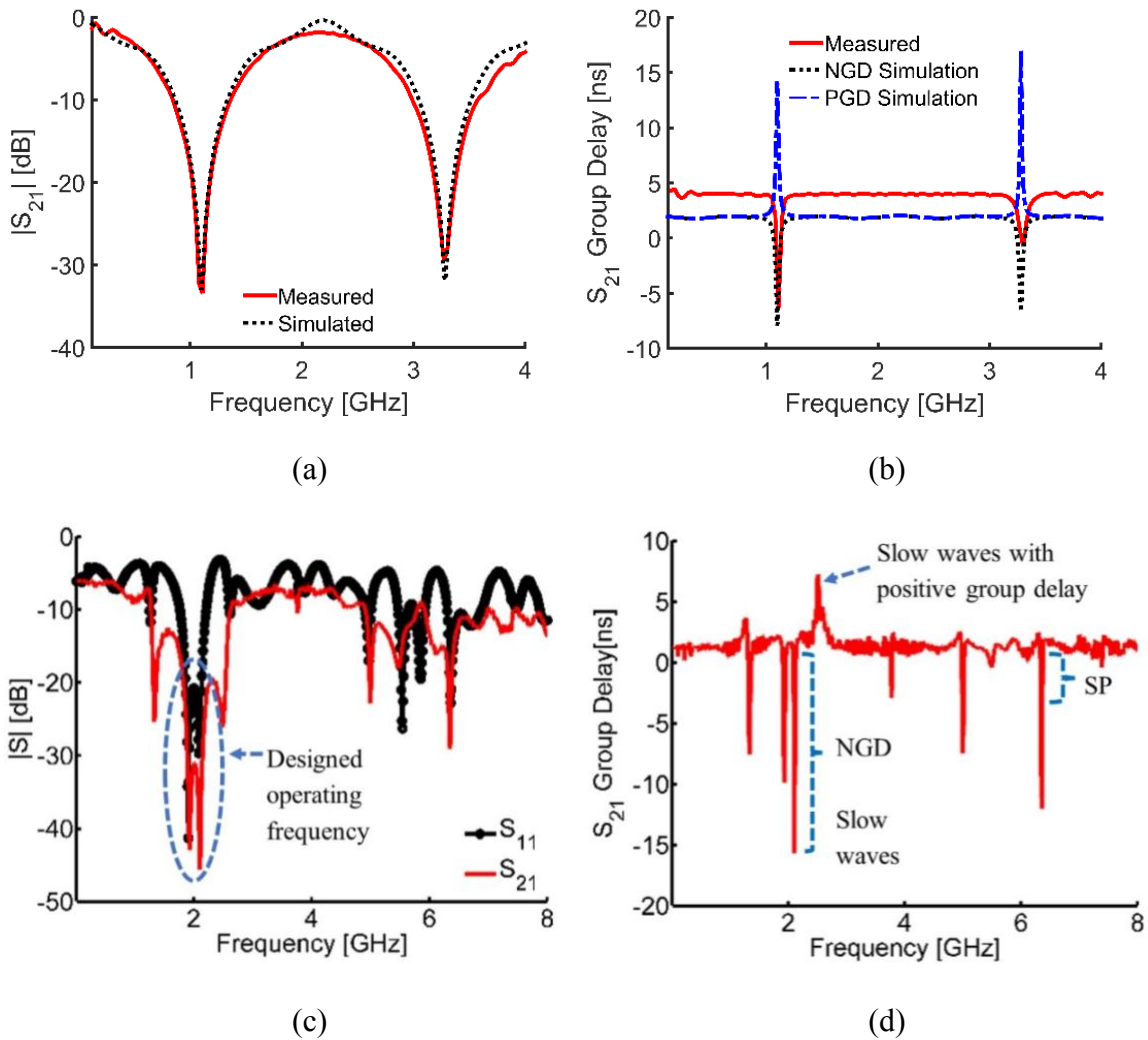
Fig. 2.3 Experimental results of (a) $|S_{21}|$ and (b) group delay of the first stage in Fig. 2.2(a). Simulation results agree with measured ones while simulation also indicates that PSD regimes can exist. Furthermore, the group delay values mainly depend on the balance of the two signal paths, i.e. $|S21|min$. Measured (c) $|S_{11}|$, $|S_{21}|$, and (d) group delay of the first stage in Fig. 2.2(b).

To investigate two stage interferometer operation, we first tune R and Φ in Fig. 2.2(a) to the desired frequency, f_0, and $|S_{21}|_{min}$ ($\sim$ -62-63 dB), as shown in Fig. 2.4(a). Then a *mut* is added to observe frequency shift, Δf, and $|S_{21}|_{min}$ change. Both parameters can be used as sensitivity indicators. A one-stage reference interferometer is also tested for sensitivity comparisons, as shown in Fig. 2.4(b).

The *mut* used is a PDMS slab with dimensions of 4 mm × 2.5 mm × 2 mm. For the two-stage in Fig. 2.2(a), the *mut* is placed on a microstrip line (*mut*-microstrip). For one-stage reference interferometer, the same *mut*-microstrip is used to replace the first stage of Fig. 2.2(a). Additional cables are added to the *mut*-microstrip section, so the electrical length is similar to that of the first stage. For the quadrature stage in Fig. 2.2(b), two measurements are conducted with the *mut* positioned at the center of the two microstrip lines.

Figs 2.4(a) and (b) show that the two-stage interferometer has much larger Δf, i.e. frequency sensitivity. Nevertheless, the curves in Fig. 2.4(a) are less sharp than those in Fig. 2.4(b), indicating a lower effective quality factor, Q_{eff}, and lower frequency reading resolution. The frequency dependent signal amplitude from the first stage, i.e. dispersion in Figs. 2.3(a) and (b), is likely the main factor that affects the Q_{eff}. Nevertheless, Δf is not determined by Q_{eff}, instead it is determined by the effective electrical length difference of the two branches as discussed in [2.4]. Fig. 2.4(c) shows the measured sensitivity improvement factor, which is defined as $\Delta f_{two\text{-}stage}/\Delta f_{one\text{-}stage}$ at the same operating frequency ω_0 and $|S_{21}|_{min}$. Also plotted is the measured group delay. It shows
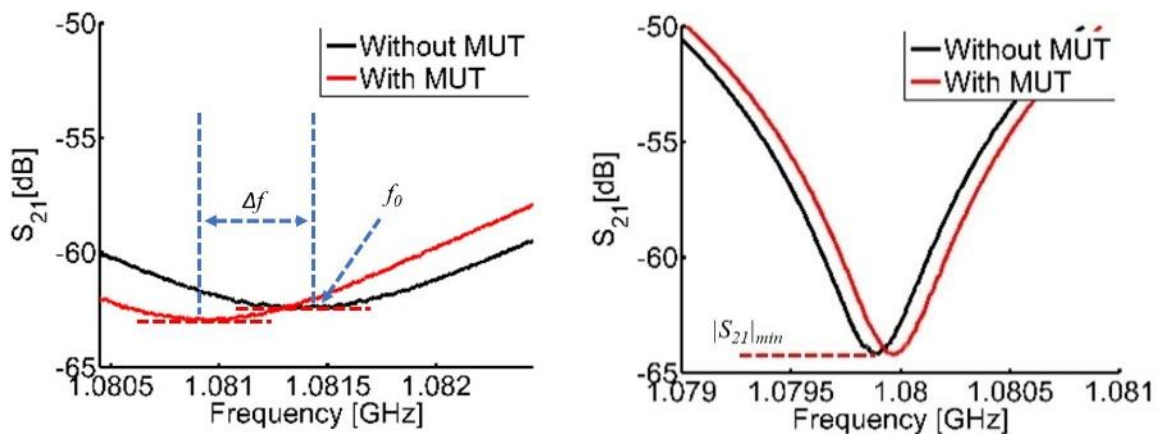
(a)   (b)
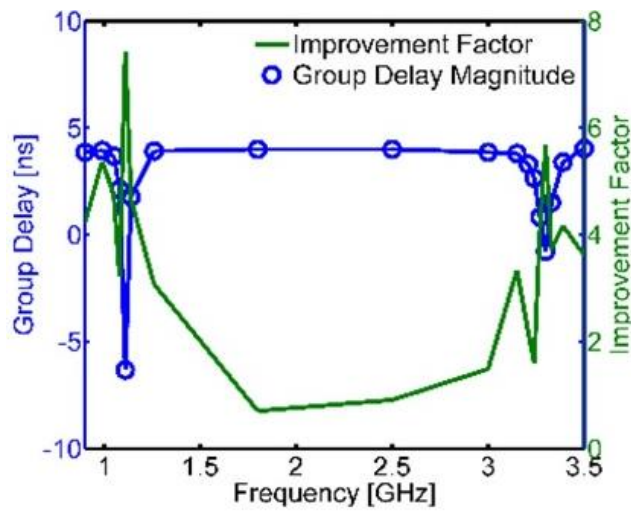
(c)

2.4 (a) Typical measurement results of the two-stage

Fig. 2.4 (a) Typical measurement results of the two-stage interferometer in Fig. 2.2(a).

(b) Typical measurement results of the reference interferometer for Fig. 2.2(a). (c)

Measured sensitivity improvement factor vs. frequency.

that sensor sensitivity is improved when operating at or near the fundamental and 1st harmonic frequencies of the first stage interferometer, regions that also have large NGDs. Secondly, between the two NGD regions, $\Delta f_{two\text{-}stage}/\Delta f_{one\text{-}stage}$ is smaller than 1, which is expected. Within this region, the two-stage interferometers become one-stage interferometers, but with slightly lower sensitivities since the first-stages are effectively straight transmission lines with 3 dB lower RF power for *mut* detections. Although this indicates a correlation between group delay and sensor sensitivity, the mechanisms responsible for the sensitivity enhancement are not fully understood. Fig. 2.4(c) also indicates that the two-stage and one-stage interferometers are operating at the same harmonic (fundamental) frequencies so the comparisons in Fig. 2.4 are fair [2.4].

Fig. 2.5(a) shows typical measurement results with the quadrature hybrid stage in Fig. 2.2(b). *mut* is placed on each of the paths. So the curves shifted left and right. The obtained $\Delta f_{two\text{-}stage}$ is ~3200 kHz compared to ~ 150 kHz in the one-stage reference interferometer, which is an improvement of over 20 times. Fig. 2.5(b) summarizes the measured $\Delta f_{two\text{-}stage}$ from 1 GHz to 3.5 GHz. It shows that $\Delta f_{two\text{-}stage}$ follows the group delay pattern. However, the slow wave with positive group delay, Fig. 2.3(d), yields the highest sensitivity.
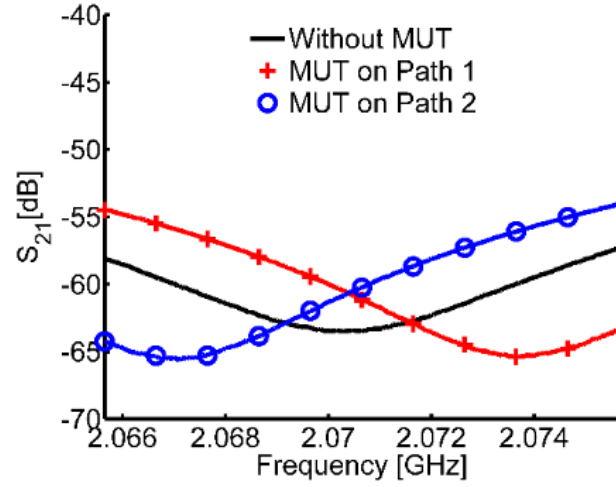
(a)
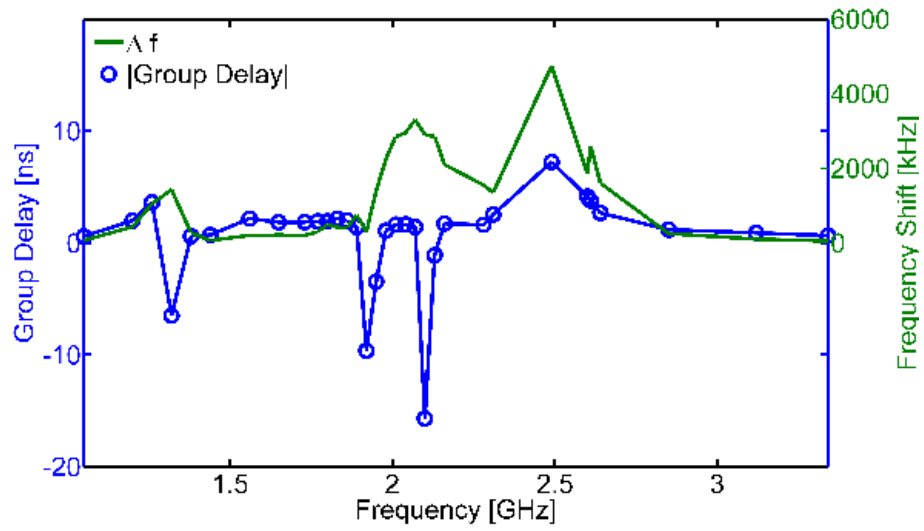
(b)

Fig. 2.5 (a) Typical measured results of the two-stage interferometer with the first stage in Fig. 2.2(b). (b) Measured $\Delta f_{two\text{-}stage}$ vs. frequency.

References

[2.1] Y. Cui and P. Wang, "The design and operation of ultra-sensitive and tunable radio-frequency interferometers," *IEEE Transactions on Microwave Theory and Techniques,* vol. 62, iss. 12, pp. 3172-3182, Dec. 2014.

[2.2] C. Song and P. Wang, "A radio frequency device for measurement of minute dielectric property changes in microfluidic channels," *Applied Physics Letters,* vol. 94, iss. 2, Jan. 2009.

[2.3] Y. Cui, J. Sun, Y. He, Z. Wang, and P. Wang, "A simple, tunable, and highly sensitive radio-frequency sensor," *Applied physics letters,* vol. 103, iss. 6, Aug. 2013.

[2.4] Y. Shao, Z. Chen, and P. Wang, "Exploiting Filter Stop Band for Radio Frequency Interferometer Operation," *IEEE Sensors Journal,* vol. 15, iss. 10, Oct. 2014.

[2.5] H. Mirzaei, R. Islam, and G. V. Eleftheriades, "Anomalous negative group velocity in coupled positive-index/negative-index guides supporting complex modes," *IEEE Transactions on Antennas and Propagation ,* vol. 59, iss. 9, pp. 3412-3420, Sept. 2011.

[2.6] M. Kitano, T. Nakanishi, and K. Sugiyama, "Negative group delay and superluminal propagation: An electronic circuit approach," *IEEE Journal of Selected Topics in Quantum Electronics,* vol. 9, iss. 1, pp. 43-51, Jan-Feb 2003.

[2.7] H. Uranus and H. Hoekstra, "Modeling of loss-induced superluminal and negative group velocity in two-port ring-resonator circuits," *Journal of Lightwave Technology,* vol. 25, iss. 9, pp. 2376-2384, Sep. 2007.

[2.8] Y. Cui, Y. He, and P. Wang, "A quadrature-based tunable radio-frequency sensor for the detection and analysis of aqueous solutions," *IEEE Microwave and Wireless Components Letters,* vol. 24, iss. 7, pp. 490-492, Jul. 2014.

[2.9] B. Levush, T. M. Antonsen Jr, A. Bromborsky, W.-R. Lou, and Y. Carmel, "Theory of relativistic backward-wave oscillators with end reflectors," *IEEE Transactions on Plasma Science,* vol. 20, iss. 3, pp. 263-280, Jun. 1992.

[2.10] G. Chaudhary, Y. Jeong, and J. Lim, "Microstrip line negative group delay filters for microwave circuits," *, IEEE Transactions on Microwave Theory and Techniques,* vol. 62, iss. 2, pp. 234-243, Feb. 2014.

[2.11] J. Woodley and M. Mojahedi, "Negative group velocity and group delay in left-handed media," *Physical Review E,* vol. 70, iss. 4, Oct. 2004.

[2.12] B. Ravelo, A. Pérennec, M. Le Roy, and Y. G. Boucher, "Active microwave circuit with negative group delay," *IEEE Microwave and Wireless Components Letters,* vol. 17, iss. 12, pp. 861-863, Dec. 2007.

CHAPTER THREE

DESIGN AND ANALYSIS OF MICROSTRIP LINE SENSOR

3.1 Design and Fabrication of Microstrip Sensors

A microstrip line sensor, shown in Fig. 3.1 and 3.2(a), was selected to be the sensing electrode in the microwave flow cytometer discussed in **Chapter V**. Resonators can concentrate the probing fields and improve measurement sensitivity, such as measuring nanometer scale cell membranes [3.1]. But their operating frequencies are limited and not easily tunable, thus inconvenient for frequency searching/sweeping application. Coplanar waveguides (CPWs) are easier to build, yet the measurement signals are sensitive to cell position relative to CPW electrode surface [3.2], and the position is difficult to control. Hence, separating cell intrinsic property variation from position variation in a measurement is challenging. The microstrip arrangement in Fig. 3.1 also has better sensitivity than CPWs sensors [3.3]. The interaction between a cell and the microwave fields varies with cell sizes and vertical location, Fig. 3.2(b), but the variations can be alleviated to tolerable levels by use of larger microstrip width, w. Hence, the microstrip in Fig. 3.2 provides a reasonable tradeoff between sensitivity, field intensity variation, and frequency tunability.

The microstrip electrode in Fig. 3.2(a) is connected to a CPW transition section at each end. The use of CPW is for easier cable connections and has increased design flexibility due to not having a fixed gap between the signal and ground planes, as is the case with the microstrip. It also allows for broadband impedance matching by tapering
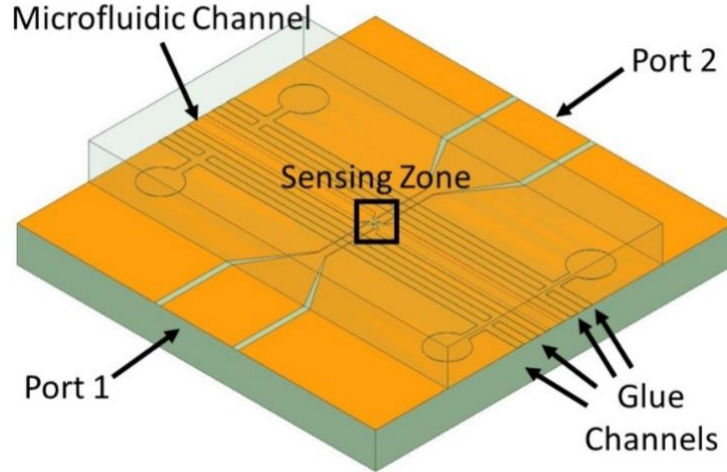
Fig. 3.1. 3-D model of microstrip line sensor used in the microwave flow cytometer. A microstrip electrode in the *Sensing Zone* serves as the sensing structure. A microscope image of the sensing zone is shown in Fig. 3.2(a).

the signal line at the transition section. The tapered section increases the series capacitance, hence increasing the impedance, to account for the lower impedance microstrip section caused by the large permittivity of most cell media [3.4, 3.5].   The microfluidic channel, used to transport fluid and/or cell samples through the sensing zone, extends the width of the 10 mm × 10 mm sensor. The 500-μm-wide channel tapers to a width of 100 μm for a 250-μm-long section passing under the ML, giving a total channel volume of 43.6 nL. Microfluidic tubes inserted at the ends of the channel allow for samples to be injected via a syringe.

The sensor is made of two pieces- a top piece that serves as a cover for the microfluidic channel and contains the signal lines and the CPW ground plane, and a bottom piece that has the microfluidic channel, the microstrip ground, and four additional
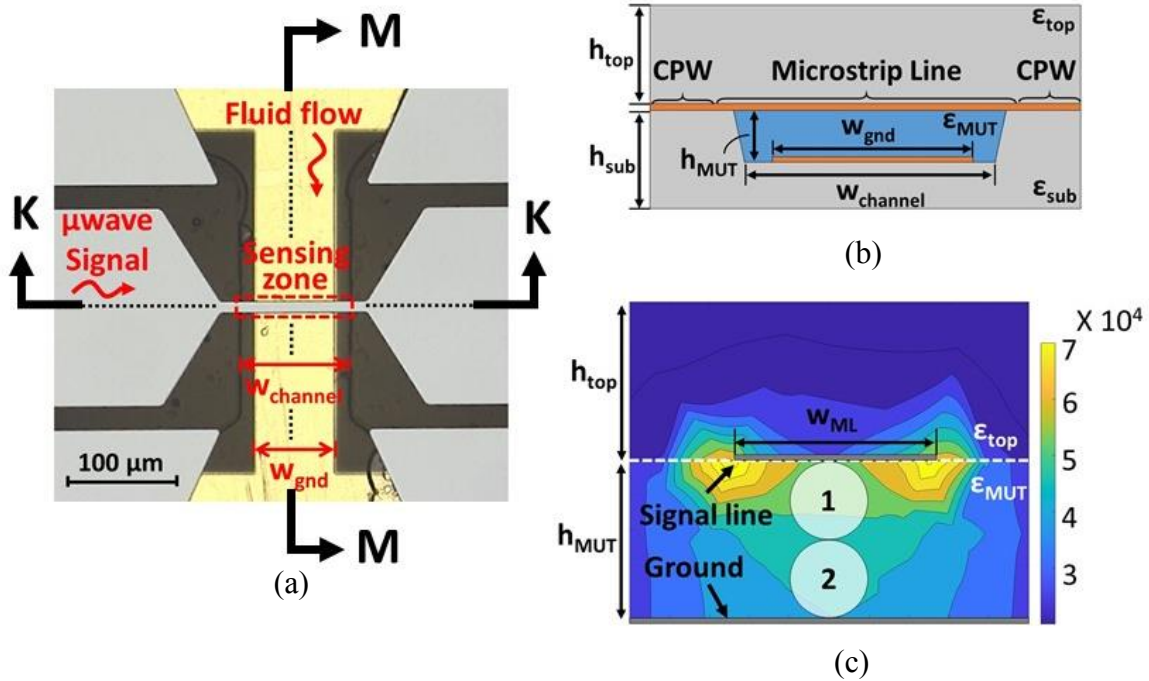
Fig. 3.2 (a) A top view of the sensing zone of the microstrip sensor, (b) K-K cross section of the microfluidic channel showing the layers of the microstrip and the signal line transitions (CPW-Microstrip-CPW), and (c) M-M cross section of the microstrip showing the HFSS simulated electric field intensity.

channels used to adhere the pieces. The sensors were fabricated on 4-inch fused silica wafers using standard microfabrication processes. 20-Cr/200-Au metal was patterned using a liftoff procedure on both wafers to create the signal and ground lines. Five 9-μm-deep channels were etched in the bottom wafer, prior to metal patterning on the bottom wafer, by immersing in concentrated 49 wt% hydrofluoric acid (HF) for 10 minutes. Due to the relatively large etch depth, 5-Cr/100-Pt was used as masking material rather than more commonly used photoresists, since photoresist is easily penetrated by HF at high concentrations [3.6]. Even with a Pt mask for etching, adhesion is a significant issue and

the metalized patterns were often removed prior to the 10-minute etch time. If deeper

channels are required borosilicate glass can be used in place of quartz since the etch rate

is significantly higher, although it exhibits isotropic etch profiles [3.7, 3.8]. We were able

to etch 10-μm channels in SCHOTT Borofloat® wafers by submerging in 49% HF for 90
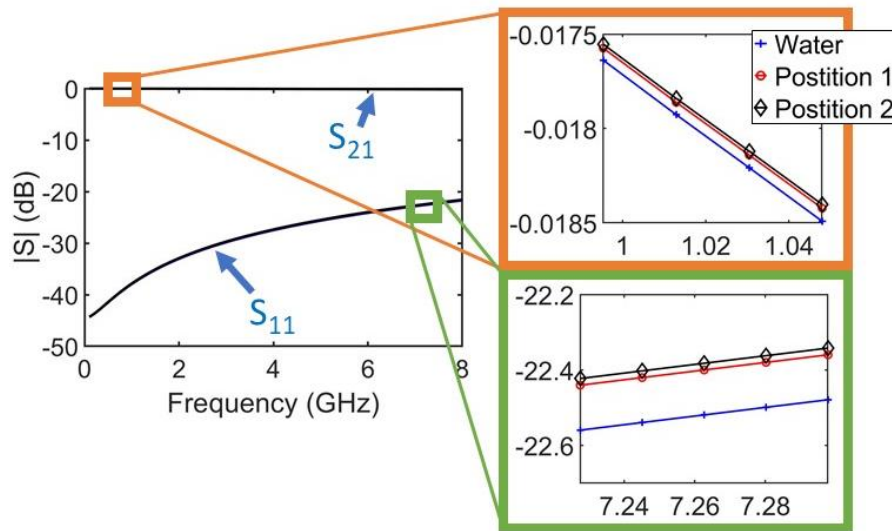
Fig. 3.3 Broadband simulation of the ML section of the sensor for polystyrene particles

($\varepsilon_r = 2.6$) in positions (1) and (2) using water as the reference material ($\varepsilon_{mut} = 81$).

seconds using an AZ P4620 photoresist mask. The fabrication process is summarized in

Fig. 3.4, Table 3.1, and Table 3.2.

The microfluidic channel, labeled $w_{channel}$ in Fig. 3.2(a), runs perpendicular to the

signal line at the center of the sensor. The other four channels are used to adhere the two

pieces together using optical glue. The glue channels are each 200 μm wide and span the

width of the sensor. The bases of the channels are metal coated to create a ground plane

for the microstrip and ensure continuity of the CPW ground. The width of the microstrip

ground, w_{gnd}, is slightly narrower than the microfluidic channel at 80 μm to allow for

misalignment during fabrication. The areas above the channels on the top wafer are left

transparent to allow for viewing under a microscope. After adhering the signal and
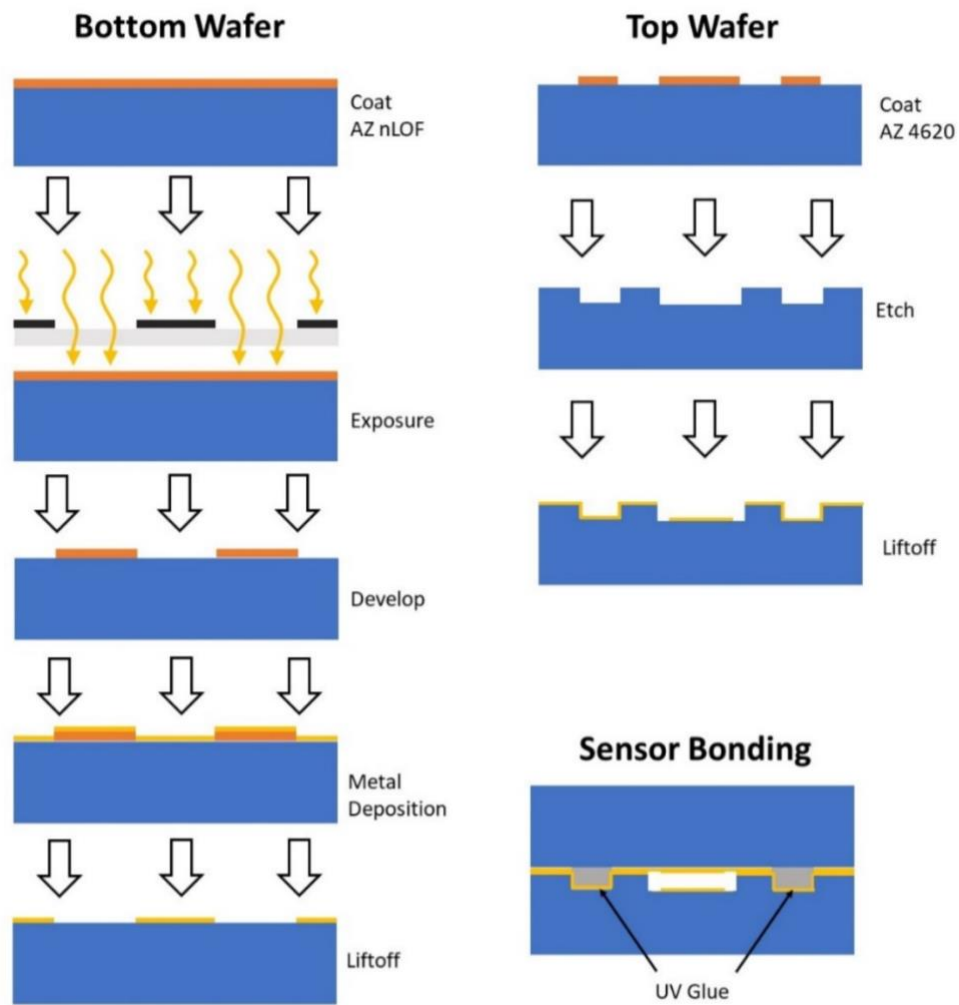
Fig. 3.4. Fabrication process of microstrip sensor. Details of each step is provided in

Table 3.1 and 3.2.

ground pieces, tubes are inserted into drilled holes at the ends of the microfluidic channel, allowing continuous fluid flow through the sensor. The final assembled device is mounted in a brass assembly with SMA connectors, shown in **Fig. 4.2(b). Fig. 3.5** shows the broadband measurement and simulation results of the microstrip line sensor. There was very good agreement between measured and simulated $|S_{21}|$ over the entire operating frequency range and $|S_{11}|$ agrees well below 6 GHz. The differences above this are likely due to effects from the connectors, optical glue, and device imperfections from fabrication, particularly scratches created from drilling the microfluidic channel inlets, being difficult to account for in the simulation.
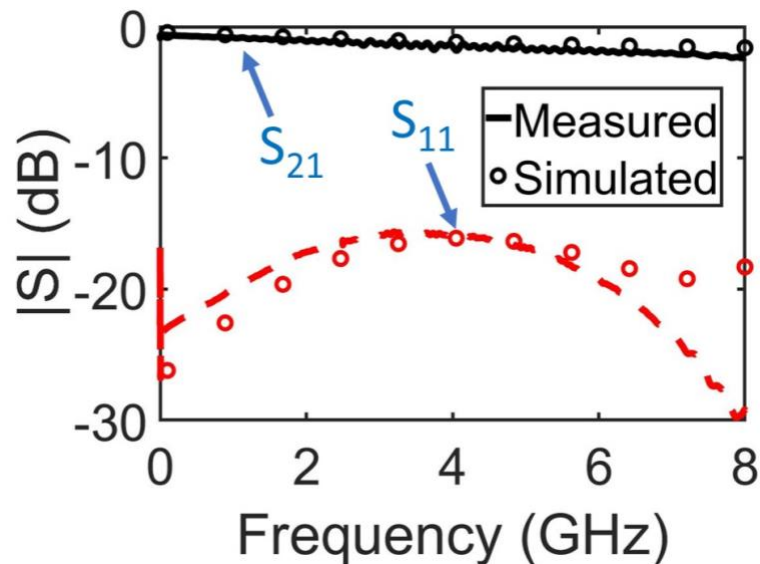
Fig. 3.5. Comparison of measurement and simulation results for the sensing electrode over the operating frequency range.

TABLE 3.1

<div align="center">BOTTOM WAFER ETCH PROCESS</div>

Step	Process Step	Parameters
1	O_2 Clean	150W for 30 sec
2	HMDS	Vapor priming oven
3	Coat AZ P4620 Photoresist	Spin at 2500 rpm, 700 rpm/sec for 60 sec
4	Soft Bake	Hotplate 115°C for 2 min
5	Expose	6 cycles, 5 sec each, 10 sec wait
6	Develop	351:DI 1:3 for 2.5 min
7	Descum	40W for 20 sec
8	Etch	49% HF immersion for 90 sec

TABLE 3.2

<div align="center">LIFTOFF PROCESS</div>

Step	Process Step	Parameters
1	O_2 Clean	150W for 30 sec
2	HMDS	Vapor priming oven
3	Coat AZ nLOF Photoresist	Spin at 1500 rpm for 30 sec
4	Soft Bake	Hotplate 110°C for 60 sec
5	Expose	Expose 6 sec
6	Hard Bake	Hotplate 110°C for 60 sec
7	Develop	351:DI 1:1 for 60 sec
8	Descum	40W for 20 sec
9	Evaporator	20-Cr/200-Au
10	Liftoff	Overnight immersion in remover 1165

3.2 Sensor Modeling

The goal of microwave dielectric spectroscopy measurements is to determine the unknown complex permittivity and impedance of the *material under test* (*mut*). In order

to extract the complex permittivity of materials it is desirable to have a closed form solution relating the relative permittivity to the effective permittivity, the latter of which can be calculated directly from S-parameter measurements. While simulations based on full wave techniques can effectively relate the permittivities, the computational efficiency is low and mesh convergence is often difficult to obtain, especially when the volume fraction of the *mut* is small. In this section static variational methods for planar transmission line structures will be discussed and applied to multilayer microstrips. The method can be used in both the space domain and the Fourier domain, the latter is known as the static spectral domain analysis (SDA).

3.3.1 Static variational method

The variational method is a method based on the calculus of variations that is used to obtain the unknown function of a physical problem formulated as a definite integral under stationary conditions; i.e., under maximum and minimum conditions for a variational integral (functional), and the stationary conditions give the lower and upper bounds of the functional. To determine the function that provides the maximum and minimum (stationary) values of the functional, the variation of the functional must be zero. Then, if the second variation is positive the function provides the minimum value (upper bound) of the functional, if it is negative the function provides the maximum value (lower bound) of the functional, just like when determining the maximum and minimum values of a function in differential calculus. As such, any approximate solution to the functional will be larger (minimum condition) or smaller (maximum condition) than the correct solution.

There are two variational formulations for determining line capacitance, and hence the characteristic impedance Z_0, of transmission lines – the energy method-based variational expression and the Green's function method-based variational expression. The former provides the upper bound of the line capacitance and the lower bound of the characteristic impedance and the latter provides the lower bound of line capacitance and the upper bound of the characteristic impedance, as shown in Fig. 3.6.

$Z_{Green's}/C_{energy}$ **Upper Bound**

↓ Minimize

Z_{true}/C_{true}

↑ Maximize

$Z_{energy}/C_{Green's}$ **Lower Bound**
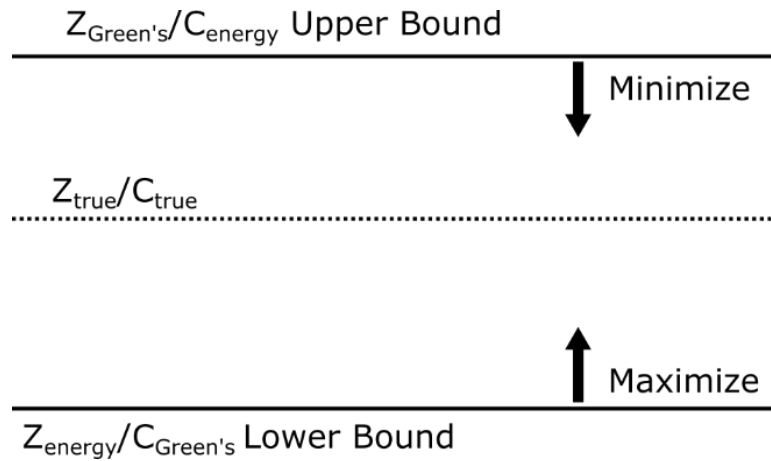
Fig. 3.6. Capacitance and impedance approximations for Green's function and energy-based formulations of variational expressions. The upper bounds should be minimized, and the lower bounds should be maximized for the highest accuracy.

The average value of both the upper and lower bounds of line capacitance using the two methods described here would be the most accurate solution, however, for the sensors described in this chapter using the Green's function method alone was sufficiently accurate.

3.3.2 Green's function method variational expression

In the Green's function method the charge distribution on the conductor is the unknown function that is assumed and treated as the trial function. Assuming that conductor 1 in Fig. 3.7 is grounded and conductor 2 is at potential V_0, giving a charge distribution $\rho(x',y')$ on it's surface.
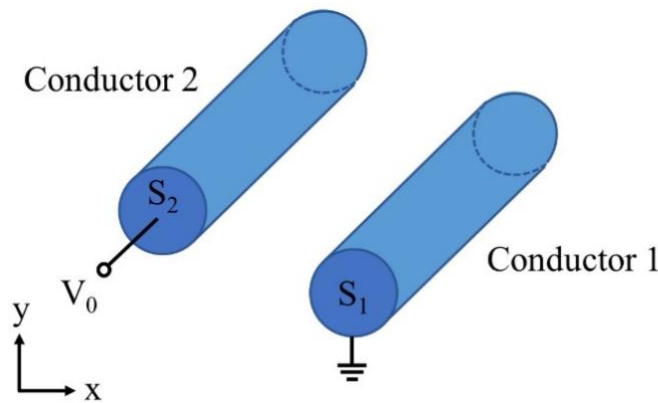
Fig. 3.7. Two conductor transmission line

The fields surrounding the transmission lines are described by the potential function $\Phi(x,y)$, which satisfies Poisson's equation:

$$\nabla_t^2 \Phi(x,y) = -\frac{1}{\varepsilon}\rho(x',y') \tag{3.1}$$

where $\varepsilon = \varepsilon_0\varepsilon_r$, (x',y') is the location of the source, (x,y) is the location of the field, and boundary conditions that Φ is zero on S_1 and at infinity. The charge density excitation on the surface of the conductor is described by Dirac's delta function $\delta(x-x')\delta(y-y')$ and the response to the charge density at location (x,y) is described by the potential Green's function $G(x,y|x',y')$, defined as the solution to

37

$$\nabla_t^2 G(x,y|x',y') = \begin{cases} -\dfrac{1}{\varepsilon}\delta(x-x')\delta(y-y') \\ 0, \qquad x \neq x', y \neq y' \end{cases} \tag{3.2}$$

The Green's function can be thought of as the response to a unit charge density at location (x,y), so then the potential at a given location is the superposition of the potential responses, given as

$$\Phi(x,y) = \oint_{S_2} G(x,y|x',y')\,\rho(x',y')dl' \tag{3.3}$$

Given that the potential on the surface of conductor 2 is V_0, this becomes

$$\Phi(x,y) = V_0 = \oint_{S_2} G(x,y|x',y')\,\rho(x',y')dl' \tag{3.4}$$

Equation (3.4) is an integral equation with unknown charge distribution $\rho(x',y')$. From this, we get the variational expression for capacitance by multiplying by $\rho(x,y)$, integrating over S_2, and using the definition $QV_0 = Q^2/C$ [3.9]

$$\frac{1}{C} = \frac{\oiint_{S_2} G(x,y|x',y')\rho(x,y)\rho(x',y')dl\,dl'}{\left[\oint_{S_2}\rho(x,y)dl\right]^2} \tag{3.5}$$

or in terms of the potential function

$$\frac{1}{C} = \oint_{S_2} \Phi(x,y)\,\rho(x',y')dl \tag{3.6}$$

Because the Green's function method provides the lower bound of line capacitance (and upper bound of impedance), the computed line capacitance will always be less than the true value of capacitance, thus the coefficients of the trial charge distribution function should be optimized to maximize the line capacitance.

3.3.3 Green's function method variational expression in the Fourier domain

The Fourier transform of the function $f(x,y)$ with respect to a continuous variable x over the range $(-\infty,\infty)$ and its inverse are defined as

$$\tilde{f}(\beta,y) = \int_{-\infty}^{\infty} \Phi(x,y)e^{j\beta x}dx \tag{3.7}$$

$$f(x,y) = \frac{1}{2\pi}\int_{-\infty}^{\infty} \widetilde{\Phi}(\beta,y)e^{-j\beta x}d\beta \tag{3.8}$$

where β is the Fourier variable. The Fourier transform of Poisson's equation then gives the ordinary differential equation

$$\frac{d^2\widetilde{\Phi}(\beta,y)}{dy^2} - \beta^2\widetilde{\Phi}(\beta,y) = -\frac{1}{\varepsilon}\tilde{f}(\beta)\delta(y-y') \tag{3.9}$$

where $\widetilde{\Phi}(\beta,y)$ and $\tilde{f}(\beta)$ are the potential and charge distribution, respectively, in the Fourier domain. Then, the variational expression in the Fourier domain be found by applying Parseval's theorem to Equation (3.6) giving

$$\frac{1}{C} = \frac{1}{2\pi Q^2}\int_{-\infty}^{\infty} \widetilde{\Phi}(\beta,y')\tilde{f}(\beta)d\beta \tag{3.10}$$

where y' is the location of the conductor containing the charge distribution and the potential in the Fourier domain is

$$\widetilde{\Phi}(\beta,y') = \tilde{G}(\beta,y')\tilde{f}(\beta) \tag{3.11}$$

where $\tilde{G}(\beta,y')$ is the Green's function in the Fourier domain. Assuming a symmetrical charge distribution, i.e. $\tilde{f}(-\beta) = \tilde{f}(\beta)$, the variational expression for capacitance in the Fourier domain is

$$\frac{1}{C} = \frac{1}{\pi} \int_0^\infty \left[\frac{\tilde{f}(\beta)}{Q} \right]^2 \tilde{G}(\beta, y') d\beta \qquad (3.12)$$

To solve Equation (3.12) for the line capacitance we must assume a trial charge

distribution, $[\tilde{f}(\beta)/Q]$. Several charge distributions and their Fourier transform have

been presented, including constant [3.10], linear [3.11], cubic [3.12], Maxwell's [3.13],

and others. Since the charge distribution on a strip conductor is symmetrical and has

singularities at the strip edges, ideally a charge distribution would be chosen to represent

that behavior, such as Maxwell's distribution function. However, the cubic charge

distribution was chosen to model the multilayer microstrip line sensor since it has been

shown to be sufficiently accurate and is much simpler to implement. The cubic charge

distribution is defined as

$$f(x) = \begin{cases} 1 + A \left| \dfrac{x}{w/2} \right|^3, & -w/2 \le x \le w/2 \\ 0, & |x| > w/2 \end{cases} \qquad (3.13)$$

where w is the strip width and A is a constant. Assuming A = 1, the Fourier transform of

Equation (3.13) is

$$\tilde{f}(\beta) = \frac{4}{\beta} \sin \left(\frac{\beta w}{2} \right) + \frac{12}{w\beta^2} \times$$
$$\left\{ \cos \left(\frac{\beta w}{2} \right) - \frac{4}{\beta w} \sin \left(\frac{\beta w}{2} \right) + \frac{16}{(\beta w)^2} \sin^2 \left(\frac{\beta w}{4} \right) \right\} \qquad (3.14)$$

The total charge *p.u.l.* is

$$Q = \int_{-w/2}^{w/2} \left(1 + \left| \frac{2x}{w} \right|^3 \right) dx = \frac{5w}{4} \qquad (3.15)$$

Finally, the normalized charge distribution function in the Fourier domain is

$$\frac{\tilde{f}(\beta)}{Q} = \frac{8}{5} \cdot \frac{\sin\left(\frac{\beta w}{2}\right)}{\frac{\beta w}{2}} + \frac{12}{5\left(\frac{\beta w}{2}\right)^2} \times$$

$$\left\{\cos\left(\frac{\beta w}{2}\right) - 2\left[\frac{\sin(\beta w/2)}{\beta w/2}\right] + \left[\frac{\sin(\beta w/4)}{\beta w/4}\right]^2\right\} \tag{3.16}$$

So to determine the line capacitance of a transmission line using the Green's function method variational expression, the Green's function of the problem must first be determined using Equation (3.9). Then the Green's function and trial charge distribution function are substituted into Equation (3.12).

3.3.4 The Transverse Transmission Line Method

To determine the Green's function of multilayer structures, the transverse transmission line (TTL) techniques is employed. The TTL method, first introduced by Chang and Change [3.14], is a convenient and simple method that uses an equivalent multi-section transmission line circuit to find the Green's function of a multi-layer structure. TTL can be used to calculate the Green's function in both the space domain and the Fourier domain, the latter of which is presented here and used for a multilayer microstrip line.

The equivalency in this technique is due to the similarity between Poisson's equation (Equation (3.9)) and the Kelvin–Heaviside voltage wave equation for a transmission line excited by a current source [3.15]

$$\frac{d^2V}{dy^2} - \gamma^2V = -\gamma\frac{1}{Y_0}I_s\delta(y - y') \tag{3.17}$$

Comparing Equations (3.9) and (3.17) gives the following equivalences

TABLE 3.3

<div align="center">

EQUIVALENT PARAMETERS

Poisson's Equation		Transmission Line
$\widetilde{\Phi}(\beta, y')f$	$\equiv$	V
β	$\equiv$	γ
ε	$\equiv$	Y_0
$\tilde{f}(\beta)/\beta$	$\equiv$	I_s

</div>

Since the charge on the strip is equivalent to a current source at the microstrip conductor

location, the voltage at strip location y' is

$$V(y = y') = \frac{I_s}{Y} \tag{3.18}$$

so the potential function equivalence is

$$\widetilde{\Phi}(\beta, y = y') = \tilde{f}(\beta)\widetilde{G}(\beta, y) \tag{3.19}$$

where

$$\widetilde{G}(\beta, y) = \frac{1}{\beta Y} \tag{3.20}$$

Substituting Equation (3.20) into Equation (3.12) gives the variational expression in

terms of the admittance parameter Y as follows

$$\frac{1}{C} = \frac{1}{\pi\varepsilon_0} \int_0^\infty \frac{\left[\tilde{f}(\beta)/Q\right]^2}{\beta Y} d\beta \tag{3.21}$$

This method can be applied to determine the Green's function of multilayer

microstrips without sidewalls, as shown in Fig. 3.8(a)-(b). The top and bottom surfaces

can be modeled as either a short circuit or an open circuit, corresponding to an electric
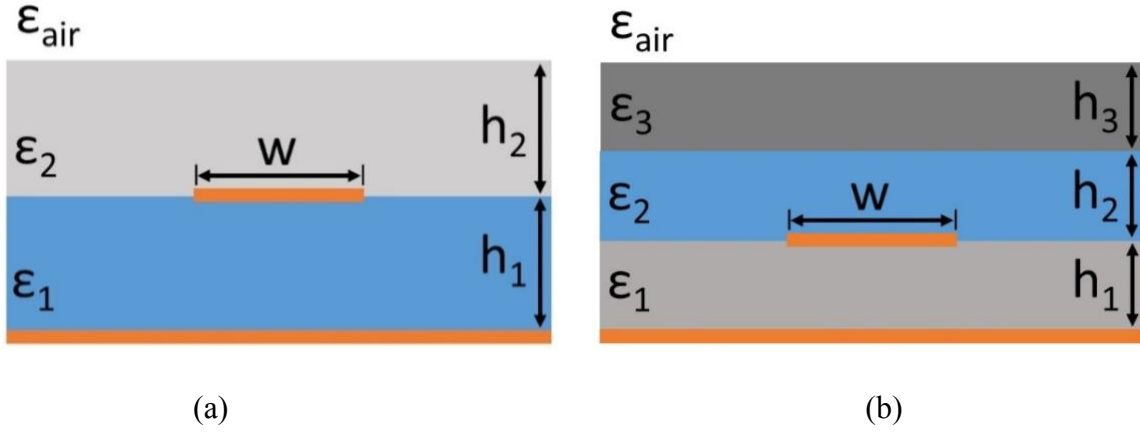
Fig. 3.8. Cross section of (a) two-layer and (b) three-layer microstrips with bottom
ground planes (electric wall) and unshielded (magnetic wall) top. The corresponding
equivalent transmission line circuits are shown in Fig. 3.9.

wall (PEC) or magnetic wall (PMC), respectively, at the ends of the equivalent
transmission lines. The admittance of a lossy transmission line is defined as

$$Y_{in} = Y_0 \frac{Y_L + Y_0 \tanh \gamma l}{Y_0 + Y_L \tanh \gamma l} \tag{3.22}$$

so the admittances of an electric wall ($Y_L \to \infty$) and a magnetic wall ($Y_L \to 0$) are

$$Y_{in}^{EW} = Y_0 \coth \gamma l \tag{3.23}$$

$$Y_{in}^{MW} = Y_0 \tanh \gamma l \tag{3.24}$$

For an unshielded microstrip, where $\varepsilon_r = 1$ and $h = \infty$, Eq. 3.26 gives admittance $Y_{in} = 1$.
For the unshielded two-layer microstrip in Fig. 3.9(a) the admittance function Y is

$$Y = Y_a + Y_b = \varepsilon_{r2} \frac{1 + \varepsilon_{r2} \tanh \beta h_2}{\varepsilon_{r2} + \tanh \beta h_2} + \varepsilon_{r1} \coth \beta h_1 \tag{3.25}$$
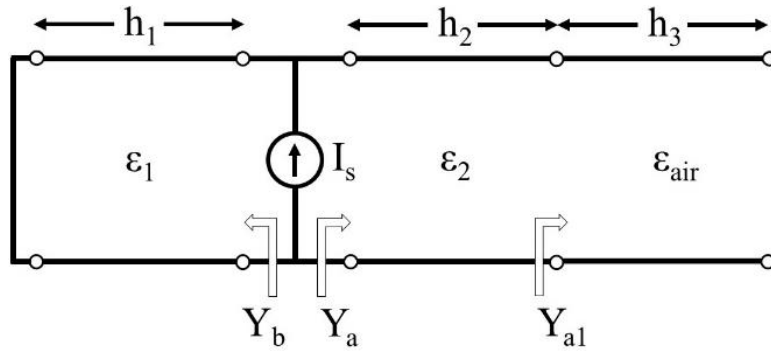
(a)
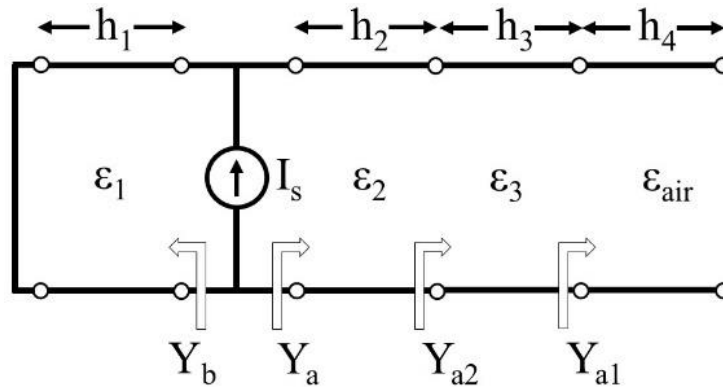
(b)

Fig. 3.9. Equivalent transmission line models of (a) two-layer and (b) three-layer microstrips with bottom ground planes (electric wall) and unshielded (magnetic wall) tops used to determine the admittance functions.

where

$$Y_a = \varepsilon_{r1} \frac{Y_{a1} + \varepsilon_{r2} \tanh \beta h_2}{\varepsilon_{r2} + Y_{b1} \tanh \beta h_2} = \varepsilon_{r1} \frac{1 + \varepsilon_{r2} \tanh \beta h_2}{\varepsilon_{r2} + \tanh \beta h_2} \qquad (3.26)$$

$$Y_b = \varepsilon_{r1} \coth \beta h_1 \qquad (3.27)$$

Similarly, the admittance function of the unshielded three-layer microstrip in Fig. 3.8(a)

$$Y = \varepsilon_{r2} \frac{Y_{a2} + \varepsilon_{r2} \tanh \beta h_2}{\varepsilon_{r2} + Y_{a2} \tanh \beta h_2} + \varepsilon_{r1} \coth \beta h_1 \tag{3.28}$$

where

$$Y_{a2} = \varepsilon_{r3} \frac{1 + \varepsilon_{r3} \tanh \beta h_3}{\varepsilon_{r3} + \tanh \beta h_3} \tag{3.29}$$

This method can be used for n-layer microstrips with or without a top shield so long as the assumptions of infinitely wide substrates and a thin conductive strip are valid. The static dielectric constant and characteristic impedance of a multilayer microstrip without sidewalls are given by

$$\varepsilon_{eff} = \frac{C}{C_0} \tag{3.30}$$

and

$$Z_0 = \frac{1}{c\sqrt{CC_0}} = \frac{Z_0(\varepsilon_r = 1)}{\sqrt{\varepsilon_{eff}}} \tag{3.31}$$

where C_0 is the line capacitance *p.u.l.* with the substrate replaced by air and c is the speed of light in free space. This method can also be applied to various other single- and multi-layer planar transmission line structures such as CPWs, coupled striplines, and slotlines [3.10, 3.16-3.24].

References

[3.1]   Y. Cui, W. F. Delaney, T. Darroudi, and P. Wang, "Microwave measurement of giant unilamellar vesicles in aqueous solution," *Scientific Reports,* vol. 8, Jan. 2018.

[3.2] Z. Wang et al., "Time domain detection and differentiation of single particles and cells with a radio frequency interferometer," *2016 IEEE Topical Conference on Biomedical Wireless Technologies, Networks, and Sensing Systems (BioWireleSS)*, Austin, TX, USA, Jan. 2016, pp. 77-80.

[3.3] C. Song, J. E. Harriss, and P. Wang, "Compensating on-chip transmission line losses for a high-sensitivity microwave sensor," *Sensors and Actuators A: Physical,* vol. 154, no. 1, pp. 7-11, Aug. 2009.

[3.4] G. Zheng, J. Papapolymerou and M. M. Tentzeris, "Wideband coplanar waveguide RF probe pad to microstrip transitions without via holes," *IEEE Microwave and Wireless Components Letters*, vol. 13, no. 12, pp. 544-546, Dec. 2003.

[3.5] X. Bao *et. al.*, "Broadband Dielectric Spectroscopy of Cell Cultures," *IEEE Transactions on Microwave Theory and Techniques*, vol. 66, no. 12, pp. 5750-5759, Dec. 2018.

[3.6] H. Zhu, M. Holl, T. Ray, S. Bhushan, and D. Meldrum, "Characterization of deep wet etching of fused silica glass for single cell and optical sensor deposition," *Journal of Micromechanics and Microengineering*, vol. 19, no. 6, Jun. 2009.

[3.7] V. Hagglund, "Characterization of masking layers for deep wet etching in borofloat glass," *Uppsala Universitet, Examensarbete*, vol. 30, pp. 1–36, 2013.

[3.8] J.M. Nagarah and D.A. Wagenaar, "Ultradeep fused silica glass etching with an HF-resistant photosensitive resist for optical imaging applications," *Journal of Micromechanics and Microengineering*, vol. 22, Feb. 2012.

[3.9] R.E. Collin, *Field Theory of Guided Waves*, 2nd ed., New York: Wiley-IEEE Press, 1991.

[3.10] T. Itoh and R. Mitra, "An accurate method for calculating charge and potential distributions in coupled microstrip lines," *Proceeding of the IEEE*, vol. 59, iss. 2, pp. 332–334, Feb. 1971.

[3.11] E. Yamashita and R. Mitra, "Variational method for analysis of microstrip lines," *IEEE Transactions on Microwave Theory and Techniques*, vol. MTT-16, iss. 4, pp. 251–256, April 1968.

[3.12] E. Yamashita, "Variational method for analysis of microstrip – like transmission lines," *IEEE Transactions on Microwave Theory and Techniques*, vol. 16, iss. 8, pp. 529–535, Aug. 1968.

[3.13] E.J. Denlinger, "A frequency-dependent solution for microstrip transmission lines," *IEEE Transactions on Microwave Theory and Techniques*, vol. 19, iss. 1, pp. 30–39, Jan. 1971.

[3.14] Y. Chang and I.E. Chang, "Simple method for the variational analysis of a generalized N- dielectric layer transmission line," *Electronics Letters*, vol. 6, iss. 3, pp. 49–50, Feb. 1970

[3.15] D. M. Pozar, *Microwave Engineering*, 4th ed., New York: Wiley, 2012.

[3.16] T.G. Bryant and J.A. Weiss, "Parameters of microstrip transmission lines and of coupled pairs of microstrip lines," *IEEE Transactions on Microwave Theory and Techniques*, vol. 16, iss. 12, pp. 1021–1027, 1968.

[3.17] S.K. Koul and B. Bhat, "Propagation parameters of coupled microstrip-like transmission lines for millimeter-wave applications," *IEEE Transactions on Microwave Theory and Techniques*, vol. 29, iss. 12, pp. 1364–1370, Dec. 1981.

[3.18] K.C. Gupta, R. Garg, and I.J. Bahl, *Microstrip Lines and Slotlines*, 4th ed., Boston, Massachusetts: Artech House Publishers, 2013.

[3.19] R. Garg and I.J. Bah, "Characteristics of coupled microstrip lines," *IEEE Transactions on Microwave Theory and Techniques*, vol. 27, iss. 7, pp. 700–705, 1979.

[3.20] I.J. Bahl and P. Bhartia, "Characteristics of inhomogeneous –coupled stripline," *IEEE Transactions on Microwave Theory and Techniques*, vol. 28, iss. 6, pp. 529–535, June 1980.

[3.21] A. Sawicki and K. Sachse, "Lower and upper bound calculations on the capacitance of multiconductor printed transmission line using the spectral-domain approach and variational method," *IEEE Transactions on Microwave Theory and Techniques*, vol. 34, iss. 2, pp. 236–244, Feb. 1986.

[3.22] A.K. Verma, Nasimuddin and R.K. Ojha, "Synthesis and analysis of optimum directivity suspended microstrip coupler," *2000 Asia-Pacific Microwave Conference Proceedings (APMC)*, Sydney, Australia, Dec. 2000, pp. 1178–1182.

[3.23] C. Nguyen, Analysis Methods for RF, Microwave, and Millimetre – Wave Planar Transmission Lines, 1st ed., New York: John Wiley & Sons, 2000.

[3.24] I. Kneppo, J. Fabian, P. Bezousek, P. Hrnicko, and M. Pavel, *Microwave Integrated Circuits*, 4th ed., London: Springer, 1994.

[3.25] A.K. Verma, *Introduction to Modern Planar Transmission Lines*, 1st ed., New York: Wiley-IEEE Press, 2021.

CHAPTER FOUR

MICROWAVE FLOW CYTOMETER

Fig. 4.1(a) shows a schematic of the microwave flow cytometer using a microwave interferometer and a microstrip line sensor. The operating principle for the microwave interferometer is described in Chapter II and the microstrip sensor is described in Chapter III. For the microwave flow cytometer system, the microstrip sensor is placed in the shorter path of the interferometer and an attenuator is used in the reference (*ref*) path to balance the loss between the two paths to maximize measurement signal-to-noise ratio (SNR).

(a)   (b)
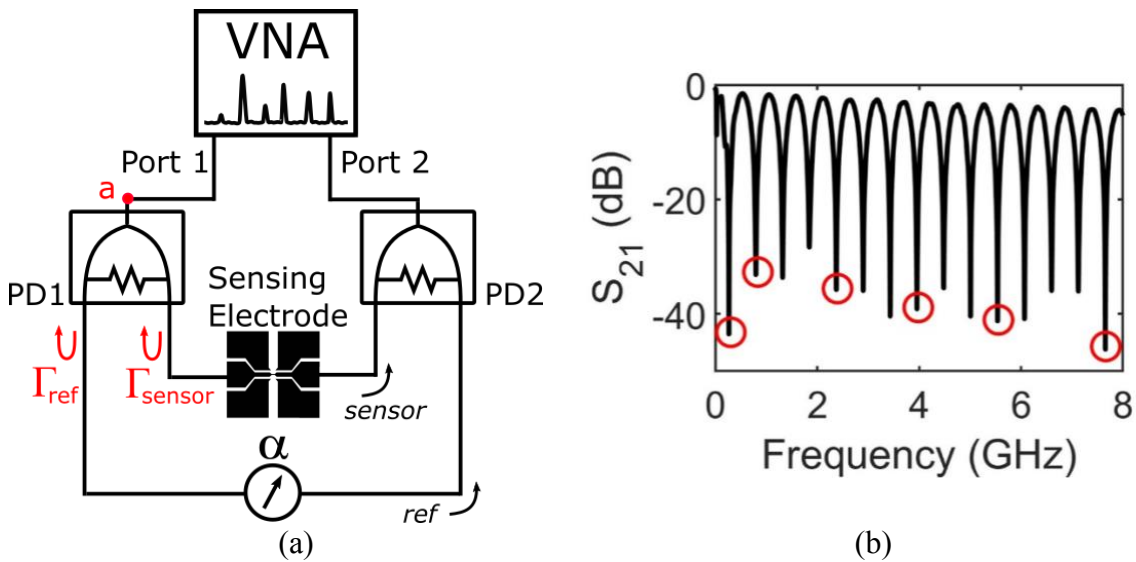
Fig. 4.1. (a) The schematic of the microwave interferometer used in the flow cytometer. A VNA is used to generate and detect single frequency probing signals. The operating frequencies are the minimum points circled in (b) the broadband system response.

With the microstrip sensor in the interferometer in Fig. 4.1(a), the path lengths were fixed such that the interferometer had a fundamental frequency of 265 MHz, with harmonics approximately every 530 MHz, as shown in Fig. 4.1(b). This allowed for easy switching between operating frequencies over a wide range of frequencies. A tunable phase shifter could be added in series with the attenuator if increased frequency tunability is desired. The full flow cytometer system, with the interferometer constructed from connectorized RF components and the microstrip line sensor described in Chapter III, is shown in Fig. 4.2.

(a)

(b)
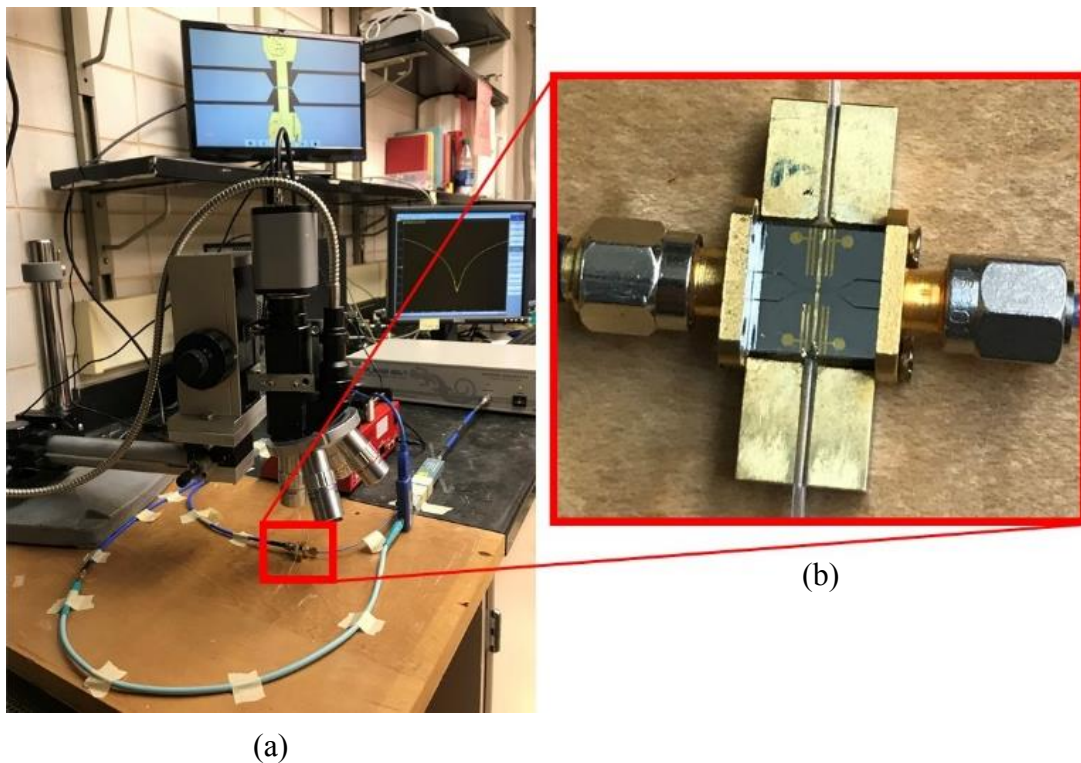
Fig. 4.2. (a) Benchtop assembly showing the interferometer setup with VNA, microscope, and (b) the final assembled microstrip line sensor.

4.1 Permittivity and Impedance Extraction

The primary function of the microwave flow cytometer is to extract microwave properties of single biological cells in a microfluidic sensor. The analytical formulation for the microstrip described in Chapter III can be used to relate the S-parameters that are measured with a VNA to the complex permittivity and impedance of a liquid *mut* in the sensing zone of the microstrip sensor. The permittivity and impedance of the *mut* can be extracted from the measured frequency spectrum using the process described in Chapter II. However, that process requires that every component in the system be characterized. Any disturbance of the system, such as moving cables or components, or fluctuations in room temperature, would change system parameters and required it to be recharacterized. A much simpler and more effective approach is to use calibration standards prior to measurements. This approach also has the advantage of not requiring frequency domain measurements, allowing for the continuous time-domain measurements required for flow cytometry measurements. The calibration process and transmission line parameters for any sensor in an RF interferometer system is described in the following sections.

4.1.1 RF interferometer calibration

In order to obtain permittivity information, $\varepsilon(f) = \varepsilon'(f) - j\varepsilon''(f)$, from measured S-parameters, first the effective substrate permittivity of the sensor is extracted. The sensor's propagation constant, $\gamma = \alpha + j\beta$, can be obtained from the measured S_{21}. The output at port 2 of the interferometer in Fig. 4.1(a) is [4.1]

$$S_{21} = A_{mut}e^{-\gamma_{mut}l_{mut}} + A_{ref} \tag{4.1}$$

where the subscript *mut* and *ref* refer to the material under test and the reference material, respectively. The complex constants A_{mut} and A_{ref} are the normalized transmission coefficients of the two paths. The transmission coefficient of the sensor is described by the term $e^{-\gamma_{mut}l_{mut}}$. These constants can be eliminated by using two calibration standards with known propagation constants by

$$\frac{S_{21mut} - S_{21cal1}}{S_{21cal2} - S_{21cal1}} = \frac{A_{mut}e^{-\gamma_{mut}l_{mut}} + A_{ref} - A_{mut}e^{-\gamma_{cal1}l_{cal1}} - A_{ref}}{A_{mut}e^{-\gamma_{cal2}l_{cal2}} + A_{ref} - A_{mut}e^{-\gamma_{cal1}l_{cal1}} - A_{ref}}$$
$$= \frac{e^{-\gamma_{mut}l_{mut}} - e^{-\gamma_{cal1}l_{cal1}}}{e^{-\gamma_{cal2}l_{cal2}} - e^{-\gamma_{cal1}l_{cal1}}} \tag{4.2}$$

where the *cal1* and *cal2* subscripts refer to the signals from two calibration solutions. Solving for $\gamma_{mut}l_{mut}$ gives

$$\gamma_{mut}l_{mut} = ln\left[\left(\frac{S_{21mut} - S_{21cal1}}{S_{21cal2} - S_{21cal1}}\right)\left(e^{-\gamma_{cal2}l_{cal2}} - e^{-\gamma_{cal1}l_{cal1}}\right)\right.$$
$$\left. - e^{-\gamma_{cal1}l_{cal1}}\right]. \tag{4.3}$$

The effective complex permittivity is then determined from γ_{mut} by [4.2]

$$\varepsilon_{eff}' = \frac{\beta^2 - \alpha^2}{\omega^2\mu_0\varepsilon_0} \tag{4.4}$$

and

$$\varepsilon_{eff}'' = \frac{2\alpha\beta}{\omega^2\mu_0\varepsilon_0}. \tag{4.5}$$

This result is the effective permittivity of the portion of the sensor containing *mut*, which assumes a homogeneous medium surrounding the electrode (Fig. 4.3). Since the effective

permittivity is the averaged permittivity of the sensing zone it includes effects of the glass

substrate. The effective permittivity is then used to determine the relative permittivity of

the medium, which removes the permittivity contribution from the substrate. The above

analysis is valid for any sensor in an interferometer system, provided the impedance

changes during measurements are small enough that reflections can be ignored.

Extracting the permittivity of the medium from the effective permittivity, however, is

dependent on the device geometry.
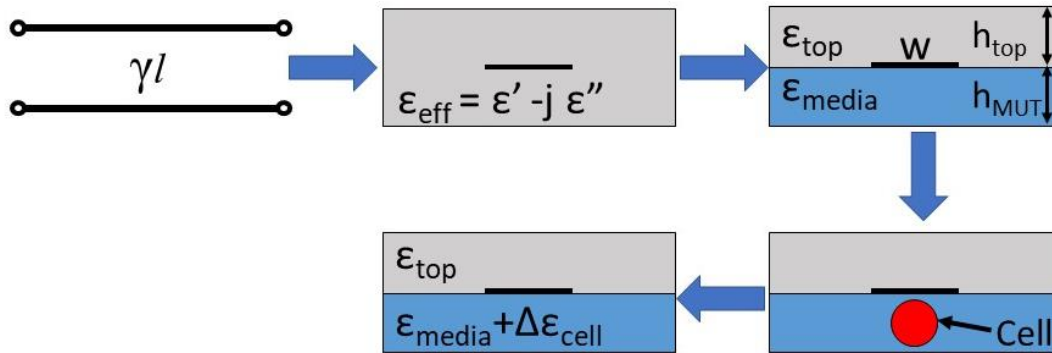
Fig. 4.3. Cell permittivity determination process. The schematic starts at the transmission

line model. The parameter γl is calculated from S_{21} using Eq. 4.2. This parameter is used

to obtain ε_{eff}, which describes the permittivity of a microstrip if it were surrounded by a

homogeneous medium. Equations (4.6)-(4.10) are used to determine the media

permittivity, ε_{media}, prior to cell measurements, where a cell is represented by the circle.

The thickness and permittivity of the glass cover, h_{top} and ε_{top}, the channel height, h_{mut},

and the electrode width, w, are constants defined by the device geometry and materials.

When a cell passes under the electrode the overall *mut* permittivity changes, labeled as

$\Delta\varepsilon_{cell}$.

Closed form solutions based on conformal mapping are commonly used to relate effective and relative permittivity of microstrip devices; however, these models are typically intended for single layer microstrips. For multi-layered structures curve fitting techniques can be used, but this is a difficult endeavor. Due to the multilayer structure of the microstrip and the large permittivity of the mediums we found the variational method in the Fourier domain along with the transverse transmission line (TTL) technique [4.3], described in Chapter III, to be more accurate than conformal mapping-based models and more computationally efficient compared to full-wave electromagnetic methods. Since the microstrip line is embedded in an inhomogeneous medium the propagating mode is approximated as quasi-TEM, for which the effective permittivity is related to the capacitance by [4.4]

$$\varepsilon_{eff} = \frac{C}{C_0} \tag{4.6}$$

where C is the capacitance of the multilayered microstrip line per unit length and C_0 is the capacitance of the microstrip line with all dielectric layers replaced by air. The capacitance of the microstrip line can then be determined from the variational expression of line capacitance in the Fourier domain discussed in Chapter III. The Y-admittance parameter for the two-layer microstrip from equation (3.25) is

$$Y^* = \varepsilon_{mut} \coth(\beta h_{mut}) + \varepsilon_{top} \left\{ \frac{\varepsilon_{top} + \coth(\beta h_{top})}{1 + \varepsilon_{top} \coth(\beta h_{top})} \right\} \tag{4.7}$$

where h_{top} (1 mm) and h_{mut} (9 μm) are the substrate and channel thicknesses, respectively, and ε_{top} is the dielectric constant of the glass substrate.

So, the effective permittivity, ε_{eff}, is determined from S-parameter measurements using Equations (4.1)-(4.5), then ε_{mut} is obtained using look up tables. Due to the complexity of Equation (3.21) there is no closed form expression for ε_{mut} so look up tables were used to determine ε_{mut} from the measured ε_{eff}. The variational method model for the microstrip sensor was used to generate two tables, one relating ε'_{mut} and ε'_{eff}, and one for ε''_{mut} and ε''_{eff}, by sweeping one of the values of ε_{mut} (real or imaginary), and calculating the corresponding part of ε_{eff}. The maximum error created by using the tables was found to be less than 0.01% for ε' and less than 0.5% for ε''. The permittivity extraction process is summarized in Fig. 4.3. When a cell passes under the electrode the overall *mut* permittivity changes. The cell measurements discussed in this dissertation are referring to the peak change in permittivity, $\Delta\varepsilon_{cell}$, which occurs when the cell is centered under the electrode.

The measured propagation constant is also used to determine the impedance of the medium. The potential at point *a* in Fig. 4.1(a) is [4.7]

$$S_{11} = B_{mut}\Gamma_{mut} + B_{ref}\Gamma_{ref}, \tag{4.8}$$

where Γ_{mut} and Γ_{ref} are the reflection coefficients at the inputs of the sensor path and the reference line in Fig. 4.1(a), and the constants B_{mut} and B_{ref} describe all other components in the system. The constants are calibrated out using the same two calibration materials by

$$\frac{S_{11}^{mut} - S_{11}^{cal1}}{S_{11}^{cal2} - S_{11}^{cal1}} = \frac{\Gamma_{mut} - \Gamma_{cal1}}{\Gamma_{cal2} - \Gamma_{cal1}}, \tag{4.9}$$

with reflection coefficients defined as

$$\Gamma_{mut,cal} = \frac{Z_{in}^{mut,cal} - Z_0}{Z_{in}^{mut,cal} + Z_0}, \tag{4.10}$$

and input impedances

$$Z_{in}^{mut,cal} = Z_{mut,cal} \frac{Z_L + Z_{mut,cal} \tanh \gamma_{mut,cal} l_{mut,cal}}{Z_{mut,cal} + Z_L \tanh \gamma_{mut,cal} l_{mut,cal}}. \tag{4.11}$$

So, Equations (4.9) and (4.10) are used to determine the input impedance of the sensor, Z_{in}^{mut}, then Equation (4.11) is solved numerically to get the complex impedance of the *mut*, Z_{mut}. For calibration, the impedance of the microstrip line is determined from Equation (3.31). The permittivity and impedance extraction process are summarized in Fig. 4.4.
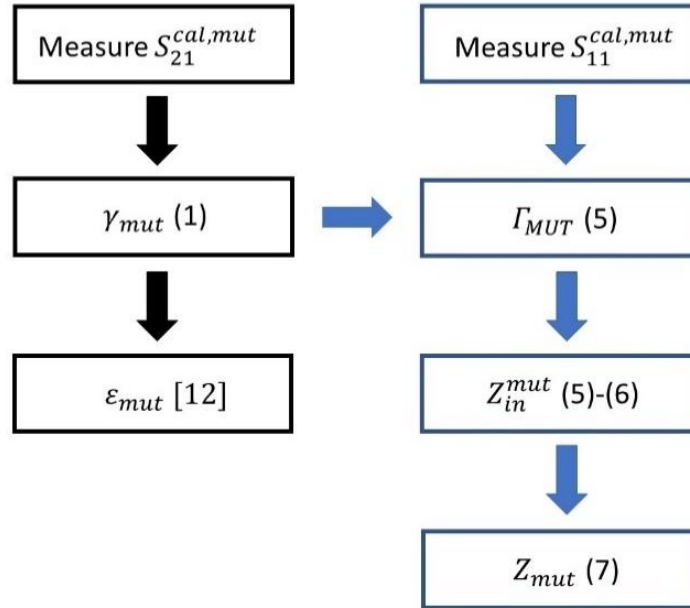
Fig. 4.4. Algorithm to determine the permittivity ε_{mut} and complex impedance Z_{mut} from S-parameter measurements.

To validate the model described above the effective permittivity, ε_{eff}, was calculated from relative permittivities, ε_{mut}, and compared with simulation using ANSYS High Frequency Structural Simulator (HFSS). The microstrip line was simulated by sweeping the real and imaginary parts of ε_{mut} and calculating ε_{eff} using Equations (4.4) and (4.5), and the propagation constant γ from HFSS using [4.6]

$$f_0 = \frac{nc}{2l_{mut}\sqrt{\varepsilon'_{eff}}}$$

(4.12)

where f_0 is the resonance frequency due to reflections, c is the speed of light in free space ($\sim 3 \times 10^8$ m/s), and n is the harmonic integer.

(a)   (b)
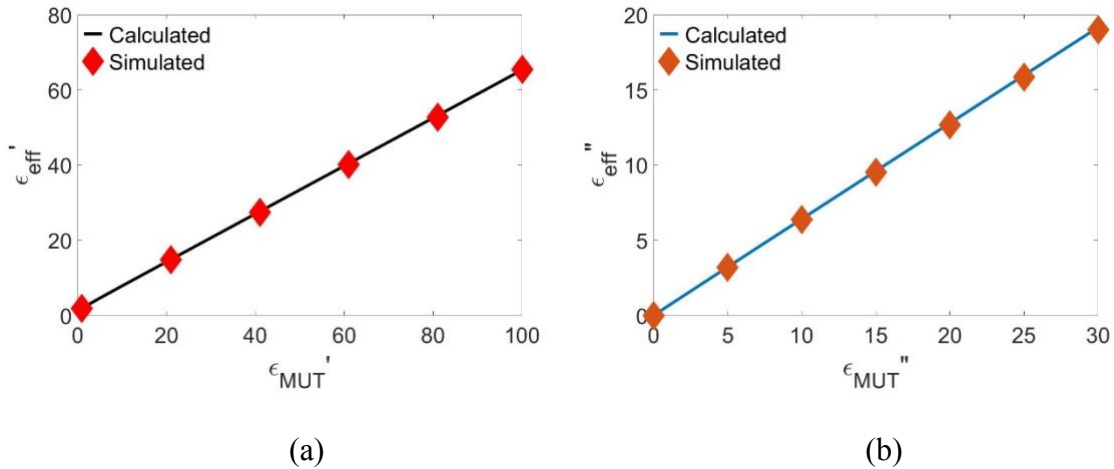
Fig. 4.5. Comparison of variational method models against HFSS simulation of effective permittivities (a) ε'_{eff} and (b) ε''_{eff} vs. relative permittivities ε'_{mut} and ε''_{mut} for the two-layer microstrip line sensor. The permittivity model described in Chapter III shows good agreement with HFSS simulation.

The simulated and calculated values for ε_{eff} for the two-layer microstrip configuration described in Chapter III are plotted in Fig. 4.5, where $W_{ML} = 10$ μm, $h_{mut} = 9$ μm, $h_{top} = 1$ mm, $\varepsilon_{top} = 3.78$, and ε_{mut} represents the unknown material permittivity in the sensor. To validate the permittivity extraction technique for the full microwave flow cytometer system with an RF interferometer, broadband permittivity measurements of isopropyl alcohol (IPA) and ethyl alcohol were compared with measurements from [4.5], shown in Fig. 4.6.

(a)　　　　　　　　　　　　　　(b)
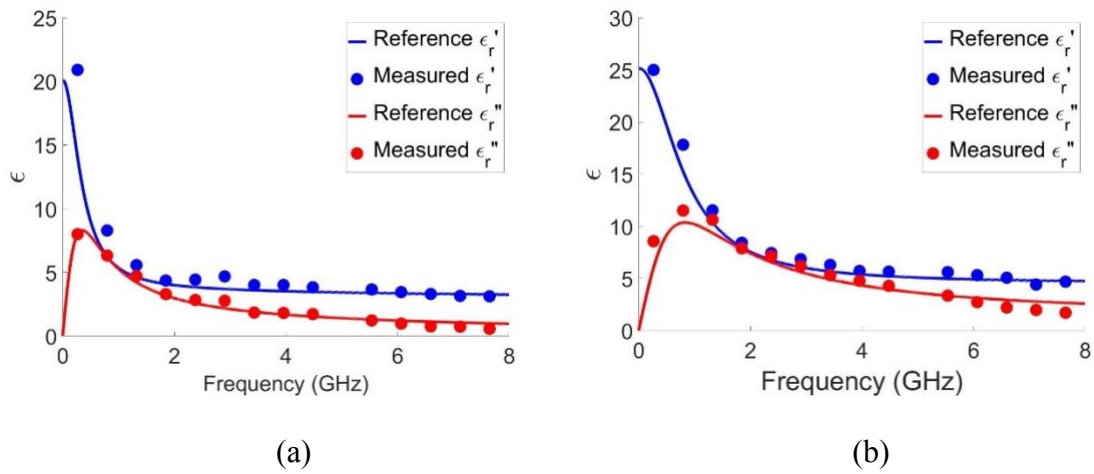
Fig. 4.6. Measured and reported [4.5] permittivities of (a) isopropyl alcohol and (b) ethanol

References

[4.1] Y. Cui, J. Sun, Y. He, Z. Wang, and P. Wang, "A simple, tunable, and highly sensitive radio-frequency sensor," *Applied Physics Letters,* vol. 103, no. 6, Aug. 2013.

[4.2] M. D. Janezic, D. F. Williams, V. Blaschke, A. Karamcheti and C.S. Chang, "Permittivity characterization of low-k thin films from transmission-line measurements," *IEEE Transactions on Microwave Theory and Techniques*, vol. 51, no. 1, pp. 132-136, Jan. 2003.

[4.3] R. Crampagne, M. Ahmadpanah, and J. L. Guiraud, "A Simple Method for Determining the Green's Function for a Large Class of MIC Lines having multilayered Dielectric Structures," *IEEE Transactions on Microwave Theory and Techniques*, vol. 26, no. 2, pp. 82-87, Feb. 1978.

[4.4] R. Garg, I. J. Bahl, and M. Bozzi, *Microstrip Lines and Slotlines*. Norwood, MA, USA: Artech House, 2013.

[4.5] A.P. Gregory and R.N. Clarke, "Tables of the complex permittivity of dielectric reference liquids at frequencies up to 5 GHz," Andrew Gregory, NPL Report MAT 23, 2012.

[4.6] R. G. Amaudov and R. B. Borisov, "S-parameters-based extraction of effective dielectric constant in transmission lines on multilayer substrates," *2011 19th Telecommunications Forum (TELFOR) Proceedings of Papers,* 2011, pp. 900-903.

[4.7] J.A. Osterberg, J. Milanes, J. Morris, and P. Wang, "Detection of *Trypanosoma brucei* by microwave cytometry," *Sensors and Actuators Reports*, vol. 4, Nov. 2022.

CHAPTER FIVE

DETECTION AND IDENTIFICATION OF *SACCHOROMYCES* YEAST SPECIES

5.1 Investigation of Yeast Microwave Specificity

A significant number of single cells need to be measured over a wide frequency range for a microwave specificity analysis to identify species or other cell characteristics. Therefore, in-flow cell measurement, instead of measuring trapped cells, is necessary. Additionally, the measurement system fluctuations should be much smaller than cellular heterogeneity within a cell species or strain, or smaller than intercellular differences for the analysis to be meaningful, as illustrated in Fig. 5.1. The measurement frequency should be tunable, since the frequencies that provide the best information for differentiation are unknown. At the same time, high sensitivity measurements are necessary, since the difference between cells within a population are expected to be small. In this chapter the results from using the multi-frequency tunable microwave flow cytometer described in Chapter IV to examine two brewing yeast species is presented.

A schematic of the microwave flow cytometer is shown in Fig. 4.1(a) and the assembly is in Fig. 4.2. The operating principle for this device was described in Chapter IV and in [5.1]. For this device setup, the sensing electrode is placed in the shorter path and an attenuator is used on the reference (*ref*) path to balance the loss between the two paths to maximize measurement signal-to-noise ratio (SNR).
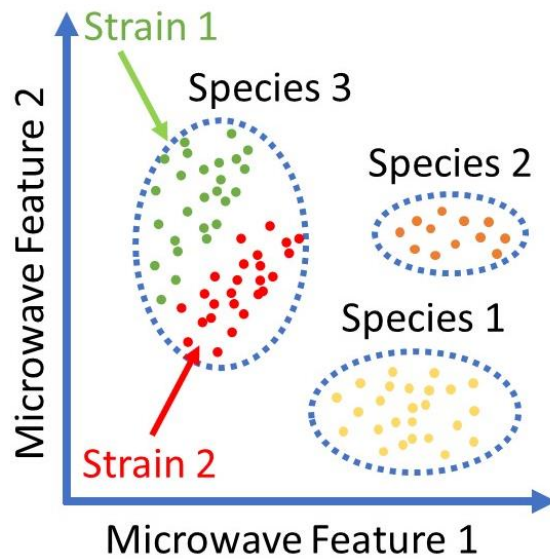
Fig. 5.1. An illustration depicting the utilization of two microwave properties to identify/distinguish different species and strains.

The measurement procedure for cell or particle measurements is as follows –

1. Calibrate the VNA using a standard thru, reflect, line (TRL) calibration kit to ensure the effects of the cables connected to the power dividers is nulled.

2. Calibrate the sensor with two liquid standards using the procedure outline in Chapter IV. This removes the effects of all components outside the sensing zone.

3. Pump the particle/cell solution into the sensor and determine operating points by measuring the broadband response. Generally this step cannot be done prior because of the varying permittivities between the calibration liquid and cell media permittivities, which shifts the interferometer operating points.

4. Measure S-parameters at a single frequency while pumping cells. A cell concentration of ~2×10^4 cell/mL pumped at 20 μL/hr will typically capture 20-

100 signals per minute. Tradeoffs between the VNA sampling rate and the pump rate can be made for faster throughput or less noise, where a higher sample rate (larger intermediate frequency) enables faster pump rate but increases system noise. For the 10 µL electrode a minimum of 15 data points is required for a single cell to ensure the peak signal is captured.

5. Adjust operating frequency and repeat Step 4. A typical measurement consisted of six single-frequency measurements with each measurement taking 2-5 minutes.

5.1.1 System evaluation with polystyrene particles

The microwave flow cytometer system was evaluated first using polystyrene particles (PSP) with various diameters (3.0 µm to 7.3 µm). The PSP measurements were used to determine the sensor accuracy, sensitivity, and precision.

Five spherical polystyrene microparticles with diameters- 3.0, 4.4, 5.5, 6.2, and 7.3 µm were suspended in DI water and pumped through the sensor at a rate of 20 µL/hr using a syringe pump to obtain signals for the six targeted frequency points shown in Fig. 4.1. These frequencies were 7.65, 5.55, 3.96, 2.38, 0.800, and 0.265 GHz. When a particle passed under the microstrip line, a shift in S_{21} was observed, which corresponded to a change in the complex permittivity due to the permittivity contrasts between the cell/particle and medium.

Fig. 5.2 shows a typical S_{21} signal and the corresponding permittivity change with DI water as the background reference. The signals are obtained with the same particle that passes through the sensing electrode multiple times. The particle was manually

controlled to pass back and forth across the sensing electrode to test the repeatability of the measurement. The particle position was controlled by first injecting the particle solution into the sensor and waiting several minutes until the particles stopped moving. The particle's lateral position can then be precisely controlled by raising and lowing the tubes connected to the inlet. The measurement time step is approximately 10 ms. The average shifts of ε' and ε'' were 0.760±0.013 and 0.145±0.006, respectively. The results show that microwave flow cytometer is sensitive, and the measurements are repeatable.
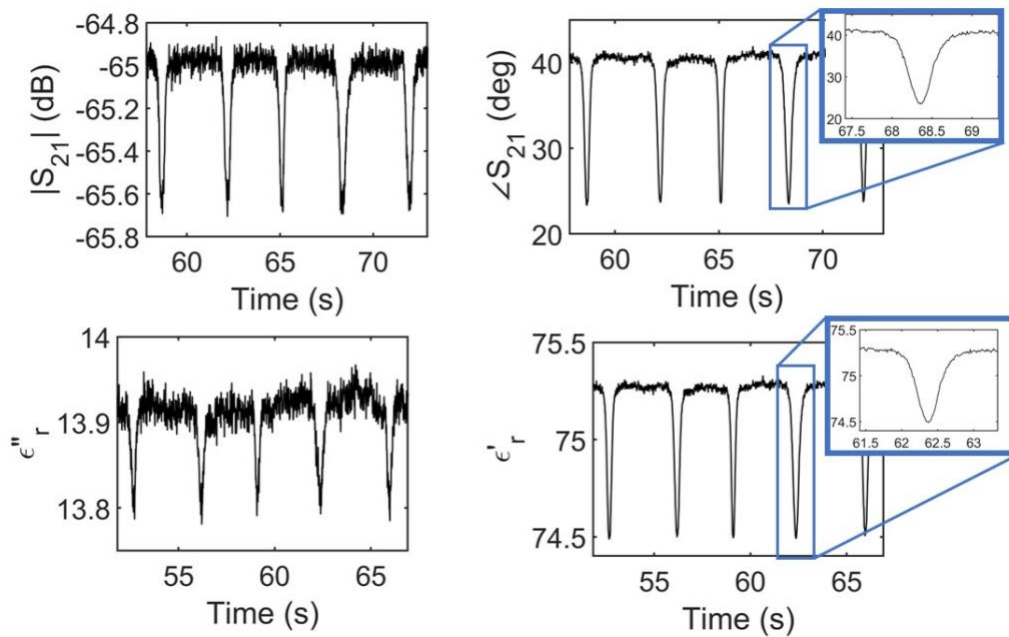
Fig. 5.2. Multiple measurements of a single 5.5 μm particle at 3.96 GHz. The average shifts of ε' and ε'' were 0.760±0.013 and 0.145±0.006, respectively. The differences between measurements can be attributed to noise having a small effect on the peak shift value.

Fig. 5.3 shows the measured results of 150 5.5 μm PSP particles measured one at a time. The average shifts for all the particles are 0.660±0.044 (ε') and 0.112±0.022 (ε''). The coefficients of variation of $\Delta\varepsilon'$ and $\Delta\varepsilon''$ are 5.40% and 17.53%, respectively. Compared to 13.64% particle volume variation, the system has good measurement accuracy.
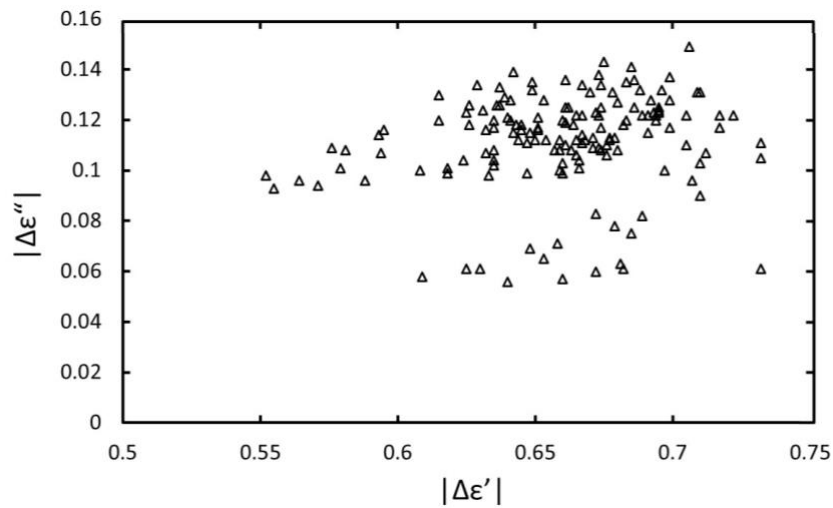
Fig. 5.3. Scatter plot of permittivity shifts for 150 5.5 μm PSP particles measured at 3.96 GHz.

Fig. 5.4(a) shows measured ΔS_{21} of PSPs with different diameters. The minimum detectable PSP particle and permittivity change, which yields an SNR of 3:1, is frequency dependent as shown in Fig. 5.4(b). The sensitivity decreases at lower frequencies due to decreasing electrical length. At higher frequencies, the sensitivity flattens out because of increased sensitivity to mechanical noise in the cables. The predicted smallest measurable PSP particle is 1.7 μm diameter, assuming a linear relationship between volume and signal size, which would occur at 2.38 GHz.
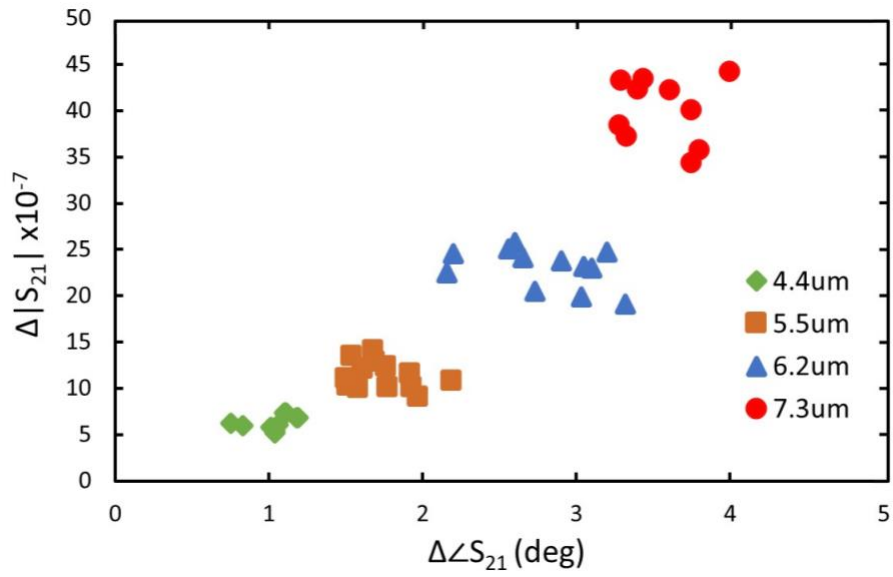
(a)
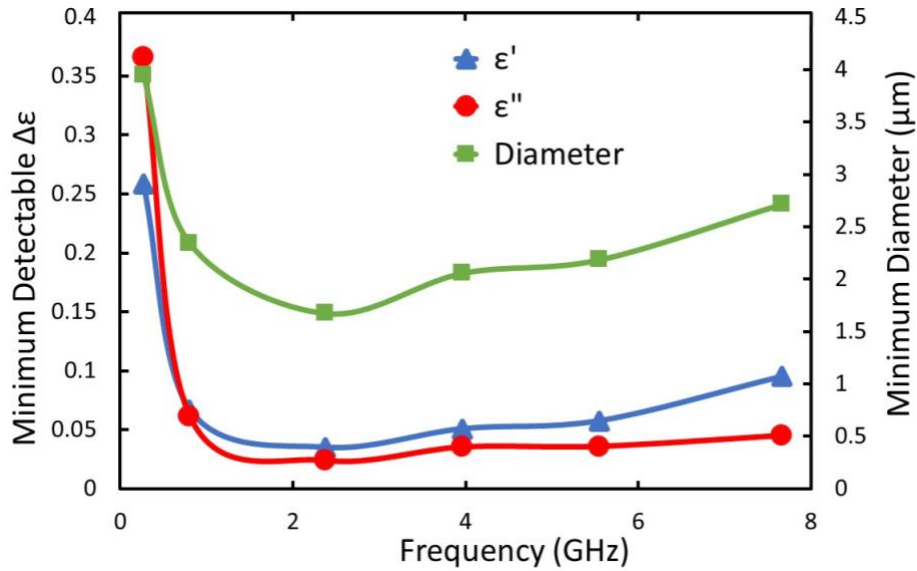
(b)

Fig. 5.4. (a) Scatter plot of the observed S_{21} shift for various sizes of microparticles at

1.81 GHz. Each point represents the peak induced shift, plotted as magnitude vs. phase.

(b) Minimum detectable shift in permittivity and minimum detectable PSP diameter for a

3:1 SNR.

5.1.2 Yeast cell measurement

The second evaluation of the microwave flow cytometer system probed viable and non-viable *S. cerevisiae* and *S. pastorianus*, two popular species of yeast used in the production of beer, for signal characteristics. The two species are nearly identical in size and shape, which makes visual identification difficult [5.9, 5.12]. Both are elliptical in shape and vary from 7 to 10 μm long and 4 to 7 μm wide [5.10, 5.11]. The similar morphologies are a result of *S. pastorianus* being a hybrid *S. cerevisiae* and another species, *S. eubayanus*, which also gives *S. pastorianus* a double size genome [5.9, 5.16, 5.17]. As such, biochemical techniques such as mass spectrometry and polymerase chain reaction (PCR) must be employed to identify closely related species [5.13-5.15]. These techniques are expensive and time consuming. The ability to rapidly distinguish between similar species such as these could provide a valuable new methodology for microbiologists.

When yeast from either species were killed by heat shock there was no noticeable change in morphology, provided the temperature was not so high to completely breakdown the cell membrane. High temperature and subsequent cell death is known to increase membrane permeability [5.16]. Consequently, there were no visual differences between the two yeast species and the two states for each condition (live and dead). Thus, the differences in microwave properties were due to the inherent differences between the cells. *S. cerevisiae* and *S. pastorianus* cells, shown in-flow in the sensor in Fig. 5.5, were grown in Yeast Extract-Peptone-Dextrose (YPD) medium until a concentration greater than or equal to 10^6 cells/mL was reached, typically around 24 hours.
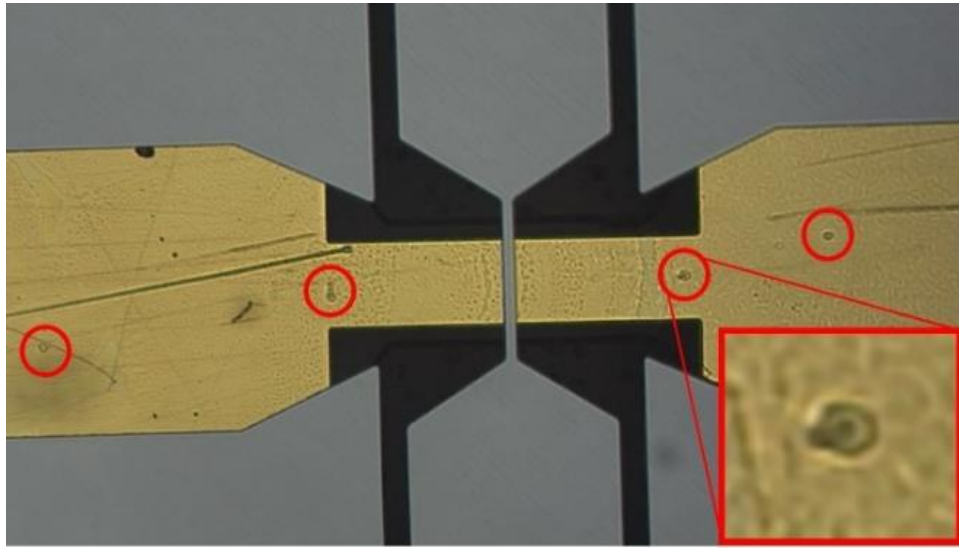
(a)
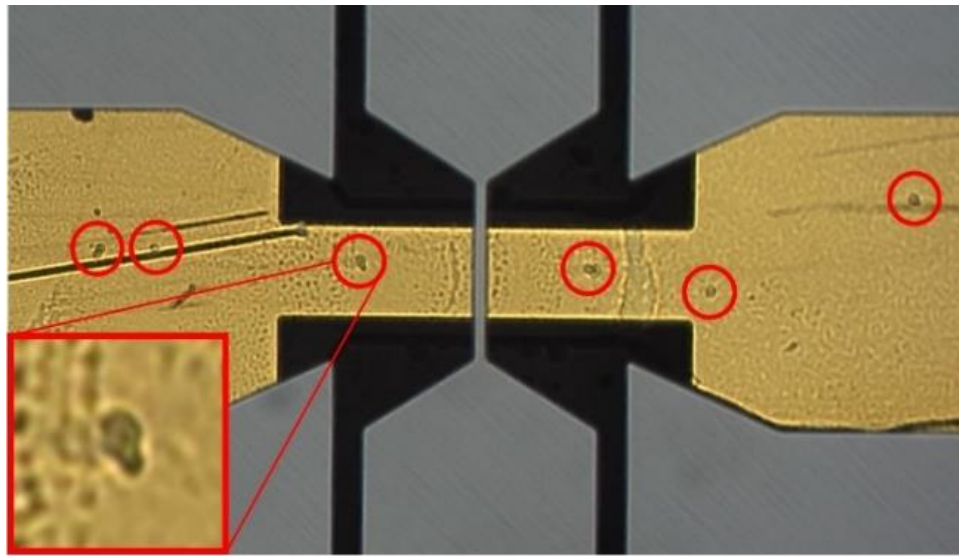
(b)

Fig. 5.5. Microscope images taken of live (a) *S. cerevisiae* and (b) *S. pastorianus* cells in-flow. The two strains, whether alive or dead, are visually indistinguishable.

The cells were diluted 40:1 DI water:cell medium immediately before taking measurements. Since measurements are taken for individual cells, the consistency of the cell concentrations between measurements is not of concern, but rather the consistency of the medium as that will affect the baseline permittivity. Dead cell samples are obtained by killing yeast in 90°C water for one minute. The effectiveness of the methods used for cell growth and killing the cells were confirmed by performing cell viability counts using Trypan blue and a hemocytometer, shown in Fig. 5.6. Trypan blue selectively stains for dead cells, making the dead cells appear darker in color. Live cells with intact membranes are not stained, making them appear lighter in color. We found *S. cerevisiae* live samples are at least 97% viable and dead samples contain less than 1% viable cells and *S. pastorianus* live samples are over 99% viable and dead samples have less than 2% viable cells.

All samples were prepared to be as uniform as possible to keep the baseline permittivity constant throughout measurements. However, due to the complex biological processes taking place during cell growth, there will always be slight differences in the media, shown in Fig. 5.7. We found the solution media permittivity had a maximum standard deviation between measurement samples of 0.9 for ε' and 0.3 for ε'', occurring at 0.265 GHz and 0.8 GHz, respectively, and the percent difference between media permittivities was less than 3% for all frequencies except for ε'' at the same two frequencies, although the larger differences are exaggerated due to the small values of ε''. The effects of these differences are minimal compared to the intrinsic differences between cells within a given population.
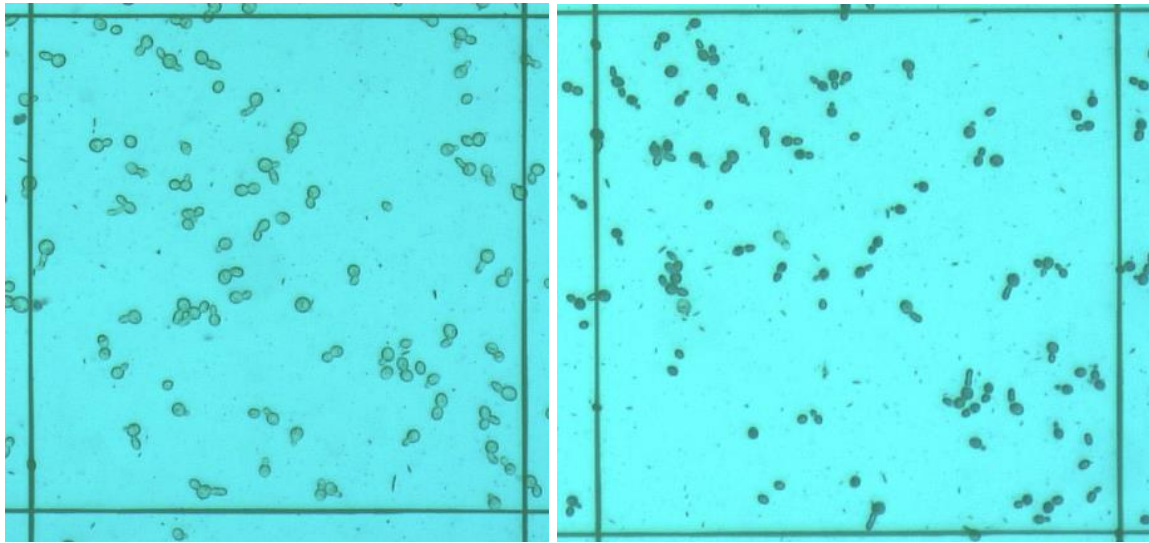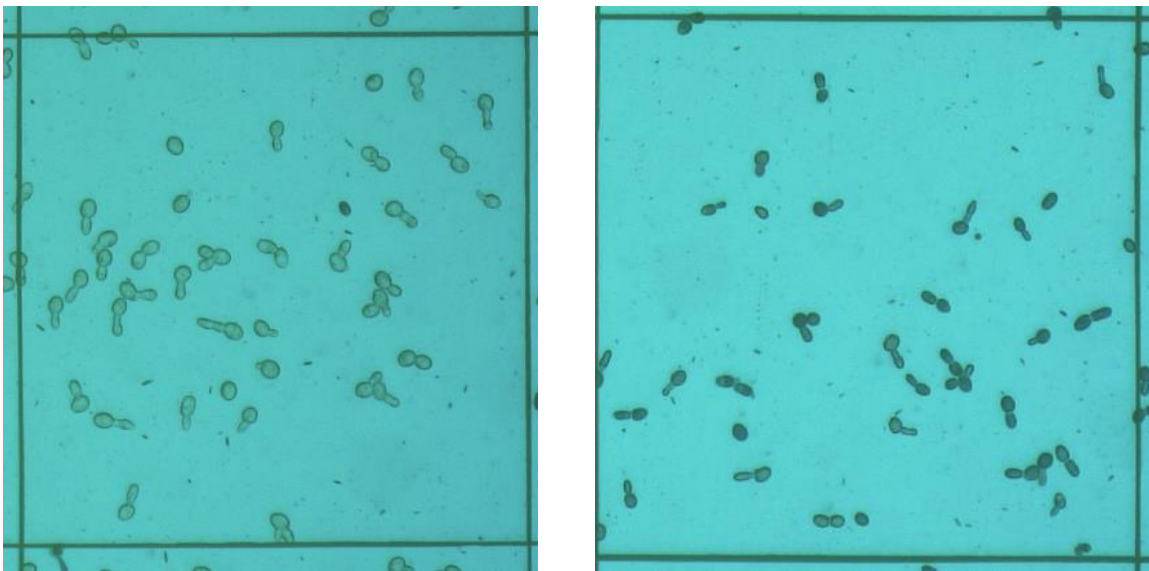
Fig. 5.6. Stained (a) live and (b) dead *S. cerevisiae* cells and (c) live and (d) dead *S. pastorianus* cells.
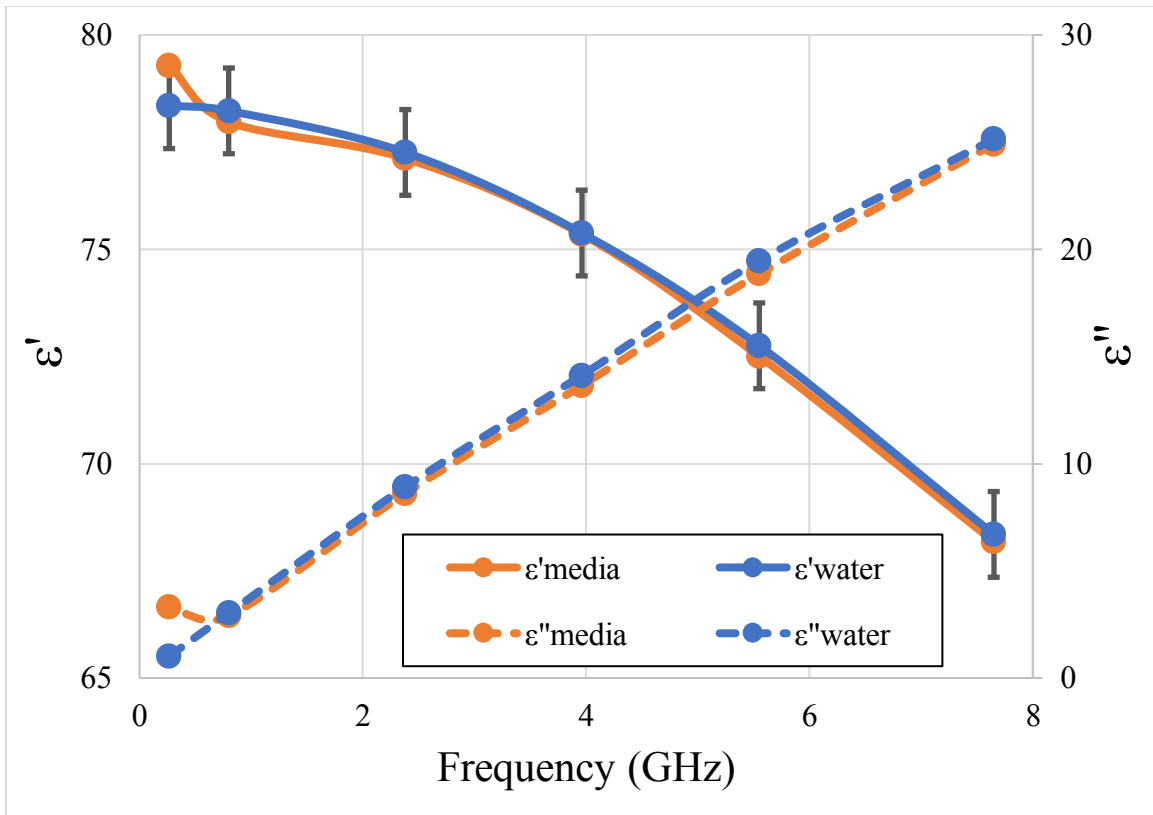
Fig. 5.7. Comparison of the complex permittivity of the media solution with water. The media solution values are the average values of all samples at each frequency.

Multiple time domain measurements were taken of four yeast samples, including two yeast species, *S. cerevisiae* and *S. pastorianus,* at two physiological states, live and dead. Measurements were taken one frequency at a time under the assumption that the solutions have a uniform distribution (i.e. uniform baseline). Fig. 5.8 shows typical measurement results of *S. pastorianus* cells at 2.38 GHz. Each signal represents a cell passing under the ML, with the peak change in ε' and ε'' occurring when the cell is under the center of the electrode.
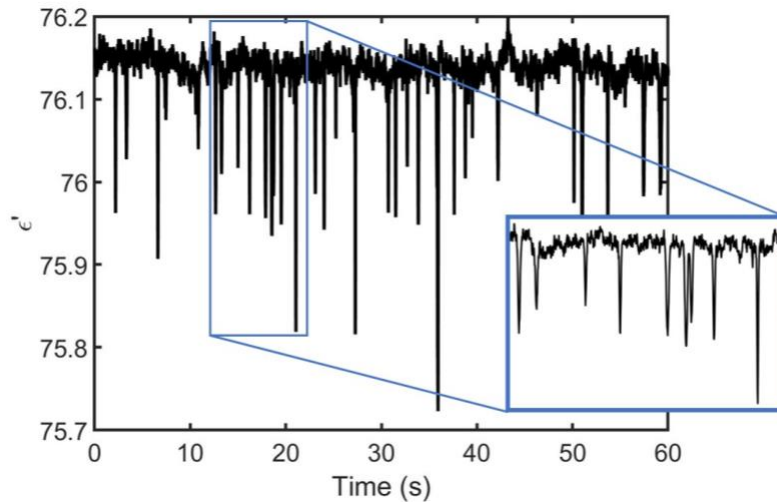
(a)
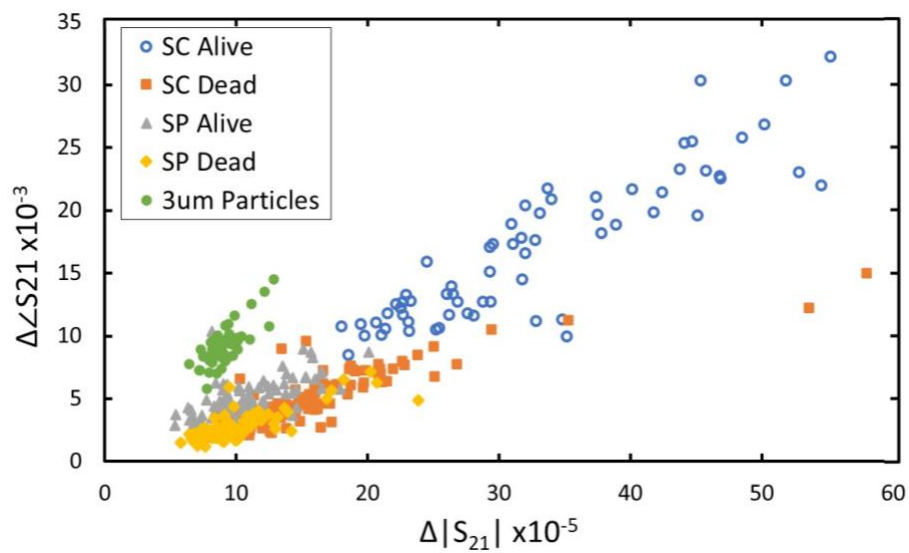
(b)

Fig. 5.8. (a) Typical time domain measurement of *S. pastorianus* yeast cells, taken at 2.38 GHz. Each signal is due to a single cell passing through the sensor. (b) Scatter plot of the change in S_{21} magnitude versus phase at 2.38 GHz. The S-parameter data is used to calculate the complex permittivity, then the peak change in ε' and ε'' is used to obtain the cell population's response.

Scatter plots for the six frequencies are shown in Fig. 5.9. Each point in the plots represents the absolute value of the difference between the average baseline value and the peak change in both ε' and ε'' for a single cell.

The results show that yeast signals have a significant distribution, which is quantified in Tables 5.1 and 5.2. The distribution comes from various potential sources discussed above. Additionally, multiple cells passing through the sensor simultaneously or cells passing under the electrode in an area where there is no ground plane may have attributed in part to the variations, but from microscope observations during measurement we estimate this occurring in less than 3% of measurements. Given the dilutions and the small areas without a ground plane relative to the areas that do contain a ground, the variations are mostly due to intrinsic differences between cells within the populations. Overall, viable *S. cerevisiae* has the largest distribution at the three frequencies, possibly due to larger microwave permittivity variations during the cell's life cycle compared to *S. pastorianus* cells. Further work is needed to understand the biological sources. All yeast signals and signal distributions are frequency dependent. At higher frequencies, yeast permittivity values ($\Delta\varepsilon$) are lower, but the distributions remain constant. Different yeast species have different signals and permittivity values, which are also altered to different degrees by cell death. Though signal overlaps exist, there are significant separations at each frequency point. The differences indicate potential microwave specificity.
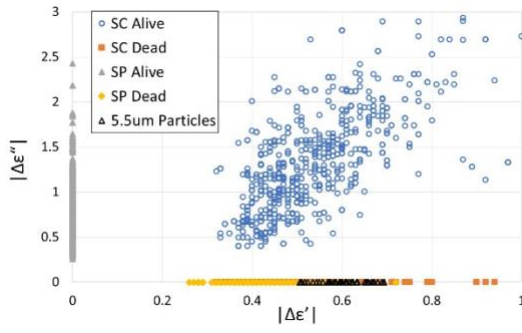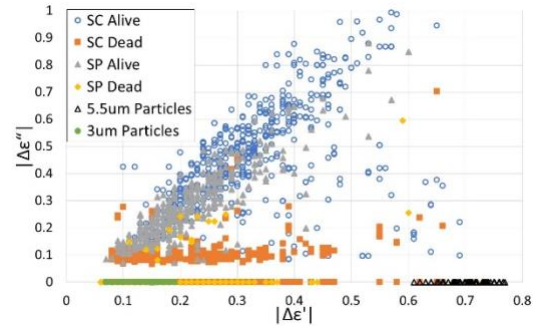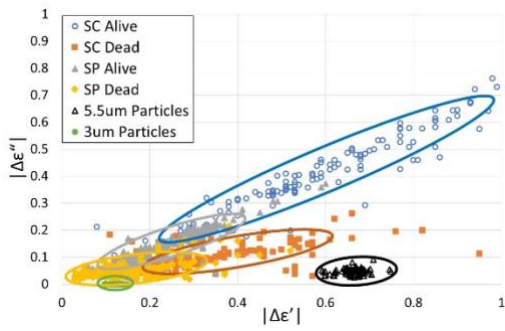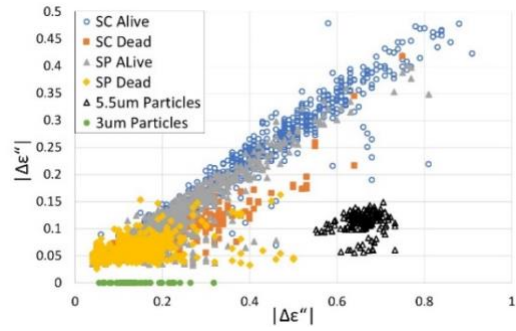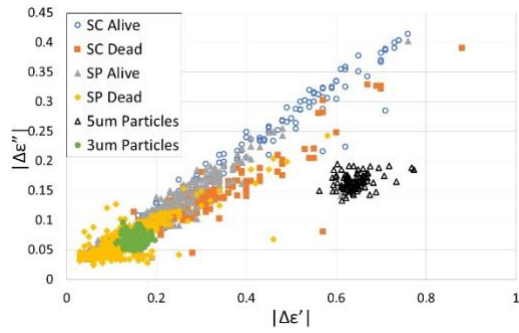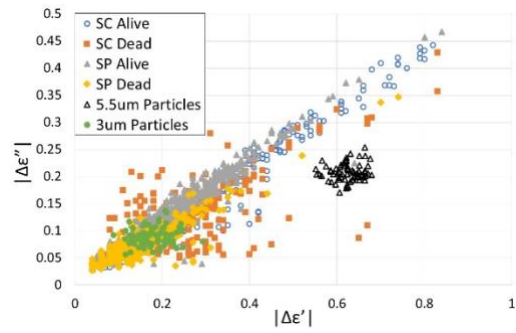
Fig. 5.9. Scatter plots of permittivity of known samples at (a) 265 MHz, (b) 800 MHz, (c) 2.38 GHz, (d) 3.96 GHz, (e) 5.55 GHz, and (f) 7.65 GHz. Each data point represents the change in permittivity for a single cell or particle, with the x-axis being the real part and the y-axis the imaginary part.

Fig. 5.10 shows the measured ε^*_{MUT} vs. frequency with the water permittivity plotted for comparison. The extracted ε^*_{MUT} follow water permittivity trend, as is shown in bulk cell measurements [5.2]. Figs 5.11 shows the trend of average yeast permittivity vs. frequency.

At 265 MHz we see that the average value of $\Delta\varepsilon'$ for the two species of dead cells are smaller than the live counterparts. This is likely due to a decrease in membrane capacitance caused by cell death, since the membrane capacitance of yeast cells remains constant while the cells are viable and drops to zero at cell death, and a smaller membrane capacitance would be observed as a decrease in the real part of the cell's permittivity [5.4]. The difference observed between the two live species at the lowest frequency can also be described by differences in the cell's membrane capacitances, since the permittivity of yeast membranes has been shown to be correlated to flocculation abilities of yeast cell species, with weaker flocculating cells having a higher permittivity [5.5]. In this work the authors observed that *S. cerevisiae* cells, which have a weaker flocculation ability than *S. pastorianus* cells, have a higher permittivity than *S. pastorianus* cells when measured in solution from 100 Hz to 100 kHz. The authors suggested the result was due to differences in cell surface charge between the two cell types, where a decrease in surface charge would decrease electrostatic repulsion between cells, and hence increase flocculation. However, a relationship between surface charge in yeast at the start of flocculation has not been found [5.18]. It has also been suggested that cell-surface hydrophobicity is responsible for flocculation in brewing yeast [5.19]. This is supported by measurements over the frequency range 40 Hz to 110 MHz showing that the

dielectric properties of the plasma membranes of live *S. cerevisiae* are strongly influenced by the properties of the hydrophobic layer of the cell membrane [5.20]. Regardless of the underlying mechanisms, our results are consistent with those reported in [5.5]. Although their measurements were performed at lower frequencies, the effects of membrane capacitance on permittivity have been observed at frequencies as high as 100 MHz and is most likely the cause of our observations [5.8].

TABLE 5.1
COEFFICIENTS OF VARIATION OF $\Delta\varepsilon'$

Frequency (GHz)	SC Live	SC Dead	SP Live	SP Dead	5.5 μm
7.65	58.2%	61.1%	41.2%	51.4%	5.06%
5.55	42.1%	47.4%	41.7%	49.3%	3.78%
3.96	51.9%	57.3%	45.3%	51.0%	5.40%
2.38	43.2%	50.1%	38.9%	52.50%	4.78%
0.80	57.8%	50.6%	38.9%	41.6%	5.50%
0.265	57.0%	19.4%	ND	18.7%	9.0%

SC represents *S. cerevisiae* and SP represent *S. pastorianus*. ND indicates permittivity values that were not obtainable.

TABLE 5.2
COEFFICIENTS OF VARIATION OF $\Delta\varepsilon''$

Frequency (GHz)	SC Live	SC Dead	SP Live	SP Dead	5.5 μm
7.65	58.8%	52.1%	39.9%	44.8%	7.7%
5.55	39.6%	42.3%	35.8%	39.8%	23.2%
3.96	50.9%	58.8%	45.7%	33.9%	17.5%
2.38	43.6%	43.9%	43.9%	52.9%	24.4%
0.80	51.1%	119%	46.3%	ND	ND
0.265	44.5%	ND	40.7%	ND	ND

SC represents *S. cerevisiae* and SP represent *S. pastorianus*. ND indicates permittivity values that were not obtainable.

At frequencies 800 MHz and above, where microwave signals more readily probe structures within the cell membrane, it is possible that the difference observed between the two species is a result of *S. pastorianus* having a larger relative genome size (1.46) than *S. cerevisiae* (1.00) [5.9]. Regardless, due to the probing nature of high frequency signals several factors will influence measurements (nucleoplasm, cytoplasm, nucleus size, nuclear envelope thickness) and thus further investigation is needed to verify this is the only cause.

The differences in $\Delta\varepsilon''$ observed between live and dead cells are likely due to increased membrane permeability caused by heat shock, meaning molecules in the external media can more readily diffuse across the cell membrane into the cell (and simultaneously, leakage of cytoplasmic ions) making the conductivity, and hence ε'', inside the cell more closely match that of the media [5.7]. At the lowest frequency (265 MHz), this is supported by observations in [5.6], where the authors measured the dielectric properties of live and dead yeast cells in suspension from 60 kHz to 600 kHz and observed lower dielectric loss ε'' of dead yeast suspensions compared to live cell suspensions. Despite these measurements being at lower frequencies than ours, the trend should extend to higher frequencies since at higher frequencies, penetration of the microwaves into the cell increases and cell membrane effects have little impact on the measured complex permittivity. This means intracellular differences between cells become more apparent. At frequencies of 800 MHz and above, where internal cell properties are more readily observed, our results are consistent with those in **[20],** where the authors observed by way of electrorotation a significant decrease in cytoplasmic
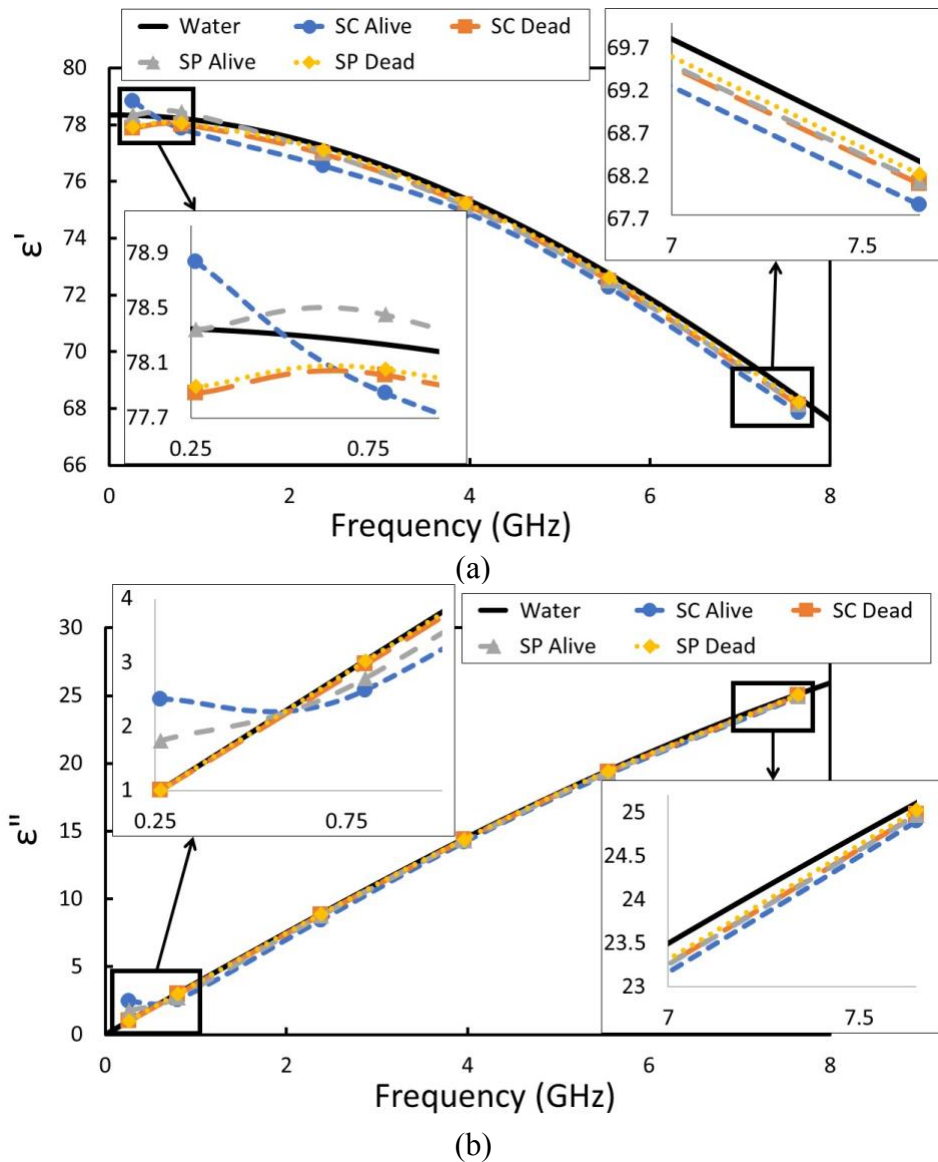
Fig. 5.10. Average shift of (a) ε' and (b) ε'' for the four cell classes versus frequency, with DI water as the baseline reference. The background reference was changed to water to help illustrate the differences observed between cell types. The media changes slightly between measurements based on chemical makeup and temperature. Efforts were made to keep the media as consistent as possible across measurements, minimizing the resulting error.
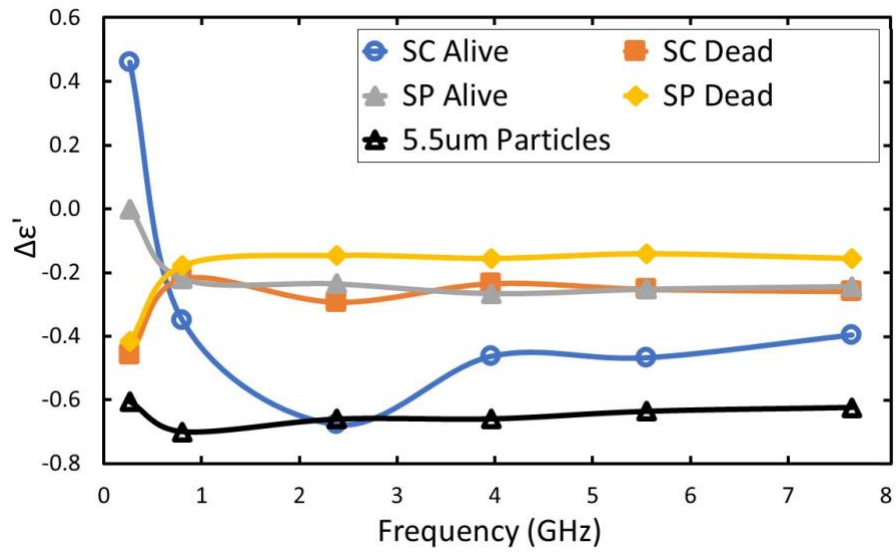
(c)
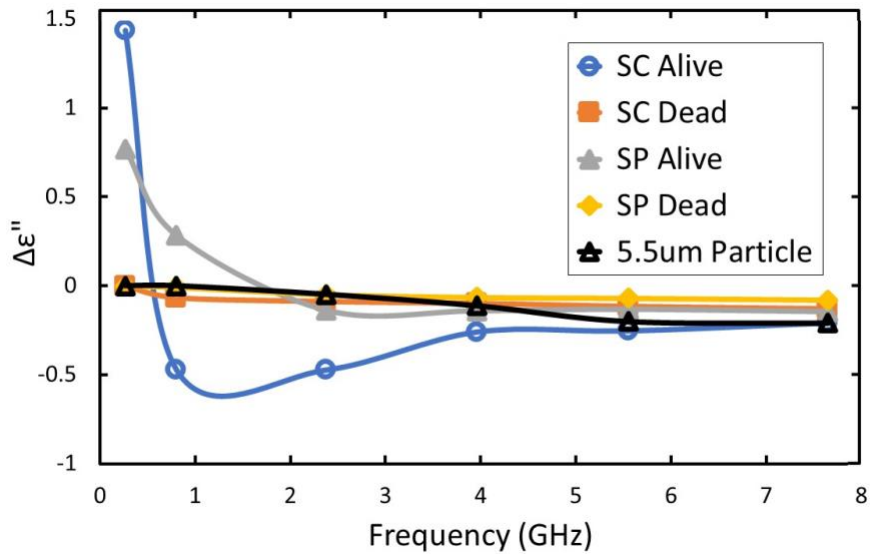
(d)

Fig. 5.11. Average shift in (c) ε' and (d) ε'' vs. frequency for each of the five mixture classes. The relative consistency in the 5.5 μm particle signals and the consistently large variability from cells across frequencies indicates that any observed frequency dependence is due to intrinsic cell properties.

conductivity in *S. cerevisiae,* from 5500±500 μS/cm to 100-800 μS/cm, when the cells were killed by heat shock. This decrease in conductivity would result in a smaller $\Delta\varepsilon''$ for dead cells compared to live cells, which is what we observed in our measurements.

This shift to internal cell properties being more readily observed at higher frequencies is apparent in the average $\Delta\varepsilon'$ at 800 MHz and above, where we see that live cells have a larger (more negative) shift than their dead counterparts. This is due to the protoplasm of the live yeast having a smaller permittivity than that of the media (which is mostly water) [5.3]. Again, due to the increased membrane permeability the internal permittivity of the dead cells more closely resembles that of the media, while the permittivity of the live cell's protoplasm is much smaller, resulting in a larger shift for live cells. Additionally, the increase in $\Delta\varepsilon'$ above 265 MHz for dead cells can be explained by the membrane capacitance no longer having an observable effect.

5.2 Machine Learning for Mixture Prediction

To better understand if microwave measurements can be exploited to discriminate yeast species and the viability of the yeast, a prediction model was developed using the measurement data described above. Quadratic discriminant analysis (QDA) was used for frequencies above 2.38 GHz and above since the data obtained appears to have a normal distribution. *K*-nearest neighbor (KNN) and linear discriminant analysis (LDA) was used for the lowest two frequencies due to having some data on only the x- or y-axis (Fig. 5.9(a) and (b)).

QDA uses a quadratic decision surface to classify measurements, as show in Fig.

5.12. It is a generative classifier that assumes each measurement class has a Gaussian distribution. The probability density function (PDF) $N(\mu, \Sigma)$ in D dimensions is defined as

$$N(x|\mu, \Sigma) = \frac{1}{\sqrt{(2\pi)^D det\Sigma}} \exp\left(-\frac{1}{2}(x-\mu)^T\Sigma^{-1}(x-\mu)\right) \qquad (5.1)$$

Where μ is the mean vector and Σ is the covariance matrix. Generative classifiers model the joint probability distribution of the inputs and their targets, i.e. the permittivity changes and the cell classes, respectively, to find the maximum likelihood solutions for the class-specific priors (proportion of data points that belong to a class), means, and covariance matrices of the PDF in Eq. 5.1.

KNN, on the other hand, is a non-parametric, or discriminative, classifier that generates classification surfaces using the k closest training examples from the data set (training set). Euclidean distance was used as the distance metric, which for points p and q located at (p_1, p_2) and (q_1, q_2), respectively, in Cartesian coordinates is

$$d(p, q) = \sqrt{(q_1 - p_1)^2 + (q_2 - p_2)^2} \qquad (5.2)$$

When an unknown object is input, the object is classified by a plurality vote of its neighbors based on the most common class of its k nearest neighbors. A k of 5 was used for all classifications models discussed in this chapter and in Chapter VI. Examples of decision surfaces from the two models is shown in Fig. 5.12.

For both QDA and KNN models the training data consists of five classes- the four yeast classes (*S. cerevisiae* and *S. pastorianus*, live and dead) and 5.5 μm particles, which could represent debris in an application such as cell monitoring during fermentation,
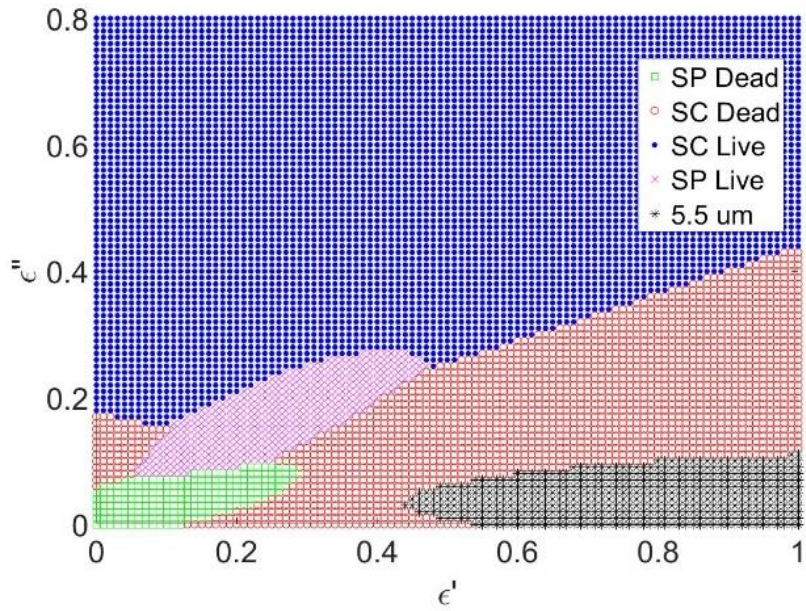
(a)
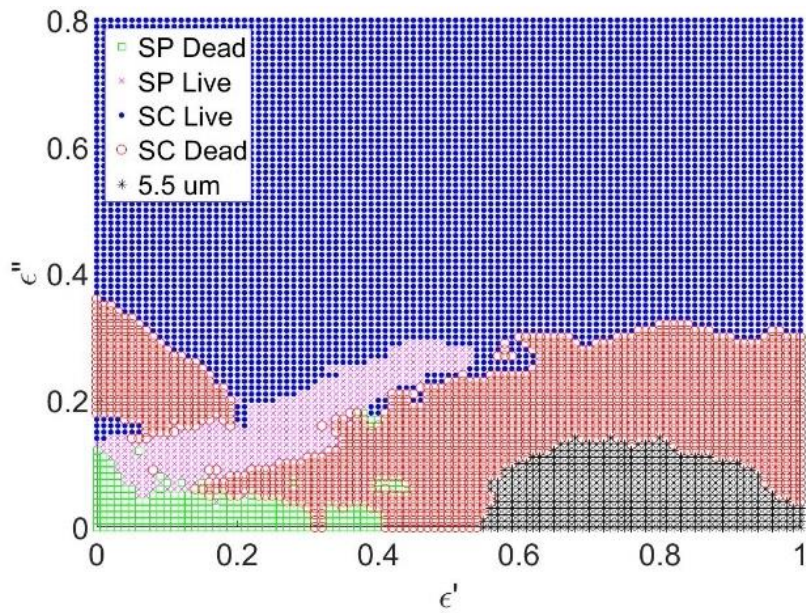
(b)

Fig. 5.12 classification surfaces from (a) quadratic discriminant analysis and (b) *k*-nearest

neighbors for 2.38 GHz, corresponding to the scatter plot in Fig. 5.9(c).

81

which would contain a significant amount of grain particulates from the mashing process that could potentially be misidentified as cells. Prediction models were developed and compared for individual frequencies. The performance of the prediction models can be measured using cross-validation, wherein the data is split into two groups – the training set and the test set. The prediction model is trained with the training set and the error rate is estimated with the test set. For k-fold cross-validation the data set first split into k groups, one group is taken as a test set and the remaining groups are used as the training set to generate a model. The model is then discarded, and the process is repeated until all k groups have been the held out as the test set. The k-fold cross validation error is given as the average error rate of all models, given in Table 5.3.

TABLE 5.3
CROSS-VALIDATION ERRORS

Frequency (GHz)	QDA	KNN
7.65	33.2%	37.4%
5.55	32.2%	34.9%
3.96	32.1%	35.8%
2.38	27.1%	19.1%
0.80	34.4*%	29.1%
0.265	15.0*%	10.7%

* Linear discriminant analysis (LDA) was used to generate prediction models since QDA was not possible.

The sample data sizes used in the prediction models and the 10-fold cross validation data set sizes are given in Table 5.4 and Table 5.5, respectively. The prediction algorithm, starting from raw S-parameter data, is shown in Fig. 5.14.

The performance of the machine learning algorithms can be visualized using confusion matrices, as shown in Fig. 5.13, which summarizes the results of a classification problem. Each row of the confusion matrix represents the true class and

TABLE 5.4
MACHINE LEARNING SAMPLE SET SIZES

Frequency (GHz)	SC Live	SC Dead	SP Live	SP Dead	5.5 μm	Total
7.65	166	260	544	315	66	1351
5.55	109	243	214	328	64	958
3.96	550	184	501	348	150	1733
2.38	135	213	192	234	68	842
0.80	458	295	324	351	65	1493
0.265	558	322	563	80	41	1564

TABLE 5.5
10-FOLD CROSS VALIDATION SET SIZES

Frequency (GHz)	Training Set Size	Test Set Size	Classifier
7.65	1216	135	QDA
5.55	862	96	QDA
3.96	1560	173	QDA
2.38	758	84	KNN
0.80	1344	149	KNN
0.265	1408	156	KNN

columns represent the predicted classes from the model; hence the main diagonal is the number of correctly identified classes and all other values are incorrect classifications. For example, in Fig. 5.13(b) the model predicted that 73 measurements were 5.5 μm particles, of which 68 were correct, 4 were incorrectly classified as SC Dead, and 1 was incorrectly classified as SP Live. The empty values mean none of the predicted 5.5 μm particles were incorrectly identified as SC Live or SP Dead. Summing all elements in the matrix gives the total sample set of the model. In a normalized confusion matrix, each row is balanced and represented as having 1.0 samples. In Fig. 5.13(b) row one indicates that 98.6% of the predicted 5.5 μm particles were correct, or 68 of the 69 predicted were correct. Confusion matrices for the remaining frequencies are given in Appendix A1.
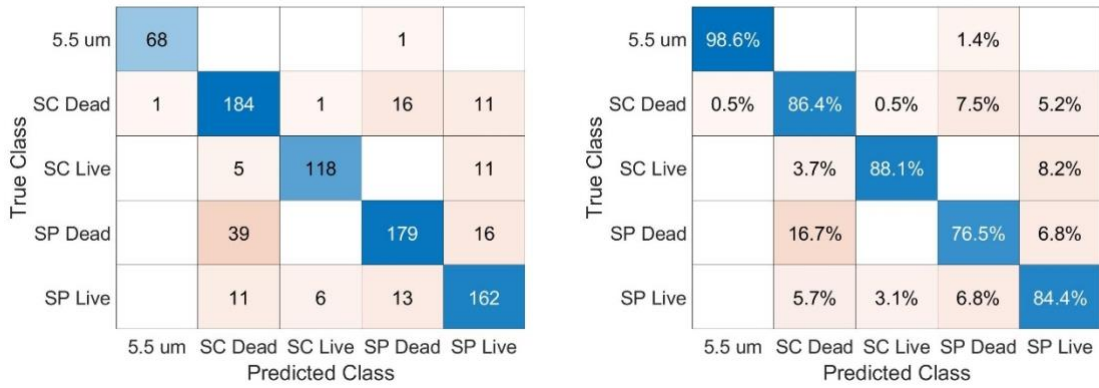
(a)
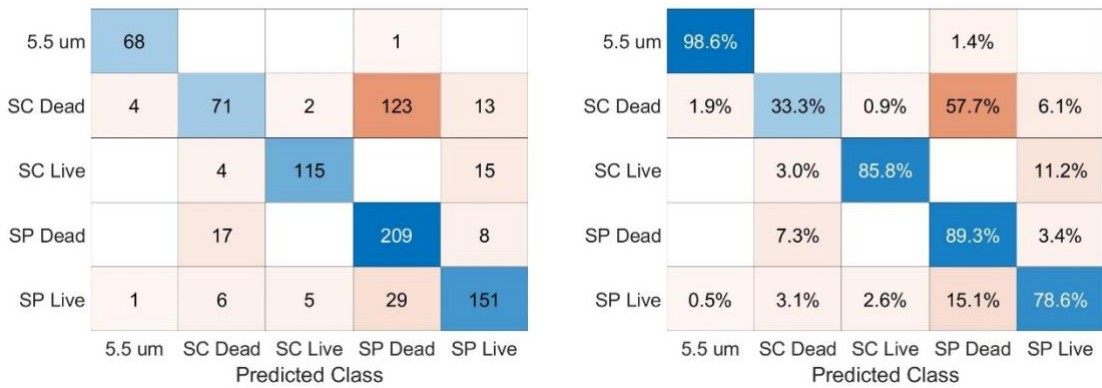
(b)

Fig. 5.13 Confusion matrices from (a) KNN and (b) QDA classification algorithms at 2.38 GHz.

We found that 2.38 GHz and 265 MHz show the lowest uncertainty if using single frequency measurements, with cross validation errors of 19% and 10%, respectively, which supports the notion that certain frequencies are more sensitive to the minute
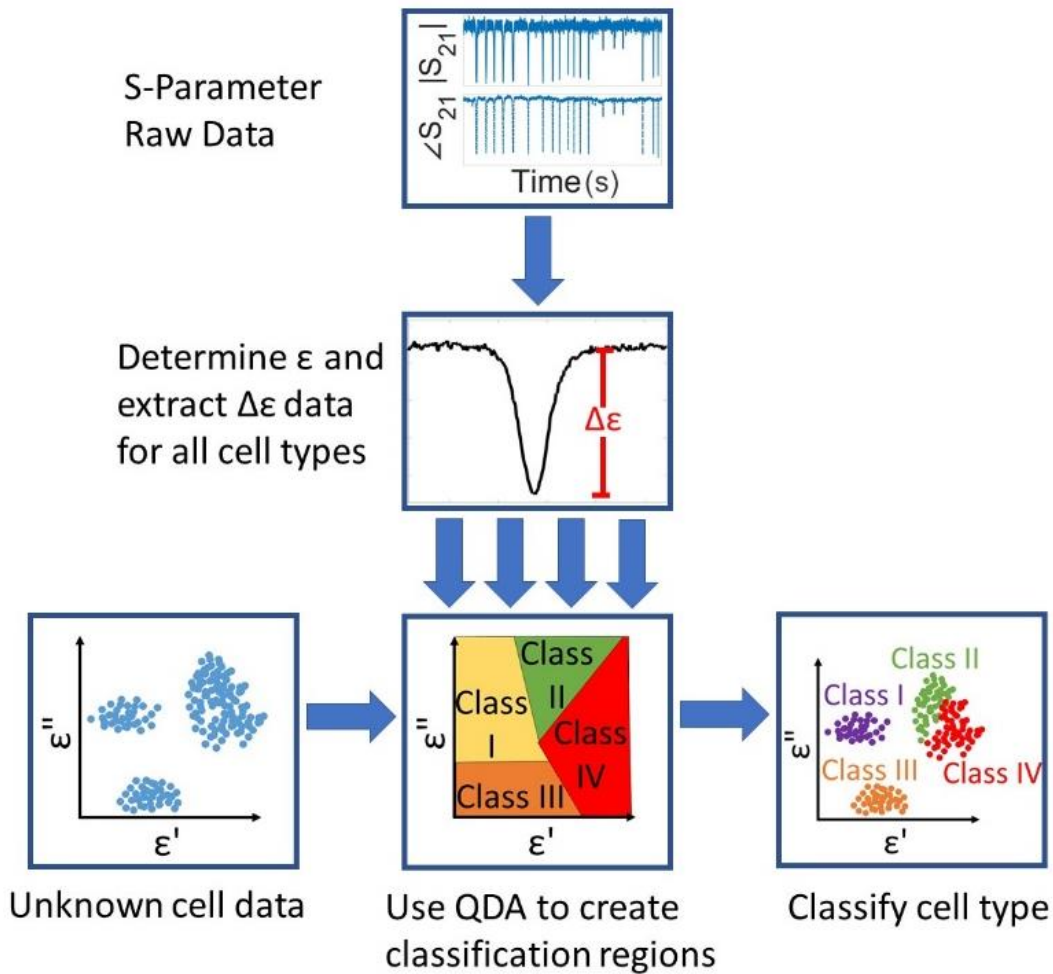
Fig. 5.14. The cell identification algorithm development. A quadratic classifier is used on known cell measurement data to create a decision surface. The regions on the surface can be used to classify unknown cell types in a mixture.

differences between live and dead cells from the same species. It also suggests that broadband measurements of the same yeast cell should enhance the differentiation power.

To further test the sensing and prediction ability of the microwave flow cytometer, the permittivity extraction algorithms, and the models in Chapter IV, a

mixture of the five classes is measured at each frequency point. The mixture contained

equal parts of the four yeast classes (22.2% each) and half as many 5.5 μm particles

(11.1%). Prior to mixing, cell densities were measured using a spectrophotometer. Fig.

5.15 shows typical time domain measurement signals at 2.38 GHz.

TABLE 5.6
PREDICTED CLASSIFICATIONS OF CELL MIXTURE

Frequency (GHz)	SC Live	SC Dead	SP Live	SP Dead	5.5 μm
7.65	25.6%	17.9%	23.9%	21.4%	11.1%
5.55	32.7%	18.3%	17.3%	15.4%	16.3%
3.96	9.4%	17.2%	32.8%	14.1%	26.6%
2.38	20.0%	21.8%	26.1%	22.4%	9.7%
0.80	44.1%	5.6%	6.3%	28.0%	16.1%
0.265	9.2%	35.9%	52.2%	0.0%	2.7%

At least 100 data points were collected at each frequency, the prediction results at

each frequency are shown in Table 5.6. While the cross-validation suggested that 265

MHz would be the most accurate, the trained model is unable to distinguish between the

two dead cell types and particles, all of which lie on the x-axis (Fig. 5.9(a)). Fig. 5.16

shows the predicted classification of the mixture at 2.38 GHz, which agree reasonably

well with expectations. This further supports the statement that the slight differences in

the media for the individual cell measurements discussed previously produce minimal

error, since that data was used for training the model.

The accuracy of predictions could be increased further by using larger training

data sets or by using multi-frequency measurements. In the case of multiple frequencies,

decision trees could be used where differences are seen in only one or two classes at a

frequency, such as *S. cerevisiae* and *S. pastorianus* live cells at 265 MHz, which can

clearly be differentiated but the other classes have significant overlap.

86

(a)   (b)
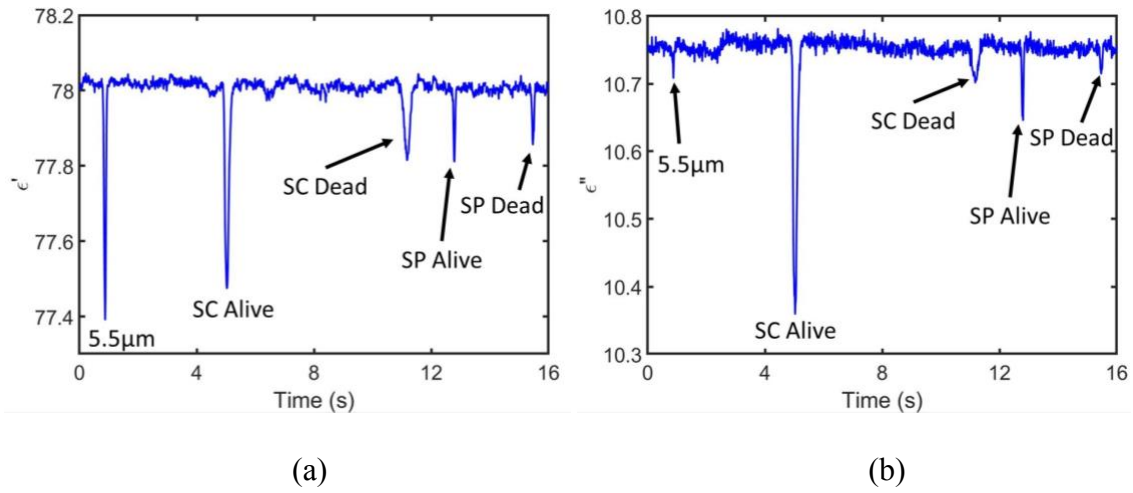
Fig. 5.15. Time domain measurements of (a) ε' and (b) ε'' at 2.38 GHz showing typical

signals for each of the five classes measured. Signal snippets were taken from known

sample measurements and spliced together to demonstrate their differences.
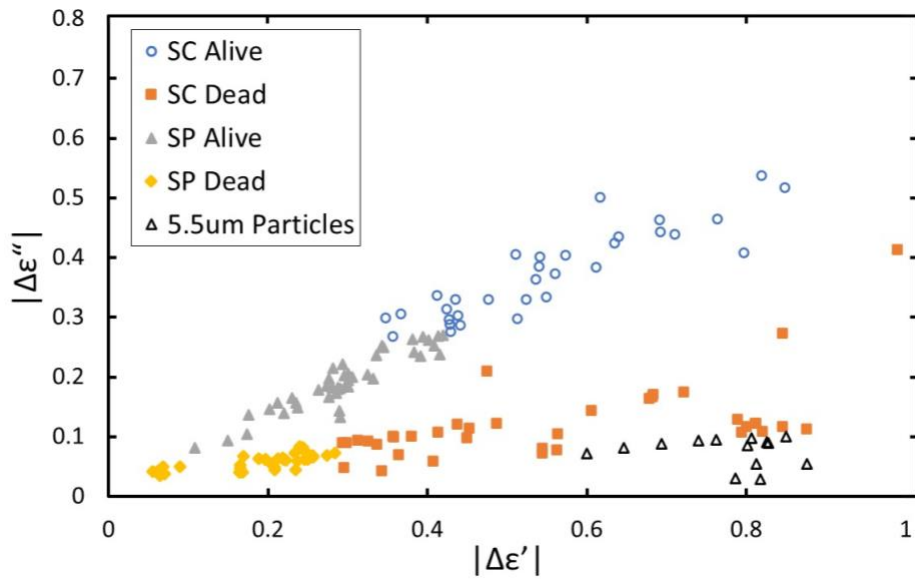
Fig. 5.16. Predicted classifications of mixture at 2.38 GHz. Predictions were made using

KNN with the training data shown in Fig. 12(c).

As shown in Fig. 5.9, significant distribution at every frequency is observed for each yeast class, with live *S. cerevisiae* having the largest. A major contributor to the variations comes from cells being in different stages of growth within the samples, since it is known that budding yeast and single yeast cells have different microwave dielectric behaviors [5.3]. Nevertheless, the variation between frequencies, shown in Tables 5.1 and 5.2, is consistent, which indicates that the cell populations are uniform between frequency measurements. So, any observed frequency dependence reflects intrinsic cell property change vs. frequency. With this assumption, there is a clear frequency dependence of both ε' and ε'' for all four cell classes, as is highlighted in Figure 5.11, whereas the 5.5 μm particle responses are much more uniform. Furthermore, we see that the difference in $\Delta\varepsilon''$ is more significant at lower frequencies for the two live species while the difference of the dead cells remains roughly the same at all frequencies. The uniformity of the dead cell responses can be explained by the leakage of cytoplasmic ions resulting from membrane damage caused by heat shocking the cells to cause cell death. The more significant frequency dependence of the live cells is due to the cell membrane having a larger effect at the lowest frequency (β-dispersion), 265 MHz, while at higher frequencies the cell membrane has little impact on measurements, and instead differences between the permittivity of the cell protoplasm and that of the media are observed. Similar phenomena for $\Delta\varepsilon'$ is observed, except for a spike in *S. cerevisiae* live cells at 2.38 GHz, where the membrane capacitance plays a significant role at 265 MHz but has little effect at higher frequencies. The large $\Delta\varepsilon'$ observed in *S. cerevisiae* at 2.38 GHz is

caused by a more drastic difference between ε' of the protoplasm and ε' of the media, but the reason it occurs at this particular frequency is unknown.

The frequency dependent properties make it difficult to compare the identification capabilities at higher frequencies with the two lowest frequencies, 800 MHz and 265 MHz. For some of the yeast classes we are only able to detect one of the permittivity values. Particularly at 265 MHz, where we only detect both ε' and ε'' for live *S. cerevisiae*. Due to this and the fact that live *S. pastorianus* is the only class where only ε'' is detectable, we can say that the differentiation of the two live species is solved at 265 MHz. However, for the remaining three classes we see that there is significant overlap to the point where we are unable to differentiate at all. Adding more classes at this frequency could lead to even worse performance. A similar trend is seen at 800 MHz, where we can detect ε' and ε'' for both live species but roughly half of the dead cells we only see a signal for ε'. This may be in part due to the lower sensitivity of the sensor at low frequencies, where the minimum detectable signals are nearly 10 times larger than at higher frequencies. Improved sensitivity at low frequencies could lead to increased microwave specificity. While this may make it difficult to differentiate more cell classes at these isolated frequencies, it may be useful when developing multiple frequency measurement prediction models. For example, the lower frequencies could be used to detect viability and higher frequencies could differentiate between these closely related species.

This is further supported with the prediction models that were generated where we found that 2.38 GHz and 265 MHz had the lowest cross validation errors. However, when

the models were used to make predictions on cell mixtures, we were unable to differentiate between the two dead cells across the species, getting a 0% value for *S. pastorianus* dead and a significantly smaller than expected number of 5.5 μm particles. Additionally, it appears that a significant number of *S. cerevisiae* live cells were misclassified as *S. pastorianus* live. This is likely due to slight differences of the media in the mixture measurements from the media that was used for individual cell type measurements. Other potential sources of errors include – multiple cells passing under the electrode simultaneously, cells passing under the region of the microstrip for which there is no ground plane, and the vertical location of the cell in the channel. Future efforts will address these problems as well as concurrent multi-frequency measurements of individual cells and minimizing sources of error.

References

[5.1]   Y. Cui, J. Sun, Y. He, Z. Wang, and P. Wang, "A simple, tunable, and highly sensitive radio-frequency sensor," *Appl. Phys. Lett.,* vol. 103, no. 6, Aug. 2013.

[5.2]   H.P. Schwan, "Electrical properties of tissues and cell suspensions: mechanisms and models," *Proceedings of 16th Annual International Conference of the IEEE Engineering in Medicine and Biology Society*, Baltimore, MD, USA, Nov. 1994, vol.1, pp. A70-A71.

[5.3]   K. Asami, T Yonezawa, " Dielectric behavior of wild-type yeast and vacuole-deficient mutant over a frequency range of 10 kHz to 10 GHz," *Biophysics Journal*, vol. 71, no. 5, pp. 2192-2200, Oct. 1996.

[5.4]   P. Tibayrenc, L. Preziosi-Belloy, and C. Ghommidh, "On-line monitoring of dielectrical properties of yeast cells during a stress-model alcoholic fermentation," *Process Biochemistry*, vol. 46, no. 1, pp. 193-201, Jan. 2011.

[5.5]   D. Kregiel, J. Berlowska, and B. Szubzda, "Novel permittivity test for determination of yeast surface charge and flocculation abilities," *Journal of Industrial Microbiology and Biotechnology*, vol. 39, no. 12, pp. 1881-1886, Dec. 2012.

[5.6]   J. Yao, T. Kodera, A. Sapkota, H. Obara and M. Takei, "Experimental study on dielectric properties of yeast cells in micro channel by impedance spectroscopy," *2014 International Symposium on Micro-NanoMechatronics and Human Science (MHS)*, Nagoya, Japan, Nov. 2014, pp. 1-4.

[5.7]   A. Ebrahimi, L.N. Csonka, and M.A. Alam, "Analyzing thermal stability of cell membrane of salmonella using time-multiplexed impedance sensing," *Biophysics Journal*, vol. 114, no. 2, pp.609-618, Feb. 2018.

[5.8]   R. Pethig and I. Schmueser, "Marking 100 years since Rudolf Höber's discovery of the insulating envelope surrounding cells and of the β-dispersion exhibited by tissue," *Journal of Electrical Bioimpedance*, vol. 3, no. 1, pp. 72-79, Jul. 2012.

[5.9]   G. G. Stewart, "Saccharomyces," in *Encyclopedia of Food Microbiology*, 2nd ed., C. A. Batt and M. L. Tortorello, Eds., Burlington, MA, USA: Elsevier, 2014, pp. 297-315.

[5.10] G.I. de Becze, " A microbiological process report; yeasts. I. Morphology," *Journal of Applied Microbiology*, vol. 4, no. 1, pp. 1-12, Jan. 1955.

[5.11] M. Ciani, L. Canonico, L. Oro, and F. Comitini, "Footprint of Nonconventional Yeasts and Their Contribution in Alcoholic Fermentations," in *Biotechnological Progress and Beverage Consumption*, 1st ed., A. M. Grumezescu and A. M. Holban, Eds., Burlington, MA, USA: Elsevier, 2019, ch. 14, pp. 435-465.

[5.12] A. Querol, E. Barrio, D. Ramón, "A Comparative Study of Different Methods of Yeast Strain Characterization," *Systematic and Applied Microbiology*, vol 15, no.3, pp. 439–446, Aug. 1992.

[5.13] R. Cody, "*Saccharomyces cerevisiae* and *S. pastorianus* species and strain differentiation by direct analysis in real time time-of-flight mass spectrometry," *Rapid Communications in Mass Spectrometry,* vol. 34, no. 17, May 2020.

[5.14] S. Torriani, G. Zapparoli, P. Malacrinò, G. Suzzi and F. Dellaglio, "Rapid identification and differentiation of *Saccharomyces cerevisiae, Saccharomyces bayanus* and their hybrids by multiplex PCR," *Letters in Applied Microbiology*, vol. 38, no. 3, pp. 239–244, Mar. 2004.

[5.15] K. Miller, Y. Gowtham, J. Henson, and S. Harcum, "Xylose isomerase improves growth and ethanol production rates from biomass sugars for both *Saccharomyces*

pastorianus and *Saccharomyces cerevisiae*," *Biotechnology Progress*, vol. 28, no. 3, pp.669-680, May 2012.

[5.16] S. Guyot, P. Gervais, M. Young, P. Winckler, J. Dumont, and H.M. Davey, "Surviving the heat: heterogeneity of response in *Saccharomyces cerevisiae* provides insight into thermal damage to the membrane," *Environmental Microbiology*, vol. 17, no. 8, pp. 2982-2992, Aug. 2015.

[5.17] P. Chen *et al.*, "Genome comparison and evolutionary analysis of different industrial lager yeasts (*Saccharomyces pastorianus*)," *Journal of the Institute of Brewing*, vol. 122, no. 1, pp. 42-47, Jan. 2016.

[5.18] P.B. Dengis, L.R. Nélissen, and P.G. Rouxhet, "Mechanisms of yeast flocculation: comparison of top- and bottomfermenting strains," *Applied and Environmental Microbiology*, vol. 61, no. 2, pp. 718–728, Feb. 1995.

[5.19] E.V. Soares, "Flocculation in *Saccharomyces cerevisiae*: a review," *Journal of Applied Microbiology,*, vol. 110, no. 1, pp. 1-18, Jan. 2011.

[5.20] M. Stoneman, A. Chaturvedi, D.B. Jansma, M. Kosempa, C. Zeng, and V. Raicu, "Protein influence on the plasma membrane dielectric properties: In vivo study utilizing dielectric spectroscopy and fluorescence microscopy," *Bioelectrochemistry*, vol. 70, no. 2, pp. 542-550, May 2007.

CHAPTER SIX

DETECTION OF *TRYPANOSOMA BRUCEI* LIFECYCLE STAGES

The parasite *Trypanosoma brucei* is a unicellular eukaryote that causes African sleeping sickness in humans and nagana disease in cattle. It has been studied extensively and has become a model organism for research on eukaryotic cell biology. The parasite completes its lifecycle between a vector tsetse fly and a mammalian host. The parasite is transferred to a mammalian host when a tsetse fly takes a blood meal and injects trypanosomes into the bloodstream. The bloodstream trypanosomes are transferred back when ingested by a tsetse fly, where the parasites are differentiated to procyclic forms in the fly midgut. When the parasite transfers between hosts it must undergo complex morphological and metabolic changes to adapt to the different extracellular environments since the bloodstream is rich in glucose and the fly midgut is not [6.14]. Both parasite forms are pleomorphic in size; in the insect vector, the parasite forms epimastigotes that typically range from 16-42 μm in length by 1-3 μm in width and in the mammalian host, the parasite forms trypomastigotes that typically range from 10-35 μm in length by 1-3 μm in width [6.15]. Additionally, the cells are not rigid in structure and are continuously changing in shape, making it difficult to visually observe and identify cell form (Fig. 6.1) [6.20]. As such, any observed differences in microwave properties of the two parasite forms is likely due to differences in internal structures since microwave frequencies are beyond the β-dispersion region and are thus able to penetrate the cell wall [6.21]. Compared with optical methods, which require periodic sampling and the use of chemical labels, microwave sensing is capable of continuous, label-free monitoring at the single

cell level, which could enable researchers to better study the complex interactions that occur within cell populations during differentiation. Additionally, the use of microwave properties allows for standardized definitions of cell lifecycle stages, removing ambiguity that could arise when defining stages by visual inspection, since they may be similar morphologically, as is the case for *T. brucei*. In this chapter the measured microwave properties of two lifecycle stages of *T. brucei* cells- bloodstream form (BSF) and procyclic form (PCF) are presented.

(a)   (b)
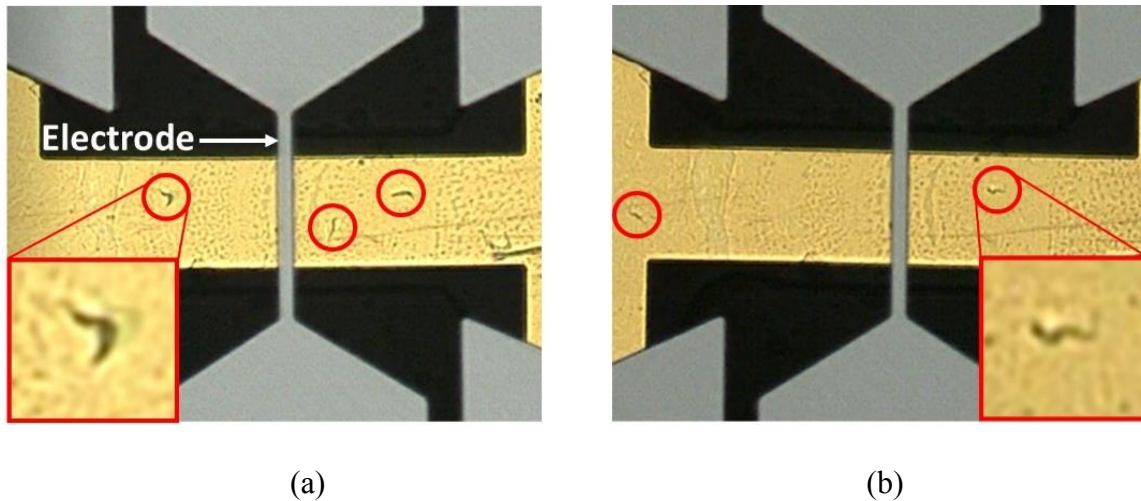
Fig. 6.1. A top view of the sensing zone with (a) procyclic form (PCF) and (b) bloodstream form (BSF) *T. brucei* cells near the microstrip line electrode.

6.1 *Trypanosoma brucei* preparation and measurements

The measurement system in Fig. 4.1 was used to measure *T. brucei* cells at 0.8, 1.32, 2.38, 3.96, 5.55, and 7.65 GHz. Multiple time domain measurements were taken of two lifecycle stages of *T. brucei* parasites - bloodstream form (BSF) and procyclic form

(PCF). BSF cells (strain 90-13) were grown in HMI-9 [6.9] supplemented with 10% heat-inactivated FBS (Corning, 35-101-CV) and 10% Nu-Serum IV (Corning, 355104) with growth conditions of 5% CO2 at 37°C. PCF cells (strain 29-13) were grown in SDM-79 [6.10] supplemented with 10% heat-inactivated FBS (Corning, 35-101-CV) with growth conditions of 5% CO2 at 25°C. Procyclic cells of the pleomorphic cell line (strain AnTat 1.1) were grown in SDM-79 or SDM-79θ (PCF media where glucose has been removed and dialyzed FBS (Corning, 35-071-CV) is used instead of standard serum) at normal PCF growth conditions (5% CO2 at 25°C). Cells were counted by optical flow cytometry and 1×10^7 cells were prepared for each measurement. The concentrated cells were subsequently diluted with media (HMI-9 or SMD-79) by a factor of 40:1 prior to microwave measurements.

Measurements were taken following the procedure outline in Chapter V. Prior to each measurement the sensor was calibrated using air and water. The sensor was calibrated a second time following each measurement to ensure that the system was stable during measurements. Fig. 6.2 shows typical permittivity measurement results of PCF and BSF cells at 1.32GHz. At 2.38 GHz and below, changes in complex permittivity were detected but changes in the real part of the impedance, Z_{mut}^{re}, were not seen for most cells. Likewise, above 2.38 GHz there were few $\Delta\varepsilon''$ signals, but changes in Z_{mut}^{re} were observed, as shown in Fig. 6.3. This could be caused by two things- first, it could be that ε'' of the cells were nearly the same as that of the media at higher frequencies, meaning that any differences are below the noise floor of the system, and/or second, the impedance mismatch of the sensor is larger at higher frequencies which increases
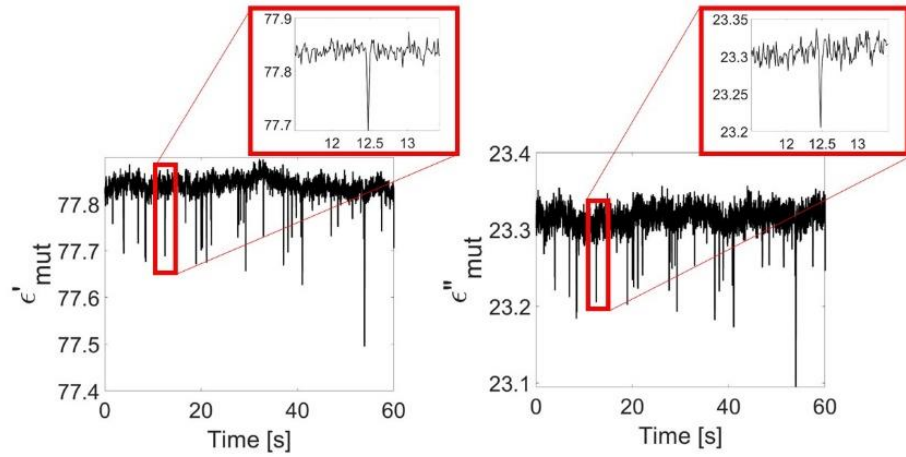
(a)
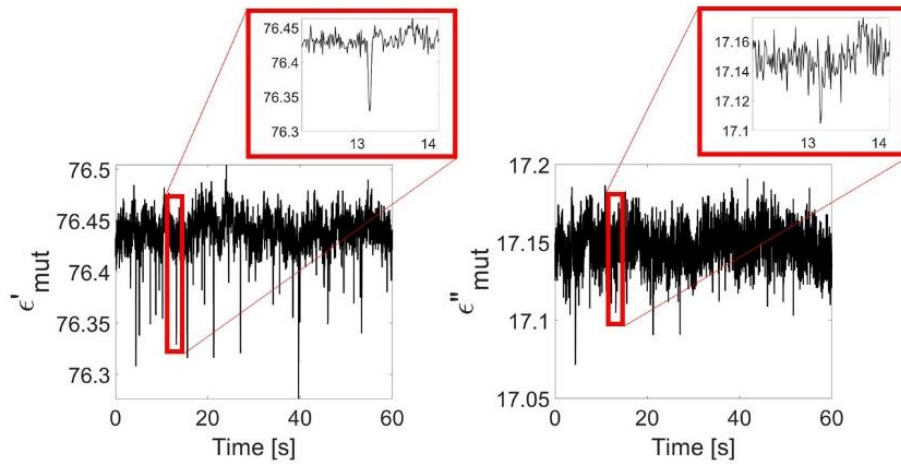
(b)

Fig. 6.2. Typical time domain complex permittivity measurement of (a) PCF and (b) BSF cells, taken at 1.32 GHz. Each signal is due to a single cell passing through the sensor. The peak change in ε'_{mut} and ε''_{mut} is used to obtain the cell population's response, shown in Figs. 6.7 and 6.8, where each point represents the peak change in ε'_{mut} and ε''_{mut}, or ε'_{mut} and Z^{re}_{mut} for a single cell.
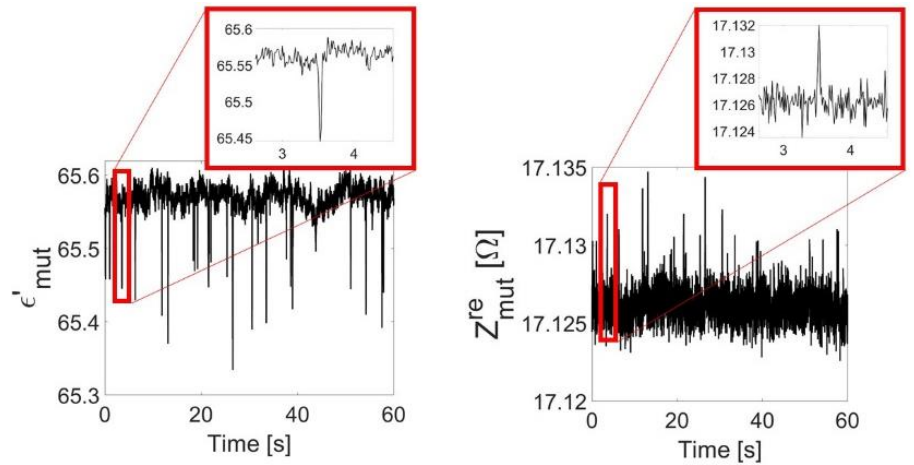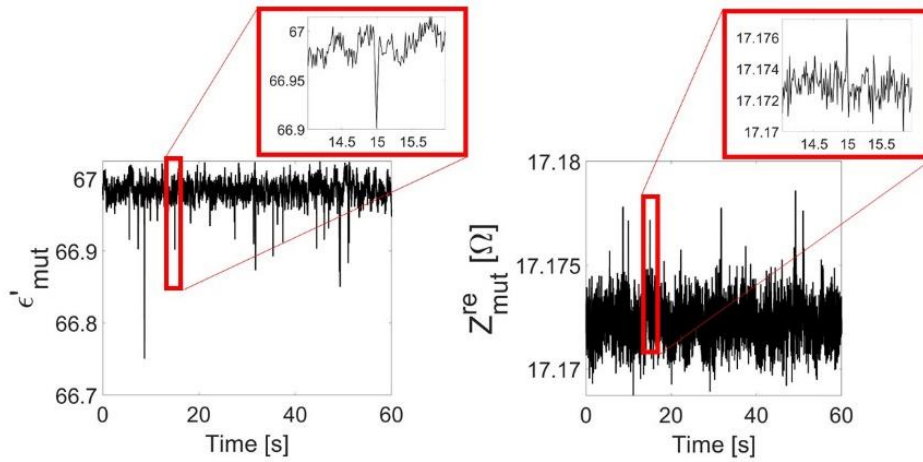
Fig. 6.3. Typical time domain permittivity and impedance measurements of (a) PCF and (b) BSF cells, taken at 7.65 GHz.

reflections (S_{11}) and adds noise to the through signal (S_{21}) of the VNA. This highlights the importance of measuring both the permittivity and impedance of cells, as it gives additional parameters if either $\Delta\varepsilon'_{mut}$ or $\Delta\varepsilon''_{mut}$ are not detectable. No signals for the imaginary part of the impedance, Z^{im}_{mut}, were detected at any frequency.

6.1.1 Effects of media

To ensure that any observed differences between cell forms were due to microwave properties of the cells and not that of the media, 3.4 μm x 5.1 μm ellipsoidal polystyrene particles were measured in the two media. As seen in Fig. 6.4 there was no discernable difference between the measured permittivity or impedance signals when the same particles were measured in different media, which indicates that the media are similar enough to not be a significant source of error. Hence, any differences between cell forms were caused by microwave properties of the two *T. brucei* forms.

(a)   (b)
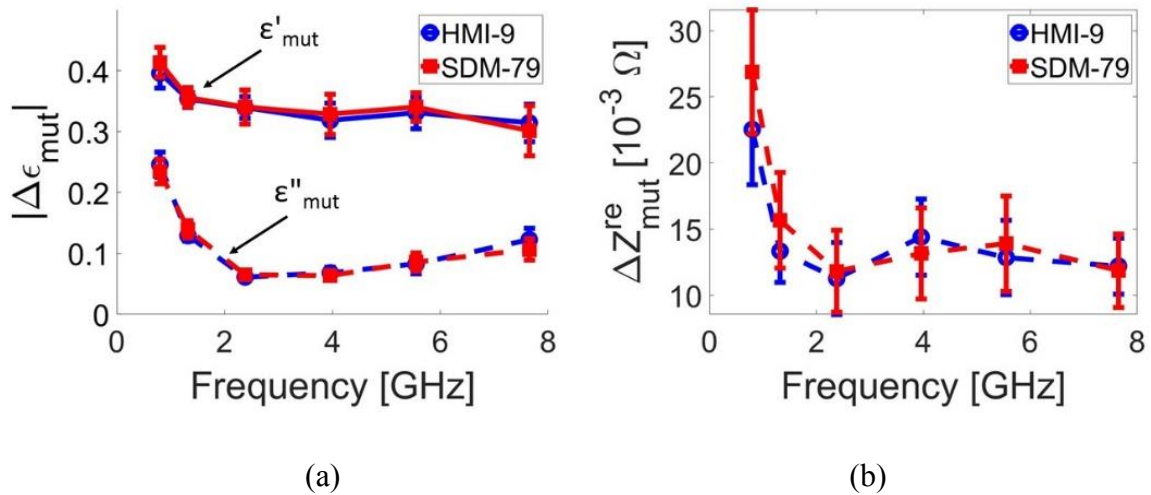
Fig. 6.4. Broadband measurements of (a) complex permittivity and (b) impedance of 3.4 μm x 5.1 μm ellipsoidal polystyrene particles in the media used to grow BSF (HMI-9) and PCF (SDM-79) cells.

6.2 Measurement Results

6.2.1 Frequency dependent impedance and permittivity

Average shifts in complex permittivity and the real part of impedance are summarized in Fig. 6.5. The difference in $\Delta\varepsilon'_{mut}$ between the two forms was smallest at 800 MHz and increased with frequency, while the reverse was true for $\Delta\varepsilon''_{mut}$, indicating that the differences between the cell forms observed at lower frequencies (2.38 GHz and below) were due mostly to differing microwave losses caused by cells, while differences at 5.55 GHz and 7.65 GHz were primarily due to differing dielectric polarizabilities. At 3.96 GHz there was not a significant difference in permittivity or impedance between the cell types. It should be noted that, while $\Delta\varepsilon''_{mut}$ is plotted at 3.96 GHz and above, and ΔZ^{re}_{mut} is plotted at 1.32 GHz and 2.38 GHz, these signals were only detected for particularly large cells, or when two cells passed under the electrode simultaneously. As such, the values in Fig. 6.7 at those frequencies may not be an accurate representation of average cells. It should also be noted that while the differences in ΔZ^{re}_{mut} were minimal, it does enable the use of multivariate machine learning techniques discussed in Chapter V.

TABLE 6.1
T. BRUCEI SAMPLE SIZES

Frequency (GHz)	BSF	PCF1	PCF2	PCF3
7.65	99	63	50	123
5.55	171	174	136	123
3.96	52	182	114	129
2.38	172	236	132	172
1.32	121	267	163	226
0.8	151	278	90	188
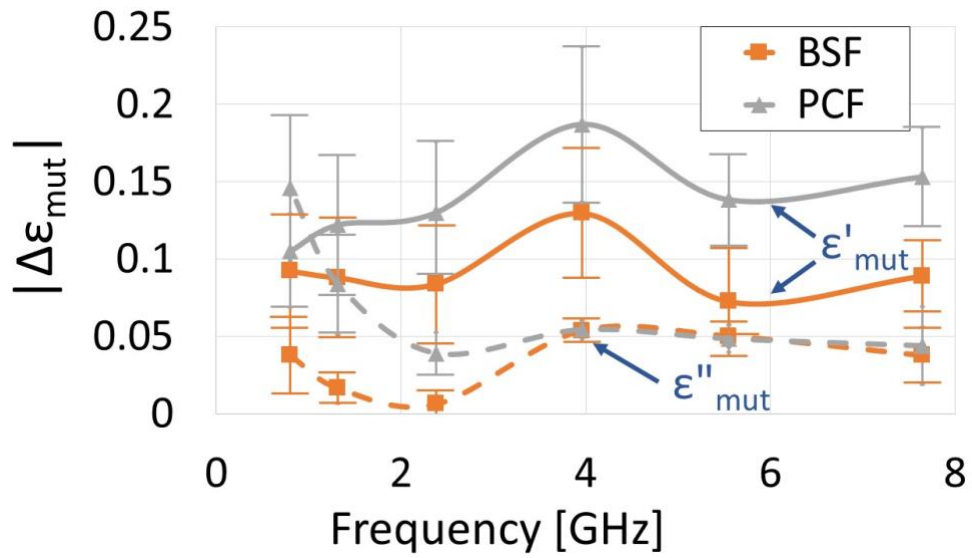
(a)
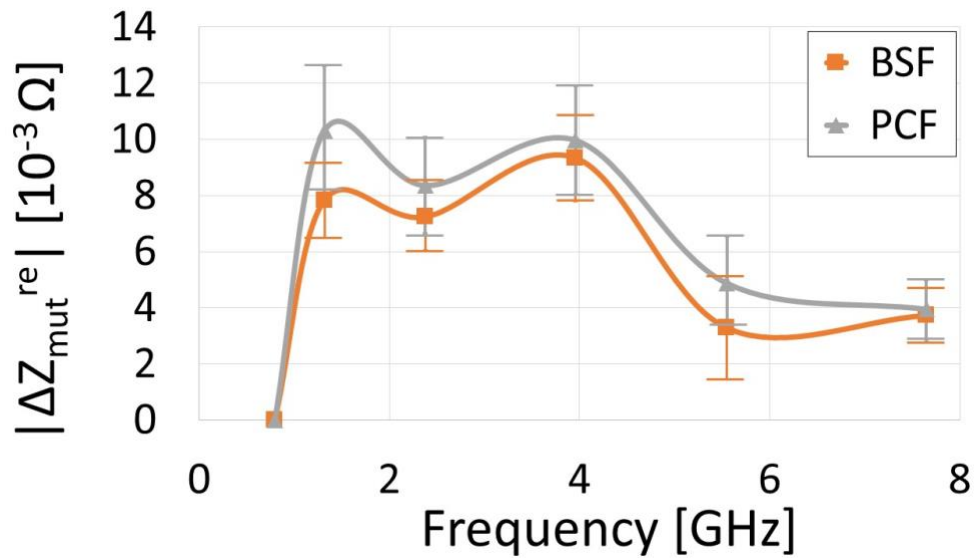
(b)

Fig. 6.5. Average shifts of (a) $|\varepsilon'_{mut}|$ and $|\varepsilon''_{mut}|$, and (b) Z^{re}_{mut} for the two *T. brucei* cell forms versus frequency.
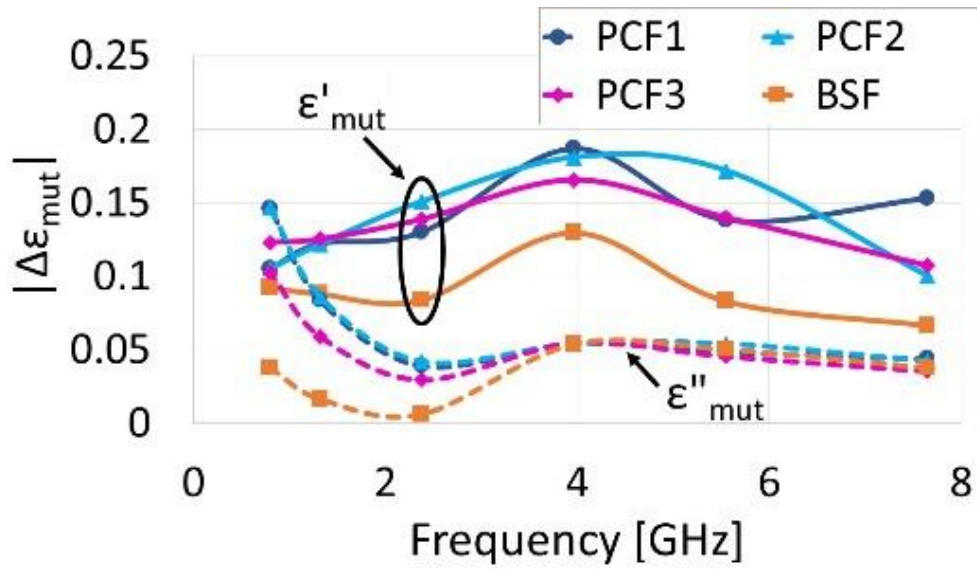
(a)
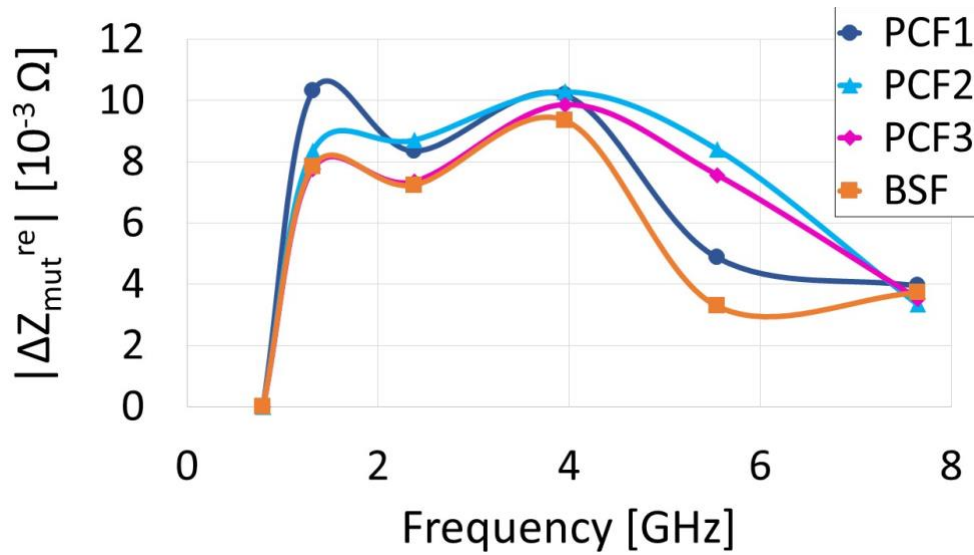
(b)

Fig. 6.6. Average shift of (a) $|\varepsilon'_{mut}|$ and $|\varepsilon''_{mut}|$ and (b) Z^{re}_{mut} for three lines of PCF cells and BSF cells versus frequency.

The total number of measurements is summarized in Table 6.1, where the values for 2.38 GHz and below represents the total number of complex permittivity signals measured, with one data point being a paired value of $\Delta\varepsilon'_{mut}$ and $\Delta\varepsilon''_{mut}$, and the values for 3.96 GHz and above represents the total number of real permittivity and impedance signals measured ($\Delta\varepsilon'_{mut}$ and ΔZ^{re}_{mut}).

To verify that any differences observed between BSF and PCF cells were independent of cell line, three lines of PCF cells were tested- the aforementioned strain 29-13 (a 427-strain parasite) (PCF1) and pleomorphic cell line (AnTat 1.1, an EATRO 1125 strain)) grown in either glucose-replete media (SDM-79) (PCF2) or glucose-deficient media (SDM-79θ) (PCF3). Average shifts in complex permittivity and the real part of impedance for the three PCF cell lines, plus the BSF cells, are summarized in Fig. 6.6.

The scatter plots shown in Fig. 6.7 also indicate that there was a difference in microwave properties between the two cell types, BSF and PCF, while the three PCF cell forms, shown in Fig. 6.8, have significantly more overlap. In these figures, each point in the plots represents the absolute value of the difference between the average baseline value and the peak change in ε'_{mut} and either ε''_{mut} or Z^{re}_{mut} for a single cell. In the following section, a quadratic discriminate analysis will be performed to characterize the system's ability to identify the two cell forms.

Fig. 6.7. Scatter plots of the measured shifts in the real and imaginary parts of permittivity at (a) 800 MHz, (b) 1.32 GHz, and (c) 2.38 GHz and the real parts of permittivity and impedance at (d) 3.96 GHz, (e) 5.55 GHz, and (f) 7.65 GHz of BSF and PCF *T. brucei* cells. Each data point represents a single cell, with the x-axis being the real part of permittivity and the y-axis the (a)-(c) imaginary part of permittivity or (d)-(f) the real part of impedance.

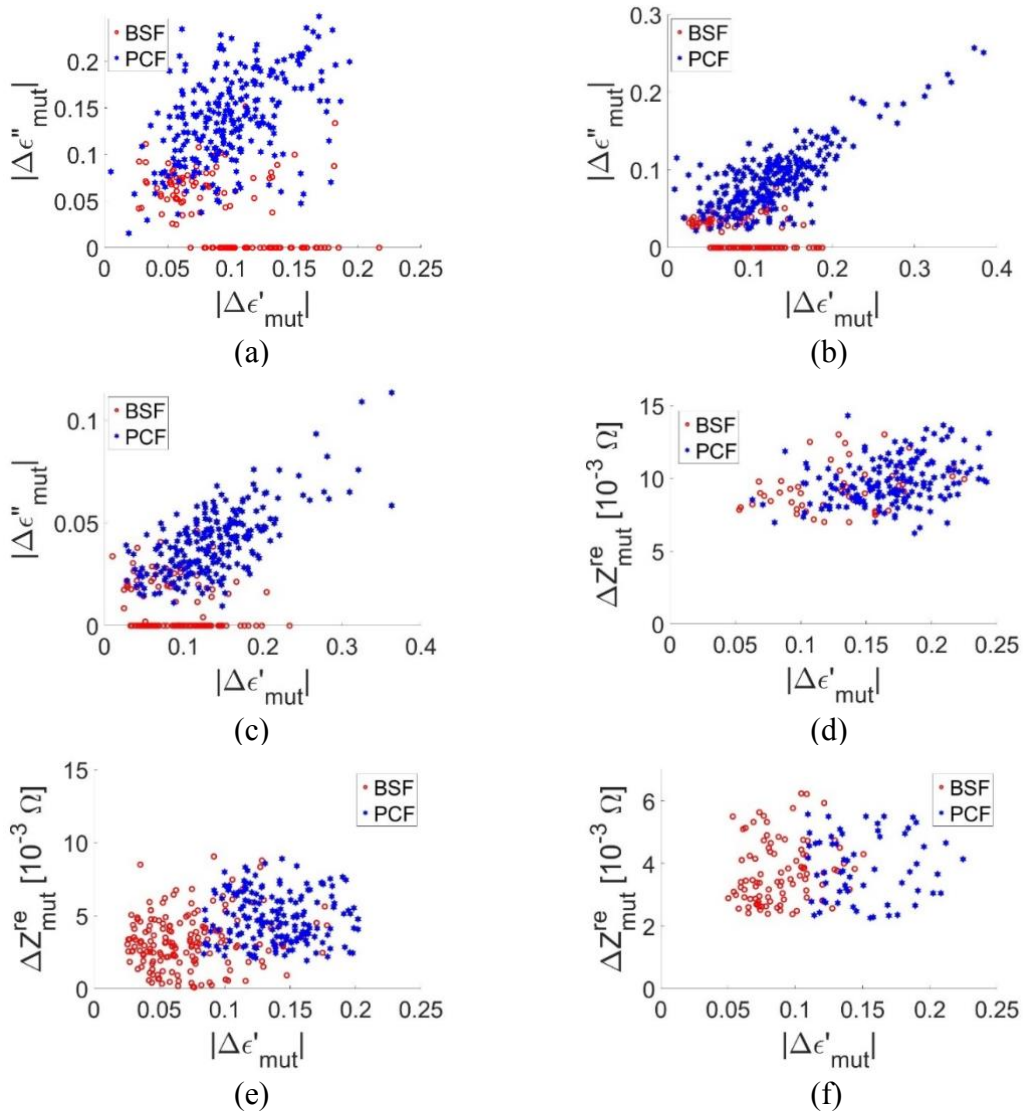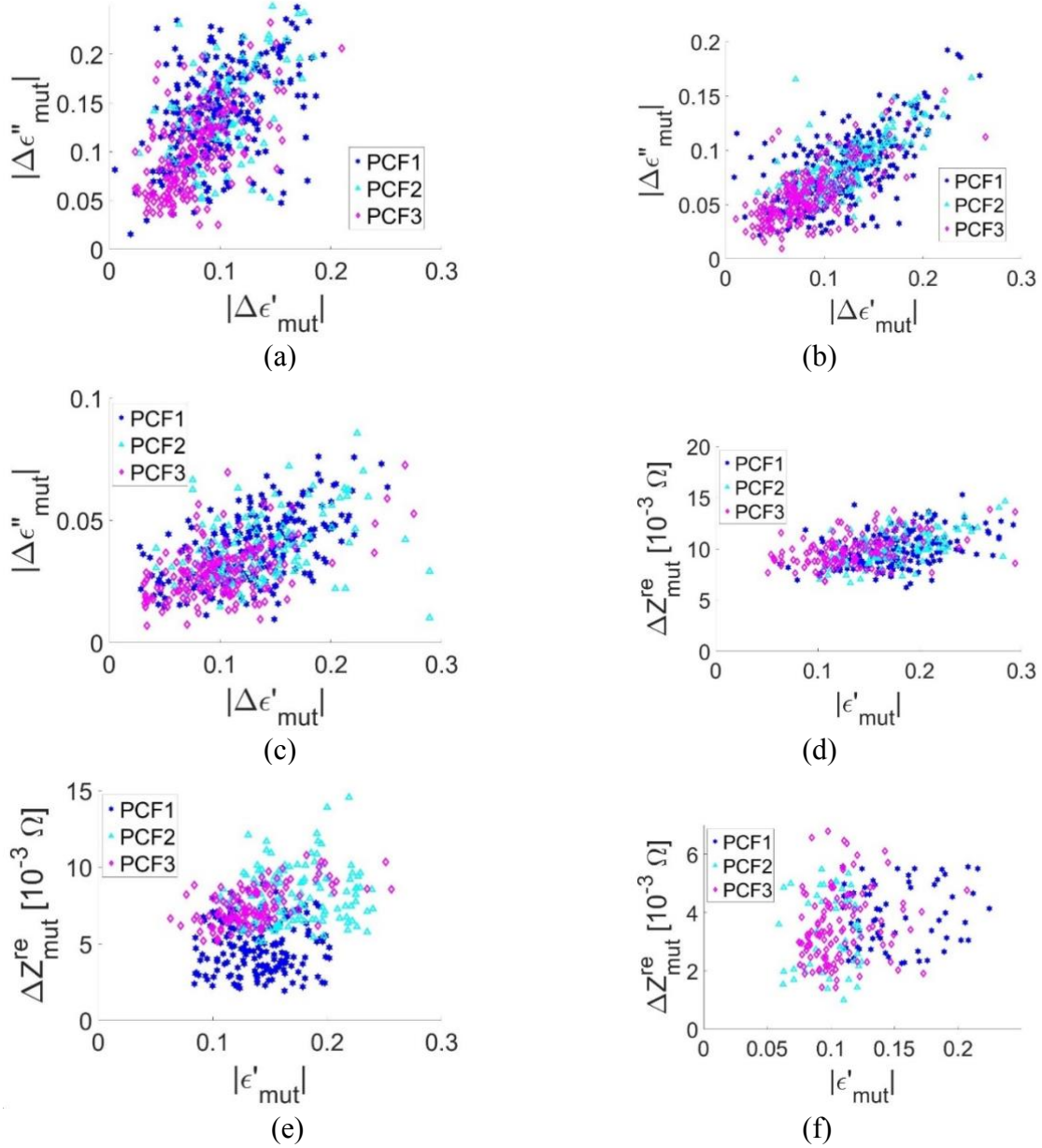Fig. 6.8. Scatter plots of the measured shifts in the real and imaginary parts of permittivity at (a) 800 MHz, (b) 1.32 GHz, and (c) 2.38 GHz and the real parts of permittivity and impedance at (d) 3.96 GHz, (e) 5.55 GHz, and (f) 7.65 GHz of three PCF cell lines. Each data point represents a single cell.

6.2.2 T. brucei life cycle classification

To test the ability to classify *T. brucei* cell forms a quadratic discriminate analysis (QDA) model was developed using the paired features summarized in Chapter V. At 2.38 GHz and below, $|\Delta\varepsilon'_{mut}|$ and $|\Delta\varepsilon''_{mut}|$ were used, and at 5.55 GHz and 7.65 GHz, $|\Delta\varepsilon'_{mut}|$ and ΔZ^{re}_{mut} were used. 3.96 GHz was left out due the inability to identify most cells. QDA uses the paired values at each frequency to create a quadratic decision surface to classify the two cell forms. The generated classification regions, with measured impedance and permittivity data overlaid, are shown in Fig. 6.9. To estimate the test error of the prediction model, 10-fold cross-validation was performed on the five prediction models shown in Fig. 6.9.

The cross-validation error was found to be uniform across all models, with 7.65 GHz having the largest error at 15.4% and 1.32 GHz having the smallest error at 10.1%. When the data from two additional PCF lines was added to the training model, where all three strains are combined as a single class, the cross-validation error was reduced to less than 10% for all frequencies except 7.65 GHz, which increased drastically to 24.6% due to the significant overlap of PCF2 and PCF3 with BSF. Comparing this to the three PCF cell lines on their own, i.e., when trying to classify the three PCF cell lines, the error increased to a minimum of 34% at 5.55 GHz, and a maximum of 50% at 2.38 and 3.96 GHz. This further validates that the ability to differentiate BSF and PCF cells is independent of cell line. This also indicates that using both permittivity and impedance data of cells can improve predictive performance of microwave sensors. Additionally, classification regions could be used for standardized definitions of cell lifecycle stages.
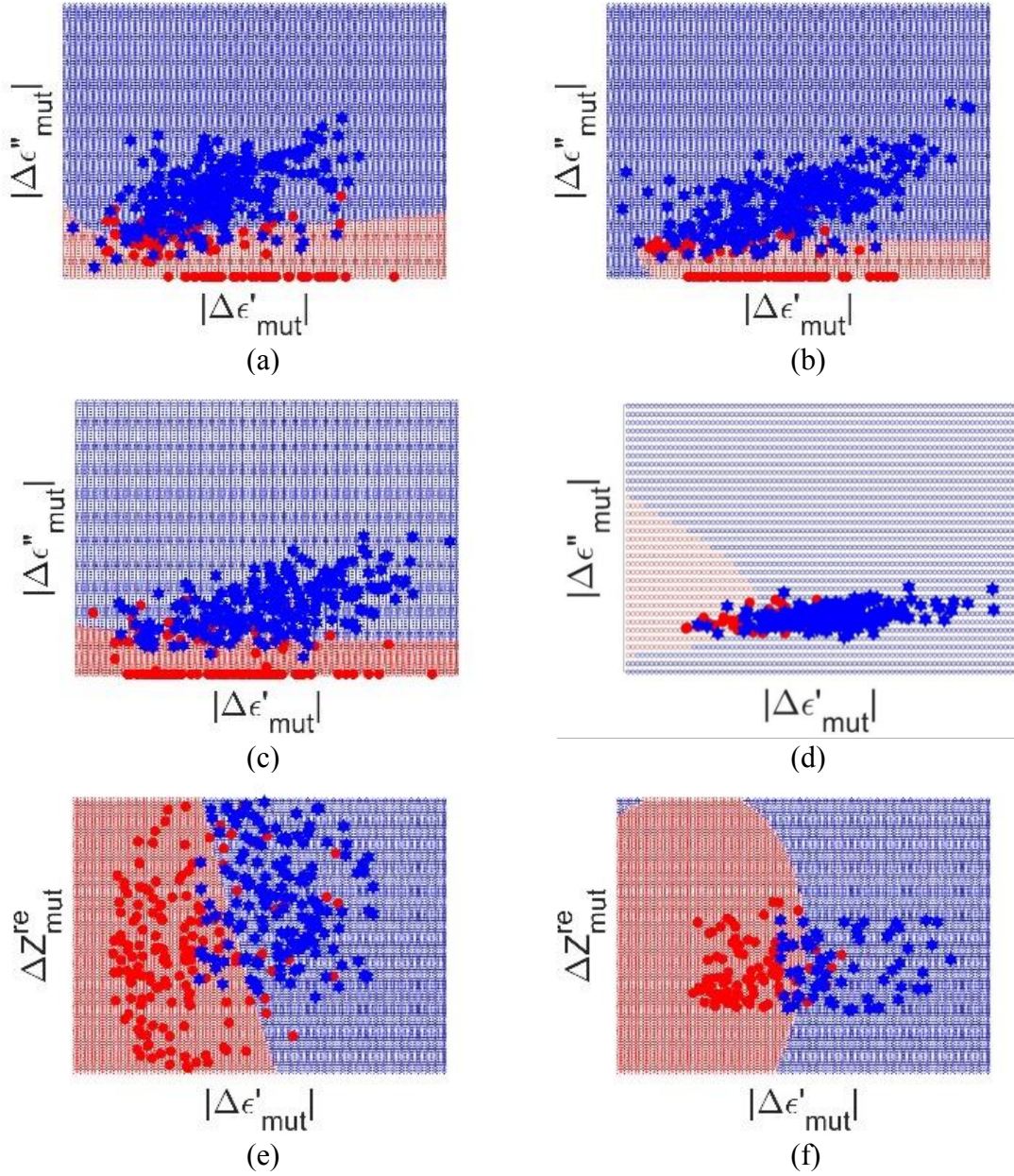
Fig. 6.9. Predicted classification regions with overlaid scatter plots of the training data using complex permittivity data at (a) 800 MHz, (b) 1.32 GHz, and (c) 2.38 GHz, and real permittivity and impedance data at (d) 3.96 GHz, (e) 5.55 GHz, and (f) 7.65 GHz.

As seen in Figs. 6.7 and 6.8, wide distributions were observed at every frequency, highlighting the fact that cells in the same lifecycle stage and culture have significant variations. Some of the variance may come from measurement errors, such as multiple cells passing under the electrode simultaneously, varying vertical locations of cells, and cells passing under the region of the sensor that does not contain a ground plane. However, sample dilutions and the large number of cells measured minimized these errors and we estimate by using optical microscopy that these errors occurred in less than 5% of signals. Additionally, the cultures were not controlled for cell phase within cultures, so it is likely there was a distribution of cell phases within cultures. For example, the BSF cells likely had a mixture of long slender (SL) and intermediate replicative forms which would likely have different microwave responses.

For all frequencies measured the differences between the average $|\Delta\varepsilon'_{mut}|$ (Fig. 6.6(a)) of the three PCF cell types were significantly less than that of BSF cells. The same can be said of $|\Delta\varepsilon''_{mut}|$ at 2.38 GHz and below, which were the frequencies used in the QDA model. The impedance signals (Fig. 6.6(b)) for the three PCF strains, however, overlap far less. Specifically at 7.65 GHz, where it is impossible to distinguish between the four cell types. Despite this, the PCF strains still varied significantly enough from BSF cells at 5.55 GHz to improve the cross-validation error from 14% to less than 10%. This indicates the potential for microwave dielectric and impedance measurements to differentiate BSF and PCF cells independent of cell strain, which could allow for this method to be applied to an array of strains without the need for strain specific calibration

or a vast database. Further improvements could be made by employing multi-frequency

measurements.

References

[6.1] Y. Cui, Y. He, and P. Wang, "A quadrature-based tunable radio-frequency sensor for the detection and analysis of aqueous solutions," *IEEE Microwave and Wireless Components Letters*, vol. 24, iss. 7, pp 490-492, Jul. 2014

[6.2] A. Valero, T. Braschler, A. Rauch, N. Demierre, Y. Barral, and P. Renaud, "Tracking and synchronization of the yeast cell cycle using dielectrophoretic opacity," *Lab on a Chip*, vol. 11, 1754-1760, Mar. 2011.

[6.3] D. Keck, C. Stuart, J. Duncan, E. Gullette, and R. Martinez-Duarte, "Highly Localized Enrichment of *Trypanosoma brucei* Parasites Using Dielectrophoresis," *Micromachines*, vol. 11, iss. 61, Jun. 2020.

[6.4] K. Asami, E. Gheorghiu, and T. Yonezawa, "Real-Time Monitoring of Yeast Cell Division by Dielectric Spectroscopy," *Biophysics Journal*, vol. 76, iss. 6, pp. 3345-3348, Jun. 1999.

[6.5] K. Asami, K. Takahashi, and K. Shirahige, "Progression of cell cycle monitored by dielectric spectroscopy and flow-cytometric analysis of DNA content," *Yeast*, vol. 16, iss. 5, pp. 1359-1363, Nov. 2000.

[6.6] T. Chen, F. Artis, D. Dubuc, J. Fournié, M. Poupot, and K. Grenier, "Microwave biosensor dedicated to the dielectric spectroscopy of a single alive biological cell in its culture medium," *2013 IEEE MTT-S Int. Microw. Symp. Dig. (MTT)*, Seattle, WA, USA, Jun. 2013, pp. 1-4.

[6.7] Z. Zhu, O. Frey, N. Haandbæk, D. S. Ottoz, F. Rudolf, and A. Hierlemann, "Real-time multi-parameter monitoring of immobilized single yeast cells via electrical impedance spectroscopy," *2013 Transducers Eurosensors XXVII: 17th Int. Conf. Solid-State Sensors., Actuators Microsyst. (TRANSDUCERS & EUROSENSORS XXVII),* Barcelona, Spain, Jun. 2013, pp. 1527-1530.

[6.8] C. Cannizzaro, R. Gügerli, I. Marison, and U. von Stockar, "Online biomass monitoring of CHO perfusion culture with scanning dielectric spectroscopy," *Biotechnology and Bioengineering,* vol. 84, iss. 5, pp. 597-610, Dec. 2003.

[6.9]   H. Hirumi and K. Hirumi, "Continuous cultivation of Trypanosoma brucei blood stream forms in a medium containing a low concentration of serum protein without feeder cell layers," *Journal of Parasitology*, vol. 75, iss. 6, pp. 985–989, Dec. 1989.

[6.10]   R. Brun and M. Schönenberger, "Cultivation and in vitro cloning of procyclic culture forms of Trypanosoma brucei in a semi-defined medium," *Acta Tropica*, vol. 36, iss. 3, pp. 289–292, Sep. 1979.

[6.11]   Y. Cui, J. Sun, Y. He, Z. Wang, and P. Wang, "A simple, tunable, and highly sensitive radio-frequency sensor," *Applied Physics Letters*, vol. 103, Jul. 2013.

[6.12]   J.A. Osterberg, N. Dahal, R. Divan, C.S. Miller, D. Moline, T.P. Caldwell, X. Yu, S.W. Harcum, and P. Wang, "Microwave sensing of yeast cell species and viability," *IEEE Transactions on Microwave Theory and Techniques,* vol. 69, iss. 3, pp. 1875-1886, Mar. 2021.

[6.13]   H.P. Schwan, "Electrical properties of tissues and cell suspensions: mechanisms and models," *Proceedings of 16th Annual International Conference of the IEEE Engineering in Medicine and Biology Society,* Baltimore, MD, USA, Nov. 1994, pp. A70-A71.

[6.14]   T.K. Smith, F. Bringaud, D.P. Nolan, and L.M. Figueiredo, "Metabolic reprogramming during the *Trypanosoma brucei* life cycle," F1000Res. 6 (2017) F1000 Faculty Rev-683.

[6.15]   J. Lee, G. Leedale, and P. Bradbury. *An Illustrated Guide to the Protozoa*, 2nd ed., Lawrence, Kansas, 2000.

[6.16]   K.R. Matthews, T. Sherwin, and K. Gull, "Mitochondrial genome repositioning during the differentiation of the African trypanonosome between life cycle forms is microtubule mediated," *Journal of Cell Science*, vol. 108, iss. 6, pp. 2231–2239, Jun. 1995.

[6.17]   I. Roditi, H. Schwarz, T.W. Pearson, R.P. Beecroft, M.K. Liu, J.P. Richardson, H.J. Biihring, J. Pleiss, R. Billow, R.O. Williams, and P. Overath, "Procyclin gene expression and loss of the variant surface glycoprotein during differentiation of *Trypanosoma brucei*," *Journal of Cell Biology*, vol. 108, iss. 2, pp. 737–746, Feb. 1989.

[6.18]   M.D. Janezic, D.F. Williams, V. Blaschke, A. Karamcheti, and C.S. Chang, "Permittivity characterization of low-k thin films from transmission-line measurements," *IEEE Transactions on Microwave Theory and Techniques,* vol. 51, iss. 1, pp. 132-136, Jan. 2003.

[6.19] K.C. Gupta, R. Garg, and I.J. Bahl, *Microstrip Lines and Slotlines*, 4th ed., Boston, Massachusetts: Artech House Publishers, 2013.

[6.20] G. Uilenberg, *A field guide for the diagnosis, treatment and prevention of African animal trypanosomosis*, 2nd ed., Rome, Italy, 1998.

[6.21] S. Grimnes, Ø.G. Martinsen, *Bioimpedance and Bioelectricity Basics*, 3rd ed., Cambridge, Massachusetts, 2015.

CHAPTER SEVEN

MICROWAVE RESISTANCE TEMPERATURE DETECTOR

Temperature is one of the most fundamental parameters of any physical system. Obtaining accurate temperature measurements in microfluidics is a challenge. The frequency and temperature dependent nature of polar liquids has been investigated thoroughly over the past several decades but precise temperature measurements in microfluidic chips is still a difficult task due to fast thermal transfer rates in small sample volumes, making it difficult to observe and account for local hot spots. In dielectric spectroscopy, where liquid references such as water and alcohols are often used due to being readily available in high purity, making their properties uniform and consistent between samples, inaccurate temperature measurements of reference materials can be a significant source of error when calibrating and testing instrumentation.

Contactless methods such as IR thermography enable remote temperature monitoring but have limited spatial resolution and low accuracy, often tens of degrees for metallic targets [7.5,7.6]. In situ methods based on fluorescence intensity ratio (FIR) provide high spatial resolution but low accuracy [7.7]. Dielectric sensing techniques have the advantage of fast response times; however, they are greatly limited by the types of samples they can use since the temperature-permittivity relationship is different for every liquid, as shown in Fig. 7.1, hence any formulation would only be valid for the specific liquid composition. [7.1,7.2].

7.1 Temperature Dependence of Permittivity

At RF and microwave frequencies polar liquids exhibit a relaxation behavior as shown in Fig. 7.1, where the relative permittivity is large at low frequency and decreases rapidly at the center relaxation frequency, f_r. The behavior can be described by the single-Debye relaxation equation

$$\varepsilon = \varepsilon_\infty + \frac{\varepsilon_s - \varepsilon_\infty}{1 + \frac{jf}{f_r}} = \varepsilon_\infty + \frac{\varepsilon_s - \varepsilon_\infty}{1 + j\omega\tau} \tag{7.1}$$

double-Debye relaxation equation

$$\varepsilon^* = \varepsilon_\infty + \frac{\varepsilon_s - \varepsilon_h}{1 + \frac{jf}{f_{r1}}} + \frac{\varepsilon_h - \varepsilon_\infty}{1 + \frac{jf}{f_{r2}}} \tag{7.2}$$

and various other formulations. The static effective permittivity, ε_s, and high-frequency effective permittivity, ε_∞, are both temperature dependent so the temperature should be monitored whenever using polar liquids as standards for calibration.

Resistive temperature detectors (RTDs) are standard temperature sensor due to their flexibility, simplicity, stability, and high thermal sensitivity. For dielectric spectroscopy, they are ideal thanks to the resistance of an electrode being invariant with permittivity. RTDs operate by measuring the temperature dependent resistance of an electrode, given as

$$\frac{dR}{R} = \alpha dT \tag{7.3}$$

which can be linearly approximated as
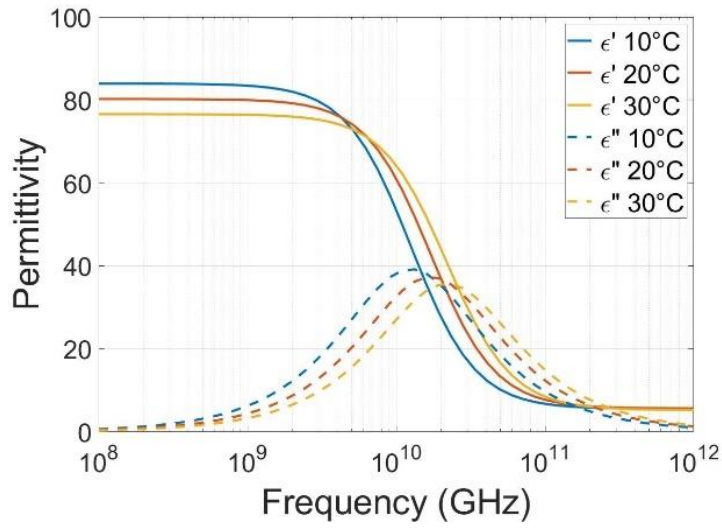
(a)
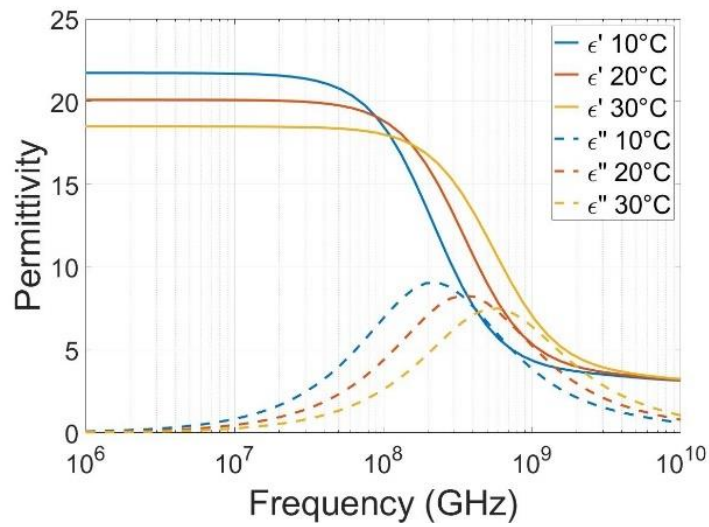
(b)

Fig. 7.1. Temperature dependent permittivity spectrum of (a) water and (b) isopropyl alcohol (IPA). The permittivity of water was calculated using the single-Debye equation (7.1) and IPA using the double-Debye equation (7.2).

$$R_T = R_{ref}\left(1 + \alpha\left[T - T_{ref}\right]\right) \tag{7.4}$$

where R_T and R_{ref} are the resistances at an unknown temperature $T\,°C$ and at a reference temperature $T_{ref}°C$, respectively, for a given conductor with temperature coefficient or resistance $\alpha(T)$. For a low-loss transmission line the loss from the conductor can be approximated as

$$\alpha_c \cong \frac{R}{2Z_0} \tag{7.5}$$

where the resistance of rectangular conductor with cross-sectional area A, length l, and resistivity ρ is

$$R = \rho\frac{l}{A} \tag{7.6}$$

Combining Equations (7.4)-(7.6) gives the temperature dependent conductivity loss as

$$\alpha_c = \frac{\rho\dfrac{l}{A}\alpha_{Au}\Delta t}{2Z_0} \tag{7.7}$$

with the constant temperature coefficient of resistance of gold, α_{Au}, given as 3.4 x 10^{-3}/°C [7.3]. From this it is clear that using a narrow width, thin film electrode maximizes the sensitivity of an RTD by minimizing the cross-sectional area and allows for a fast response time for the detector.

The microwave RTD in **Fig. 7.2** was fabricated using the liftoff process described above. The sensor was fabricated using two separate liftoff processes, the first used contact lithography to pattern the large metal structures and the second was done using electron-beam lithography to pattern a 500-nm wide, 500-μm long meandered microstrip electrode with 20/200-nm thick Cr/Au metal. A 40-um tall, 100-um wide
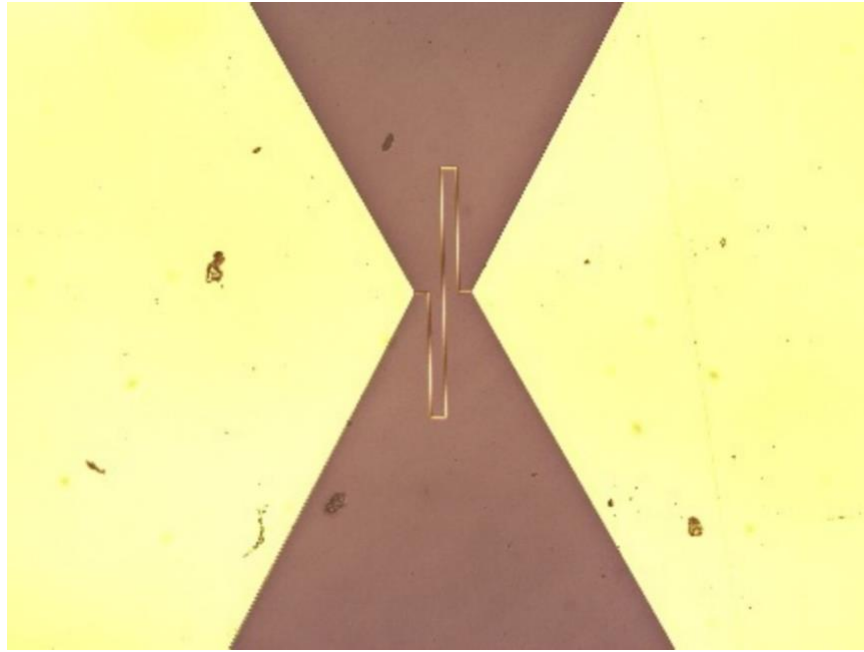
Fig. 7.2. (a) Microwave RTD sensor with PDMS microfluidic channel and (b) microscope image of the meandered microstrip electrode used as and RTD sensor.

polydimethylsiloxane (PDMS) microfluidic channel was bonded to the glass substate using oxygen plasma treatment [7.9].

In the experimental setup, shown in Fig. 7.3, the sensor is placed on top of a hot/cold plate inside a conductive tube to ensure uniform temperature. The hot/cold plate uses two resistance temperature detector (RTD) sensors and a proportional–integral–derivative (PID) controller to maintain stable temperatures. In this setup the full sensor setup is kept at the same temperature as hot/cold plate. Although the quartz substrate, microstrip feedline, and connectors also exhibit temperature dependent behavior, the change in loss tangent of the substrate over the desired operating range is less than 1% and $\Delta\alpha_c$ due to the microstrip feedlines and connectors is several orders of magnitude
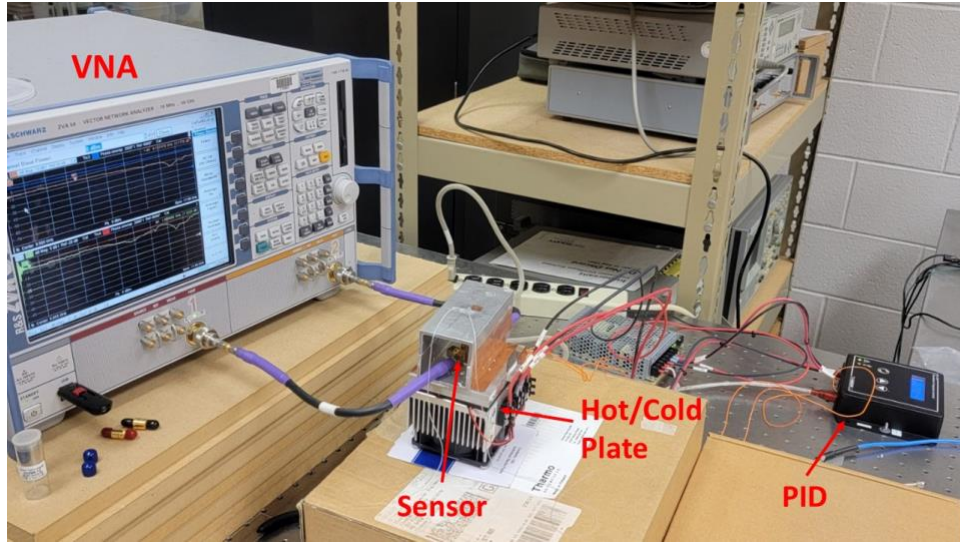
Fig. 7.3. Benchtop assembly showing the sensor inside a thermally conductive tube on a hot/cold plate. The temperature is controlled by the PID with two RTD sensors connected to the hot/cold plate.

smaller than $\Delta\alpha_c$ from the meander section, hence their contributions can be neglected [7.8].

7.2 Temperature Measurement Procedure

Due to the small cross-sectional area of the microstrip line and small loss tangent of the quartz substrate, the attenuation of the sensor without a sample ($\varepsilon_{mut} = 1$) can be assumed to be entirely conductive loss from the microstrip meander section. When a liquid sample is added the change in loss will be a combination of a change in conductive loss due to temperature change of the microstrip and dielectric loss of the sample, i.e.

$$\alpha = \alpha_{ref} + \alpha_c(T) + \alpha_d(\varepsilon) \tag{7.8}$$

116

where α is the measured attenuation, α_{ref} is the attenuation without *mut* at a reference temperature, and α_c and α_d are the added conductive and dielectric loss from a liquid sample.

The temperature sensor can be calibrated by measuring the attenuation constant at a reference temperature, generally 0°C or 20°C, to get R_{ref} and T_{ref} from Equations (7.2) and (7.3), and the temperature can be determined from

$$T = \frac{1}{\alpha}\left(\frac{R_T}{R_{ref}} - 1\right) + T_{ref} \tag{7.9}$$

Then the permittivity can be measured after the interferometer is calibrated. The temperature and permittivity dependent propagation constant is

$$\gamma = \alpha + j\beta = \alpha_{ref} + \alpha_c(T) + \alpha_{mut}(\varepsilon'') + j\beta_{mut}(\varepsilon') \tag{7.10}$$

and the permittivity can be determined using the Green's function method variational expression for a three-layer microstrip, along with the single layer reduction (SLR) technique, which reduces the multilayer microstrip into an equivalent single layer structure and allows for the use of the familiar microstrip equations, with the equivalent height defined as [7.4]

$$h_{eq} = h_1 \tag{7.11}$$

The equivalent permittivity of a single layer microstrip is

$$\varepsilon'_{eq} = \frac{\varepsilon'_{eff} - 1}{q} + 1 \tag{7.12a}$$

$$\varepsilon''_{eq} = \frac{\varepsilon''_{eff}}{q} \tag{7.12b}$$

with filling factor q defined as

$$q = \frac{1}{2}(1 + p) \tag{7.13}$$

where

$$p = \begin{cases} \left[1 + \dfrac{12h_{eq}}{W}\right]^{-1/2}, & for\ \dfrac{W}{h_{eq}} > 1 \\[3mm] \left[1 + \dfrac{12h_{eq}}{W}\right]^{-1/2} + 0.04\left[1 - \dfrac{W}{h_{eq}}\right]^2, & for\ \dfrac{W}{h_{eq}} \le 1 \end{cases} \tag{7.14}$$

A more accurate filling factor could then be obtained by using an iterative approach [7.10, 7.11]. However, for the temperature sensor presented here the first approximation of the filling factor was found to be sufficiently accurate.

A comparison of the model against HFSS simulation using the structure shown in Fig 3.2(b) for a 500-nm wide, 500-μm long microstrip with a quartz substrate (ε_{er1} = 3.78, h_1 = 1 mm), and a 40 μm tall microfluidic channel (h_2 = 40 μm) in PDMS (ε_{r3} = 2.6, h_3 = 2 mm), shown in Fig 7.4, where ε_{er2} is the *mut* permittivity (ε_{mut}).

When the sensor is connected to the microwave interferometer with an empty microfluidic channel (ε_{mut} = 1+j0) and the temperature is varied, the resistance of the microstrip line change but the propagation constant will remain constant. When a dielectric liquid is added both the propagation constant and the conductive loss will change with temperature. This effect can be seen in Fig. 7.5, where the phase of S_{21} remains mostly constant when the temperature of the empty sensor is increased and the magnitude of S_{21} changes with temperature (Fig. 7.5(a)), and when water is added to the sensor both $\angle S_{21}$ and $|S_{21}|$ change with temperature (Fig. 7.5(b)).
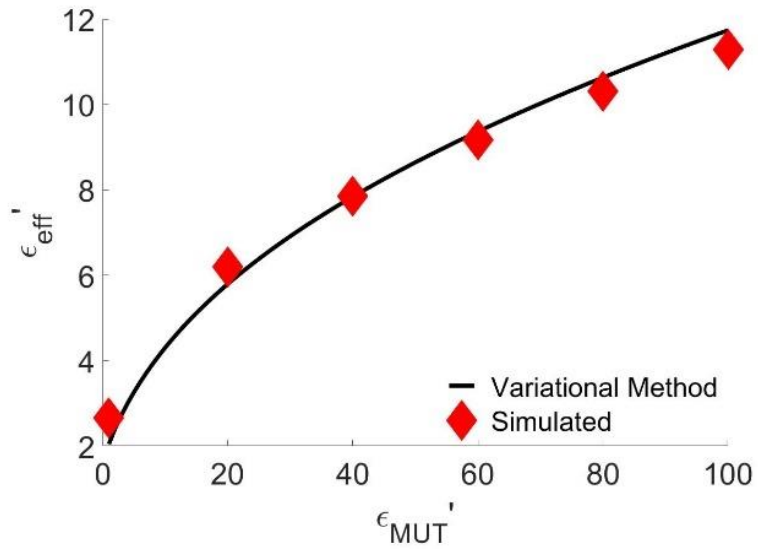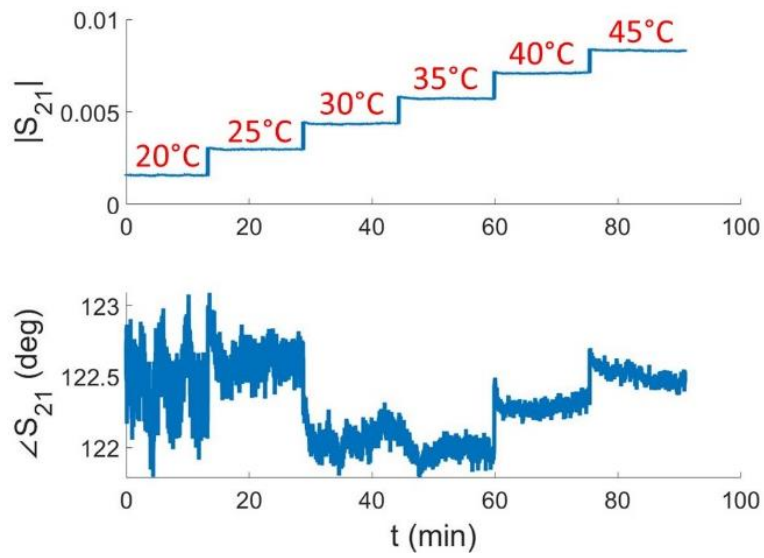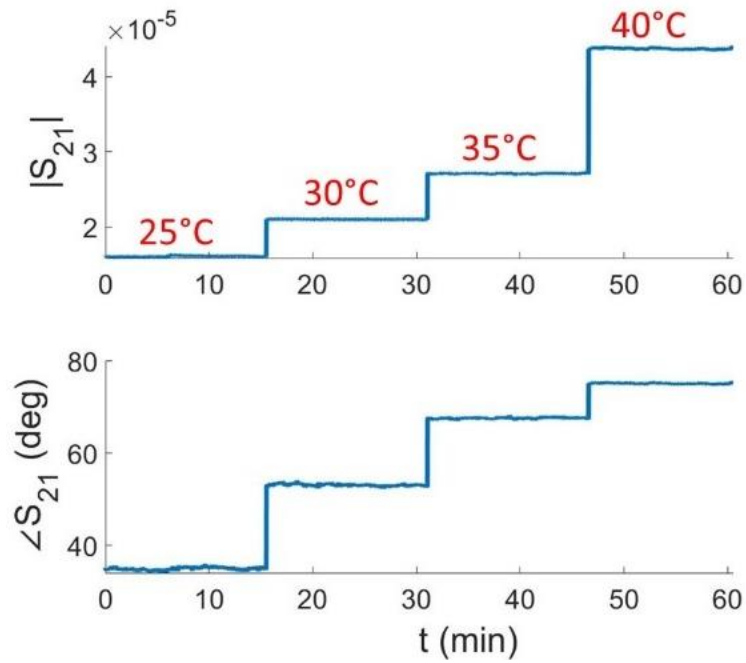
(a)
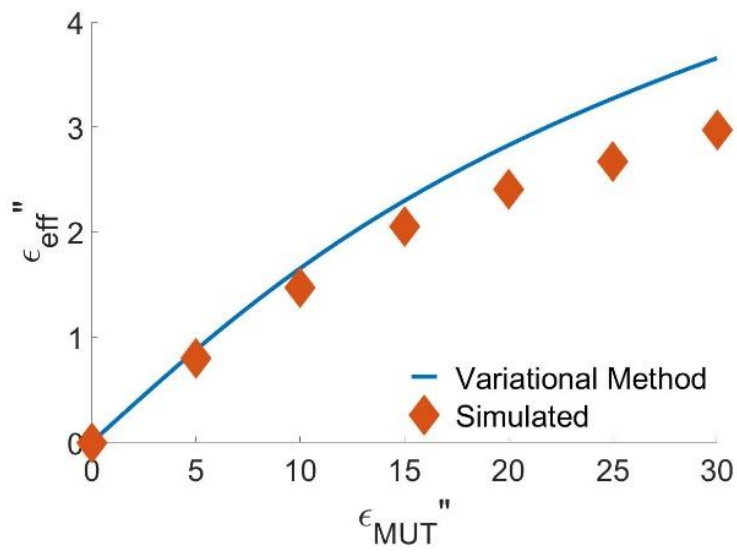
(b)

Fig. 7.4. Comparison of the (a) real and (b) imaginary permittivity calculations from the variational method with SLR model of a three-layer microstrip line and HFSS simulation of the RTD sensor.

Fig. 7.5. Time domain measurements of the microwave RTD sensor while (a) empty and (b) with water.

Fig. 7.6 shows a comparison of the response of the sensor at varying temperatures with IPA and DI water. Since water has a larger permittivity that IPA, as seen in Fig. 7.1, both the magnitude and phase of S_{21} have a larger response when compared to the empty (air) baseline. When all *mut* is removed from the sensor and the test assembly is brought back to the baseline temperature of 20°C after 5 hours of measurements, the S_{21} signal returns to its baseline values, showing the stability and repeatability of the system.
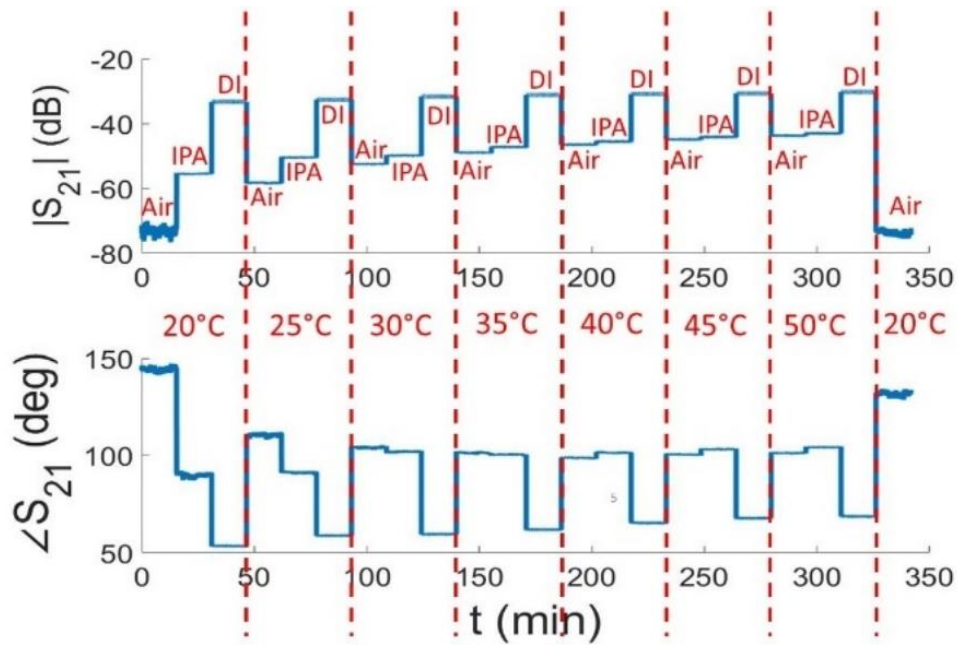

Fig. 7.6. Time domain response of the microwave RTD sensor with the temperature varied from 20°C to 50°C.

From the measurement in Fig. 7.5(a) the limit of detection for the RTD is approximately ±0.1°C, assuming minimum SNR of 3:1. If higher sensitivity is required the microstrip can be lengthened, using Eq. 7.7 to determine the length based on desired

sensitivity. If higher spatial resolution is needed, e.g. for smaller volumes of solute, the electrode length can be reduced.

References

[7.1]   A.P. Gregory and R.N. Clarke, "Tables of the complex permittivity of dielectric reference liquids at frequencies up to 5 GHz," Andrew Gregory, NPL Report MAT 23, 2012.

[7.2]   D. Wang, G. Yesiloz, M.S. Boybay, and C. Ren, "Microwave temperature measurement in microfluidic device," *Lab on a Chip,* vol. 16, iss. 12, pp. 2192-2197, May 2016.

[7.3]   W.F. Leonard and R.L. Ramey, "Temperature coefficient of resistance in thin metal films," *Journal of Applied Physics,* vol. 37, pp. 3634-3635, Feb. 1966.

[7.4]   A.K. Verma and A. Bhupal, "Dielectric loss of multilayer microstrip line," *Microwave and Optical Technology Letters*, vol 17, iss. 6, pp. 368-370, Apr. 1998.

[7.5]   J. Christofferson, K. Maize, Y. Ezzahri, J. Shabani, X. Wang, and A. Shakouri, "Microscale and Nanoscale Thermal Characterization Techniques." *ASME Journal of Electronic Packaging.* vol. 130, iss. 4, December 2008.

[7.6]   J. Christofferson, K. Maize, Y. Ezzahri, J. Shabani, X. Wang, and A. Shakouri, "Infrared Temperature Control System for a Completely Noncontact Polymerase Chain Reaction in Microfluidic," *Analytical Chemistry,* vol. 79., iss. 4, pp. 1294-1300, Feb. 2007.

[7.7]   F. Yang, N. Yang, X. Huo, and S. Xu, "Thermal sensing in fluid at the micro-nano-scales." *Biomicrofluidics.,* vol. 12, iss. 4, 2 Jul. 2018.

[7.8]   Y. Zhou, E. Li, G. Guo, Y. Gao, and T. Yang, "Broadband Complex Permittivity Measurement of Low Loss Materials Over Large Temperature Ranges by Stripline Resonator Cavity Using Segmentation Calculation Method," *Progress in Electromagnetics Research,* vol. 113, pp. 143-160, Jan. 2011.

[7.9]   A. Borók, K. Laboda, and A. Bonyár, "PDMS Bonding Technologies for Microfluidic Applications: A Review," *Biosensors*, vol. 11, iss. 8, Aug. 2021.

[7.10] A.K. Verma and G.H Sadr, "Unified dispersion model for multilayer microstrip line," *IEEE Transactions on Microwave Theory and Techniques*, vol. 40, iss. 7, pp. 1587–1591, July 1992.

[7.11] A.K. Verma, P. Singh, and L. Matekovits, "Strip-width and slot-gap dependent equivalent isotropic substrate and dispersion characteristics of asymmetric coplanar waveguide, symmetric coplanar waveguide, and microcoplanar strip line on anisotropic substrates," *IEEE Transactions on Microwave Theory and Techniques*, vol. 62, iss. 10, pp. 2232–2240, Oct. 2014.

CHAPTER EIGHT

CONCLUSION

This dissertation presented a novel microwave flow cytometer a microwave flow cytometer for single cell detection and characterization. In Chapter II the operation of an RF interferometer was described, and it was demonstrated that a single stage RF interferometer can have negative group delay (NGD) and superluminal propagation (SP) properties, and power ration dependent frequency regions with large positive group delay. These abnormal frequency regimes are formed due to RF guided wave interference. Nevertheless, material-under-test (*MUT*) still interacts with traveling waves. The arrangement of two-stage interferometers potentially enables high sensitivity operations. When the first stage is built with commercial power dividers, the measured frequency sensitivity was increased by up to 7 times, which is comparable to the improvements with filters and resonators. When using a quadrature hybrid based first stage, the frequency sensitivity improvement was up to 20 times. The improvements occur at frequencies where the signal group delay is slow, regardless of if it is positive or negative. Thus, two-stage RF interferometers, like other microwave sensors [8.1], are attractive choices for many of biomedical, electronic, and industrial applications.

In Chapter III a broadband microstrip line sensor for dielectric spectroscopy and microwave flow cytometry was presented. The design methodology and fabrication process were described. The sensor was shown to have high sensitivity and uniformity, which removes cell measurement uncertainty from unknown vertical cell position. An analytical model based on the Green's function formulation of the variational method

124

with the TTL technique was also presented and used to determine a closed form quasi-static model for microstrip line sensors that can be used to extract the permittivity and characteristic impedance of multilayer microstrip sensor.

In Chapter IV the microwave flow cytometer system was developed using the interferometer system described in Chapter II and microstrip line sensor from Chapter III. Models were presented for extracted the unknown permittivity and impedance from liquid *mut* in any sensor in a microwave interferometer. The models were validated using HFSS simulations and standard liquid permittivities (IPA and ethanol), the models and validation measurements showed excellent agreement with the theoretical models.

In Chapter V the microwave flow cytometer platform was used for single yeast characterization. We showed that membrane differences in two *Saccharomyces* yeast cell species, as well as two viability states, resulted in observable difference in both the real and imaginary parts of the permittivity at 265 MHz. We also showed that increased permeability of the cell membrane in dead cells, induced by heat shock, resulted in lower permittivity inside the cells compared with live cells of the same species at 800 MHz and above. These properties were then used to differentiate between the two yeast species and determine their viability, as well as differentiate signals from polystyrene particles from that of the cells.

The measurements were validated by creating machine learning prediction models at each frequency and testing them with mixtures containing live and dead cells from the two species and 5.5 μm particles. Of the frequencies tested, 2.38 GHz had the highest degree of specificity, indicating that cells have a stronger frequency dependence than was

previously known and that this frequency dependence can be exploited for microwave cell characterization measurements.

In Chapter VI the results of complex microwave permittivity and impedance measurements of two lifecycle stage forms of *T. brucei* cells was presented. The microwave flow cytometer was used to obtain in-flow measurements of BSF and PCF cells at multiple frequencies and demonstrate the system's ability to identify the two cell forms. Three additional lines of PCF cells were measured to show that the ability to identify cell forms is independent of cell strain. Additionally, we showed that the cells have a stronger ε'' dependence at lower frequencies (2.38 GHz and below) and a stronger ε' dependence above 2.38 GHz. For measurements where ε'' could not be detected, due to either ε'' of the cells matching that of the media or large reflections caused by impedance mismatches, impedance signals were be used to improve classification performance. Lastly, polystyrene particles were used to show that differences in cell media had negligible effects on measurement accuracy. This leads to the conclusion that $\Delta\varepsilon'$ and $\Delta\varepsilon''$ measurements could be used to identify the two *T. brucei* lifecycle stage forms at lower frequencies (2.38 GHz and below), and $\Delta\varepsilon'$ and ΔZ_{real} measurements could be used at higher frequencies (5.55 GHz and above). Measurements were validated using a QDA prediction model, which had a maximum cross-validation error of 15.4% when using only one PCF strain and an error of less than 10% when using multiple PCF strains, showing that microwave-based sensors have great promise in label-free, real-time monitoring of cell cycles.

Chapter VII presented a highly sensitive microwave RTD sensor. The sensor was fabricated by electron-beam lithography to minimize the cross-sectional area of the electrode and maximize sensitivity. The sensor is capable of measuring temperature in a microfluidic channel to within 0.1°C. A model is presented to extract both the *mut* permittivity and temperature and it is demonstrated that temperature sensing mechanism is independent from the *mut* permittivity effects.

References

[8.1]   A. Ebrahimi, W. Withayachumnankul, S. Al-Sarawi, and D. Abbott, "High-sensitivity metamaterial-inspired sensor for microfluidic dielectric characterization," *Sensors Journal, IEEE,* vol. 14, pp. 1345-1351, 2014.

APPENDICES

Appendix A

Confusion Matrices for Yeast Classification Models

Figures A1 and A2 provide the confusion matrices for all classification models presented in Chapter V. The two lowest frequencies, 265 MHz and 800 MHz, have several data points with only a single measurement value (ε' or ε''), so QDA is not appropriate since it assumes a two-dimensional Gaussian distribution. At these frequencies linear discriminant analysis (LDA) is used. QDA is used for frequencies 2.38 GHz and above and KNN is used for all frequencies.
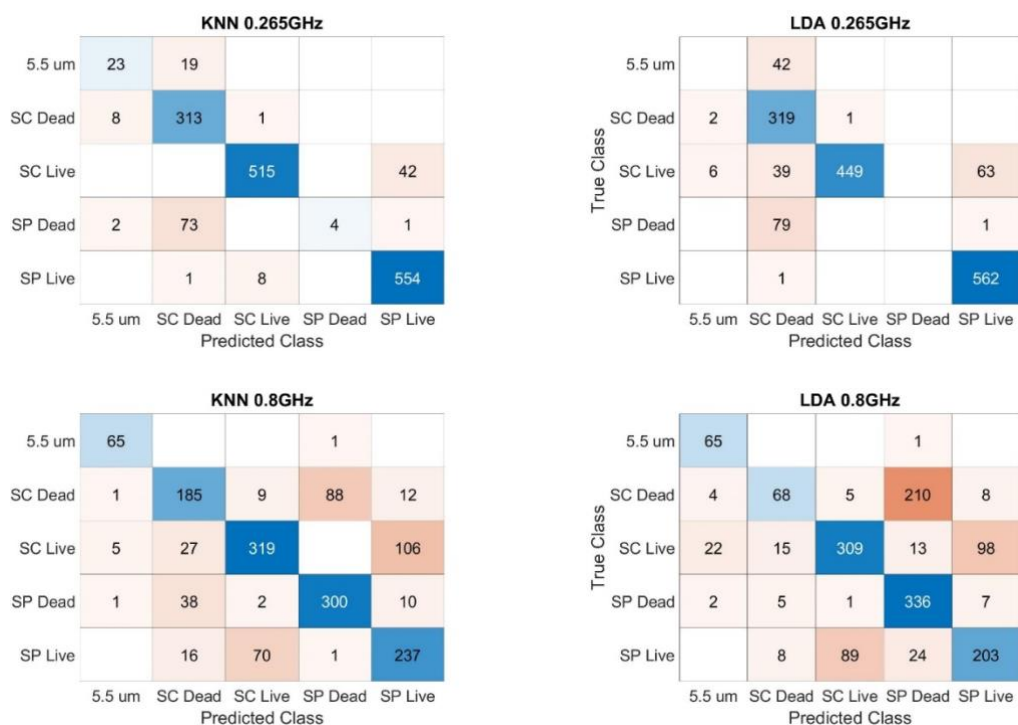

Figure A1. Confusion matrices for the two lowest frequency measurements used for yeast cell classification in Chapter V.
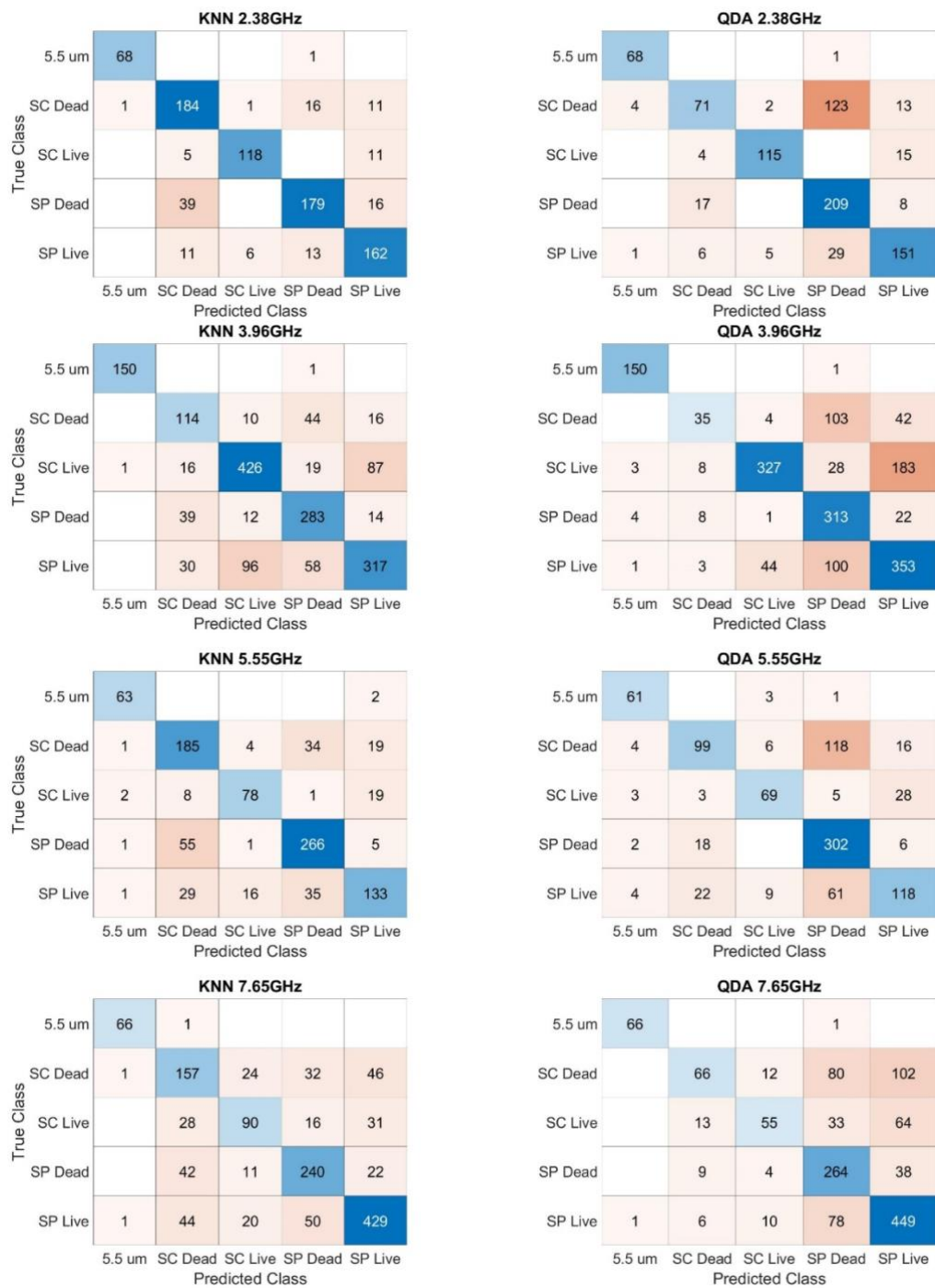
Figure A2. Confusion matrices for the four highest frequency measurements used for yeast cell classification in Chapter V.

Appendix B

Confusion Matrices for *T. brucei* Classification Models

The figures below provide the confusion matrices for all classification models

presented in Chapter VI. Models were created for the following data sets

1. Figure B1: BSF and PCF1 cells (strain 1 in Chapter VI).

2. Figure B2: All three strains of PCF cells without BSF cells.

3. Figure B2: BSF and PCF cells with all three strains of PCF cells combined into

   one class.

Tables B1, B2, and B3 give the cross-validation errors for the models created for

each of the three data sets described above. For all data sets QDA and KNN models were

created and for all data sets the two highest frequencies, 7.65 GHz and 5.55 GHz, use ε_{re}

and Z_{re} data, all other frequencies use ε_{re} and $\varepsilon_{im,}$ as described in Chapter VI.

TABLE B1
CROSS-VALIDATION ERRORS FOR DATA SET I

Frequency (GHz)	QDA	KNN
7.65	15.4%	17.3%
5.55	13.9%	15.9%
3.96	18.7%	20.4%
2.38	11.0%	13.2%
1.32	10.1%	10.8%
0.80	13.3%	14.2%

TABLE B2
CROSS-VALIDATION ERRORS FOR DATA SET II

Frequency (GHz)	QDA	KNN
7.65	40.3%	44.5%
5.55	33.4%	38.5%
3.96	44.4%	46.3%
2.38	49.8%	55.5%
1.32	46.8%	53.6%
0.80	45.2%	49.9%

TABLE B3
CROSS-VALIDATION ERRORS FOR DATA SET III

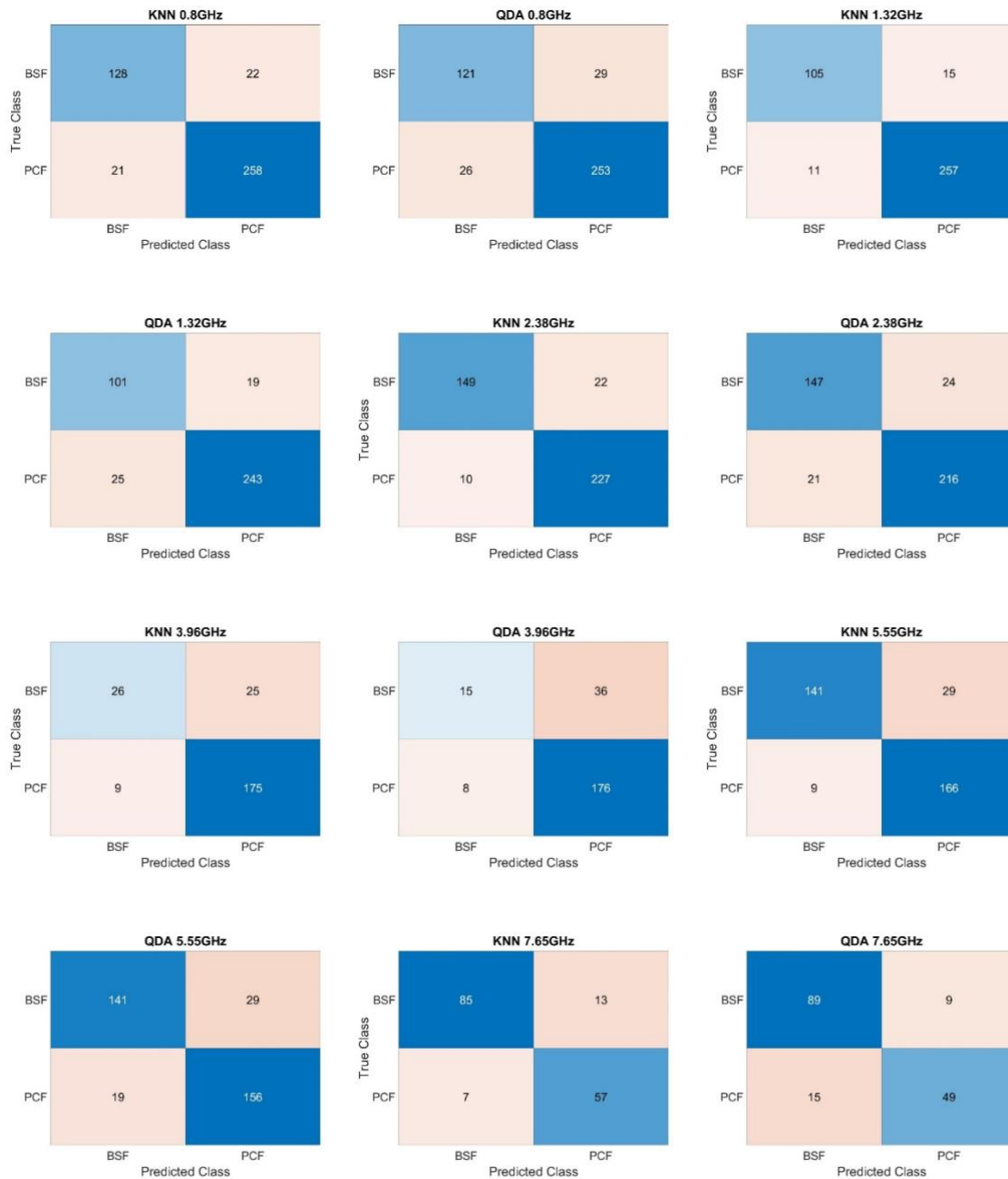| Frequency (GHz)	QDA	KNN
7.65	24.9%	24.6%
5.55	9.38%	10.0%
3.96	24.7%	23.4%
2.38	8.16%	8.16%
1.32	8.31%	8.18%
0.80	13.5%	14.5%

Figure B1. Confusion matrices for the six frequencies measurements frequencies used for

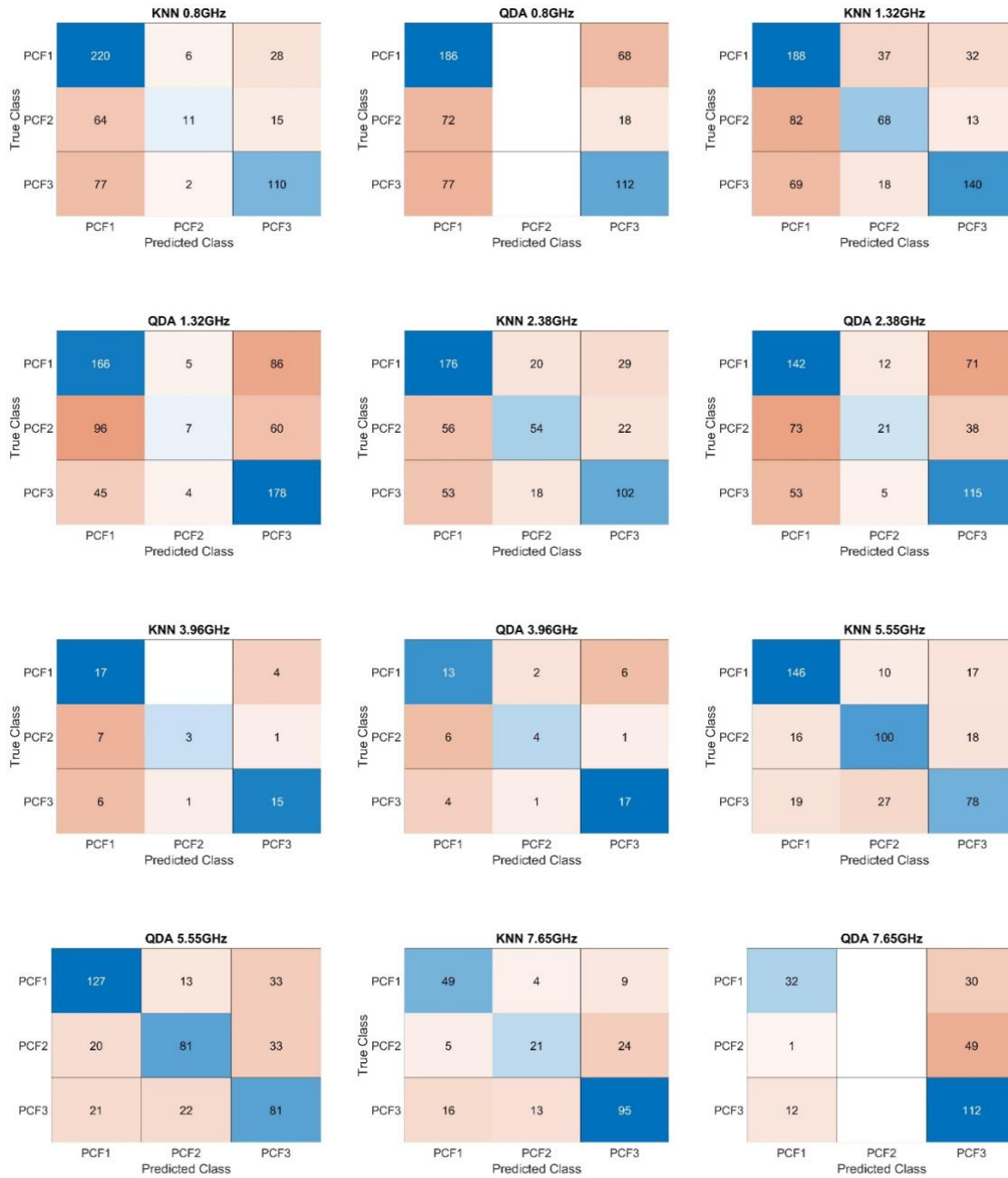*T. brucei* cell classification in Chapter VI. The models used BSF and one strain of PCF.

Figure B2. Confusion matrices for the six frequencies measurements frequencies used for

T. brucei cell classification in Chapter VI. The models used the three PCF strains.
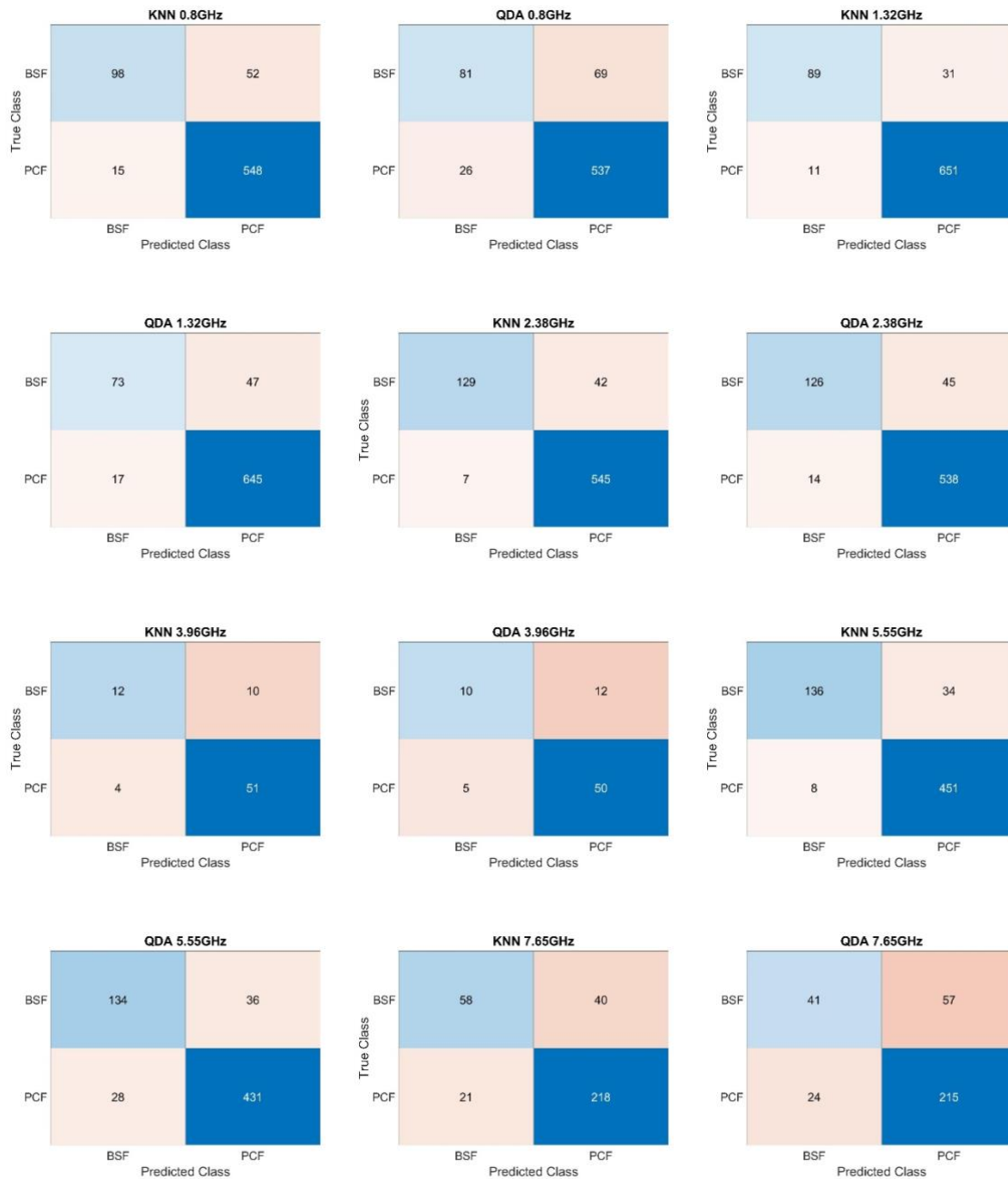
Figure B3. Confusion matrices for the six frequencies measurements frequencies used for *T. brucei* cell classification in Chapter VI. The models used BSF as one class and PCF cells with all three strains of PCF cells combined into one class.